12-2018

Computational prediction, characterization, and methodology development for two-dimensional nanostructures: phosphorene and phosphide binary compounds.

Congyan Zhang
University of Louisville

COMPUTATIONAL PREDICTION, CHARACTERIZATION, AND
METHODOLOGY DEVELOPMENT FOR TWO-DIMENSIONAL
NANOSTRUCTURES: PHOSPHORENE AND PHOSPHIDE BINARY COMPOUNDS

By

Congyan Zhang

B.S., North University of China, 2010
M.S., Shanghai University, 2013
M.S., University of Louisville, 2015

A Dissertation
Submitted to the Faculty of the
College of Arts and Sciences of the University of Louisville
in Partial Fulfillment of the Requirements
for the Degree of

Doctor of Philosophy
in Physics

Department of Physics and Astronomy
University of Louisville
Louisville, Kentucky

December 2018

COMPUTATIONAL PREDICTION, CHARACTERIZATION, AND
METHODOLOGY DEVELOPMENT FOR TWO-DIMENSIONAL
NANOSTRUCTURES: PHOSPHORENE AND PHOSPHIDE BINARY COMPOUNDS

By

Congyan Zhang

B.S., North University of China, 2006
M.S., Shanghai University, 2010
M.S., University of Louisville, 2013

A Dissertation approved on

November 20, 2018

by the following Dissertation Committee:

_____
Dr. Ming Yu (Dissertation Director)

_____
Dr. Chakram S. Jayanthi

_____
Dr. Gamini Sumanasekera

_____
Dr. Xiao-An Fu

ACKNOWLEDGMENTS

XiaoAn Fu for being a part of my committee in addition to providing advice and guidance that has improved my thesis.

It is a pleasure to thank the many people in the department who made this thesis possible, especially, Ms. Mary Gayle Wrocklage and Ms. Rea Diehlmann. I would also like to thank Dr. Lutz Haberzettl and Dr. Harrison for the technical support, especially, the support that they provided when I needed to connect to the university computer servers from home. My acknowledges also go to Dr. Paul Tandy and Dr. Qi Dong for their wonderful work on fitting the parameters of SCED. Many thanks to my co-worker Dr. Cherno Baba Kah, Dr. George Anderson, Mr. Md Rajib Khan Musa, Ms. Safia Abdullah R Alharbi and Mr. Manthila Chaturange Rajapakse for their support and assistance.

Nobody has been more important to me in the pursuit of this project than my Husband Rong Zhao and my daughter Kathy Zhao. I would also like to thank my parents and in-laws.

ABSTRACT

COMPUTATIONAL PREDICTION, CHARACTERIZATION, AND
METHODOLOGY DEVELOPMENT TWO-DIMENSIONAL NANOSTRUCTURES:
PHOSPHORENE AND PHOSPHIDE BINARY COMPOUNDS

Congyan Zhang

November 20th, 2018

In this thesis, a comprehensive computational simulation was carried out for predicting, characterizing, and applications of two-dimensional (2D) materials. The newly discovered GaP and InP layers were selected as an example to demonstrate how to explore new 2D materials using computational simulations. The performance of phosphorene as the anode material of Lithium-ion battery was discussed as the example of application of 2D material. Furthermore, the semi-empirical Hamiltonian for phosphorous and lithium elements have been developed for our future work on the application of phosphorus and lithium-based systems.

The novel 2D materials of GaP and InP binary compounds were found to possess unique anisotropic structural, electronic, and mechanical properties. Their crystalline structures show orthorhombic lattices symmetry and high buckling of 2.14 Å-2.46 Å. They have strong directional dependence of Young's moduli and effective nonlinear elastic moduli. They have wide fundamental bandgaps which were also found to be tunable under the strain. In particular, a direct-indirect bandgap transition was found under certain strains,

reflecting their promising applications for the strain-induced bandgap engineering in nanoelectronics and photovoltaics.

To completely understand the performance of phosphorene as the anode material of Li-ion battery, the lithium adsorption energy landscape, diffusion mobility, intercalation, and capacity of phosphorene were studied. The calculations show the anisotropic diffusivity and the ultrafast diffusion mobility of lithium along the zigzag direction. Phosphorene could accommodate up to the ratio of one Li per P atom (i.e., $Li_{16}P_{16}$). In particular, there was no lithium clustering even at the high Li concentration. The structure of phosphorene, when it was fractured at high concentration, is reversible during the lithium intercalation. The theoretical value of the lithium capacity for a monolayer phosphorene is predicted to be above 433 *mAh/g*.

The SCED-LCAO Hamiltonians for phosphorus and lithium were developed in this thesis. The optimized parameters were obtained by fitting the structural and electronic properties of small clusters and bulk phases, which were calculated by the *ab*-initial methods. The robustness tests of phosphorus parameters were executed by relaxing the back phosphorus, phosphorene, and blue phosphorene with SCED-LCAO-MD code. The energy order and band gap of black phosphorus, phosphorene and blue phosphorene are all consistent with the DFT calculations and experimental measurements. The robustness tests of Li parameters were executed for the BCC bulk of Li and its stability was proved.

TABLE OF CONTENTS

LIST OF TABLES

LIST OF FIGURES

CHAPTER I

INTRODUCTION

1.1   Background of 2D materials

About 80 years ago, Two-dimensional (2D) materials were argued not exist because
they were assumed thermodynamically unstable. The argument was that a divergent
contribution of thermal fluctuations in low-dimensional crystal lattices should lead to such
displacements of atoms that become comparable to interatomic distances at any finite
temperature [1-3]. Experimental observations showed that the melting temperature of thin
films (*e.g.,* monatomic steps on (100) alkali halide surfaces and rare gases on graphite)
rapidly decreases with decreasing thickness [4, 5]. For this reason, atomic monolayers were
known only as islands on the top of three-dimensional (3D) subtracts, usually grown
epitaxially on top of mono-crystals with matching crystal lattices. Without such a 3D base,
2D materials were presumed not to exist.

The knowledge on 2D material was promoted in the year 2004 [6] when a free-
standing graphene was mechanically exfoliated. This single atom layered crystal has shown
promise as a "wonder material" due to a wealth of interesting (shown in Figure 1.1) and
unique properties, which also led to the 2010 Nobel prize in physics. The deep research in
graphene attracted interests in exploring other 2D materials. As the consequence, the 2D
family includes not just carbon material but also graphene-like layers [7-26], transition
metal dichalcogenide (TMD) layers [27-33], MXenes [34], and layered oxide materials

[35], etc. (shown in Figure 1.2). 2D nanostructures are now one of the greatest widely studied areas.
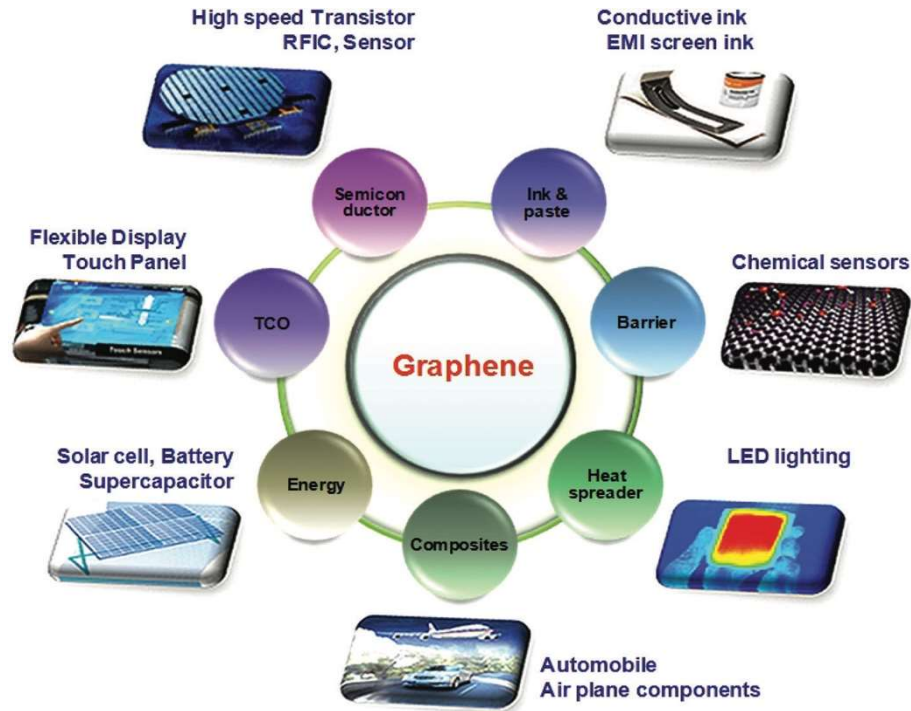
Figure 1.1 Overview of applications of graphene in different fields [36].

The main reason for the extensive focus on 2D materials is their nano-scaled thickness, which leads to unique properties due to the quantum size effect. Furthermore, because of the single-layer thickness, 2D films have different electronic distribution, geometry, high surface-bulk ratio and absence of interlayer interactions by comparing with their 3D counterparts. On the other hand, the absence of interlayer interaction and the electron confinement are very important in finding the band structure of 2D materials, which indicates the changing of optical and electronic properties from 3D to 2D. Similarly, the quantum size effects and high surface-bulk ratio lead to remarkable changes in chemical and mechanical properties[37].

Figure 1.2 lists some of successfully synthesized the 2D materials before the discovery of phosphorene. 2D crystals can be flat, buckled, puckered, or even sandwiched layers. They can be insulator, semiconductor, metal or even superconductor, which indicate the wide application of 2D materials. Graphene and *h*-BN have the similar flat honeycomb structure but totally different in electronic properties, graphene has a zero gap at the Dirac cone, while *h*-BN has a wide band gap with 4.69 eV [7]. On the other hand, TMD's layered structures, which are formed as a transition metal atom attached to two atoms from Group VI of the Periodic Table, can be either semiconductors, or half-metals, or metals, or even superconductors.
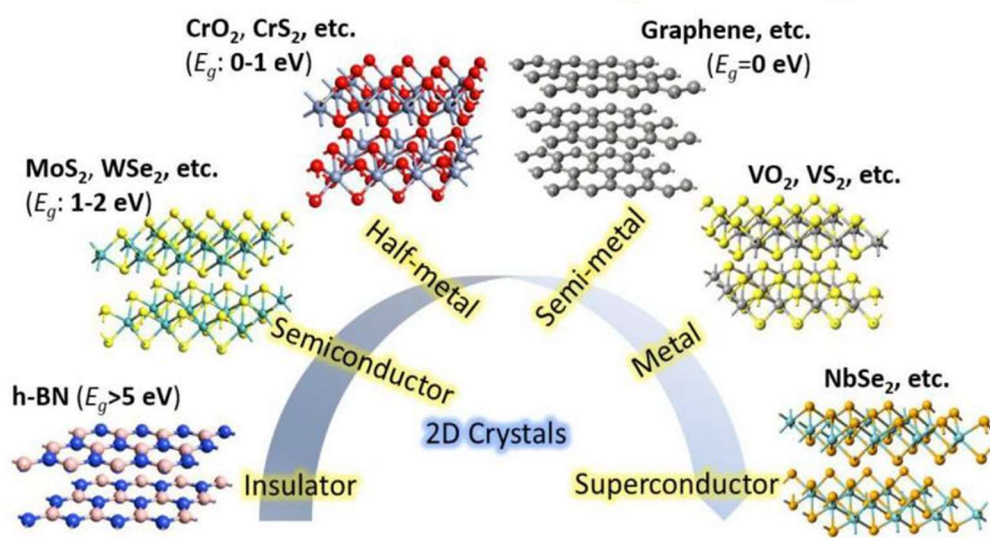
Figure 1.2 The 2D crystals before the discovery of phosphorene [38].

2D materials appear as the most suitable candidate to eventually create a new generation of electronic devices. Some of the advantages of 2D materials than the 3D bulks are listed below: First, the band gap of 2D layers can be tunable just by changing the number of layers, which is more convenient for the experimenters to design the desirable

devices. Second, the longer distance between two layers means more space and fewer interactions between layers. As a consequence, 2D materials show higher capacity and faster diffusion speed, indicating their applications on energy storage and batteries. Third, charge carriers are confined in the atomically thin semiconductor, resulting in a narrower mobile charge distribution. This confinement of charge carriers allows the carriers can be easily controlled by the gate voltage, leading to excellent gate electrostatics. 2D materials have been reported to have wide applications in the area of electronic devices, sensors, energy storage, batteries, optoelectronics, photovoltaics, and so on [7-9, 27-33, 39-42].

1.2   Background of the computational simulation on 2D materials

In order to understand the materials properties fundamentally, modern materials research often requires a close combination of computation and experiments. The theoretical works are very important to motivate, aid, query and collaborate with experimental investigations. Theoretical studies include but not limited to the following works: explore the optimized structure; examine the stability; characterize the properties including structural, electrical, optical, mechanical and thermal properties. Furthermore, computational modeling is one of the most useful tools for the study of dynamical processes in nanostructure systems; in particular, for the systems under extreme conditions (e.g., high pressures, low/high temperatures, toxic gases, etc.) that performing experimental investigation is hard, impossible, or cost expensive.

So far, a number of computational methods and tools have been well established. For instance, the density functional theory (DFT) [43, 44], atomic molecular dynamics [45, 46], Monte Carlo techniques [47], and phase-field method [48-50] have been used very frequently in the theoretical simulations ranges from small clusters with several atoms to

big systems (*e.g.*, DNA) with thousands of atoms. Promoted by various government agencies (*e.g.*, the Materials Genome Initiative (MGI) for Global Competitiveness launched by the National Science and Technology Council in the United States [51]), computational simulations on materials have been steadily moving towards discovering and designing new materials guided by computation, machine learning and data mining or by a closely tied combination of computational predictions and experimental validation [52]. Due to their attractive properties different with 3D materials and the wide applications, the exploration on 2D materials by computation or the combination of computation and experiment is one of the primary works for the material researchers.

1.3   Computational discovery of 2D phosphide binary compounds

Currently, most successfully synthesized 2D materials have their corresponding layered bulk counterparts (*i.e.*, those with van der Waals interaction between layers). Discovering new 2D materials from their layered bulk counterparts attracted extensive interests. Further interests are then focused on the discovery of other possible types of 2D materials which have no corresponding layered bulk counterparts in nature, and mechanical stripping or general CVD method might not work easily for synthesizing those types of materials. It is extremely tough and challenging to discover and realize these types of 2D materials directly from the experimental synthesis and therefore, theoretical predictions with fundamental guiding for synthesis are necessary.

Extensive efforts have been devoted to this issue both theoretically and experimentally [9-26, 53-63]. In particular, the theoretically predicted silicene, germanene [10, 13-26] and borophene [60-63] layeres have been successfully synthesized on certain substrates and opened a door to further explore unknown 2D materials which have no layered bulk

counterpart, such as SiC, GeC, and III-V binary compounds [9, 12, 58, 59]. Here we tried to provide a pathway to find such 2D binary compounds from their bulk counterparts. Bulk GaP and InP binary compounds were selected as examples and seek if there exist stable layered GaP and InP binary compounds by truncating the zinc-blend bulk counterparts along certain orientations.

1.4   Phosphorene and its application

Phosphorene was newly discovered in the year of 2014 [64-66]. Different from all mentioned 2D layers, phosphorene has anisotropic structural behavior, which leads to anisotropic electronic, mechanical, and thermal properties. Based on the novel properties, phosphorene has been reported to have promising applications in many areas include electronic devices, sensors, thermoelectric devices, energy storage, batteries and so on [67].

The density of states and band structure of phosphorene in Figure 1.3 (a) indicated that phosphorene is a semiconductor with a direct band gap at Γ. Furthermore, the band structure is anisotropic between Γ-X and Γ-Y directions, reflecting its anisotropic band behavior. As shown in Figure 1.3 (b), the electrical conductance and electron mobility was also reported to have anisotropic behavior [68], where the value of mobility along the armchair direction is 3 orders of magnitude larger than that along the zigzag direction. The electronic properties of phosphorene indicate that it is a perfect candidate for the electronic devices such as field effect transistors. Figure 1.3 (c) shows the orientation dependence of Young's modulus [69] along the zigzag direction (166 GPa) and armchair direction (44 GPa). Another strong indication of the anisotropic nature of phosphorene is the direction dependence of the Poisson's ratio [70] (Figure 1.3 (d)). The Poisson's ratio along the zigzag direction (0.703) is about 4 times bigger than that along the armchair direction (0.175).

6

These unique mechanical properties make phosphorene a promising novel material for nanoelectromechanical systems and devices.
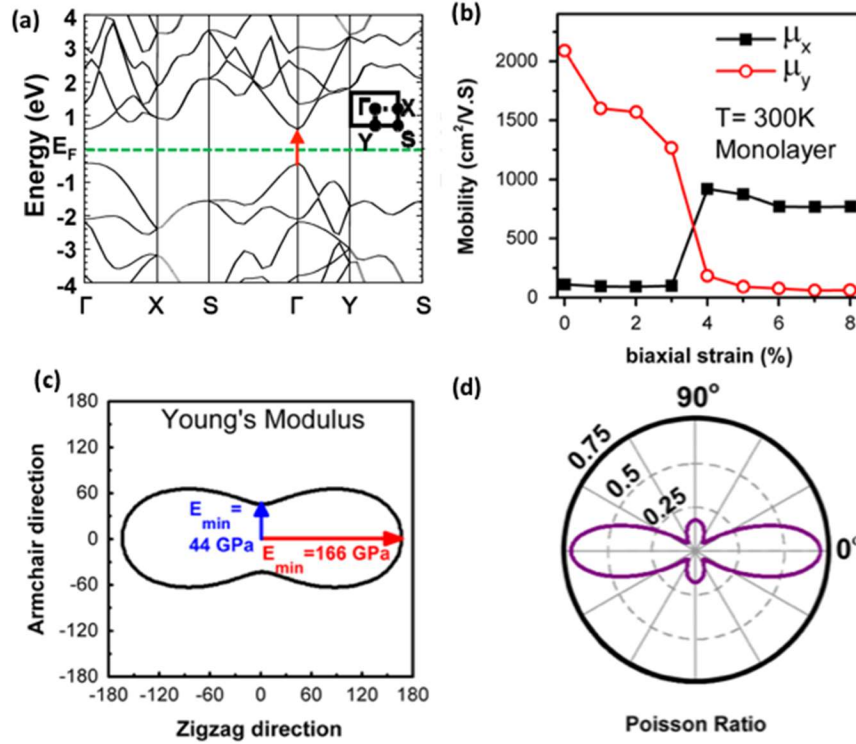
Figure 1.3 Anisotropic properties of phosphorene [67].

The structure of phosphorene is puckered in nature, which leads to the bridges along armchair direction and valleys along the zigzag direction. Therefore, the speed of Li ions migration along the zigzag direction is expected to be much faster than that along the armchair direction, which may lead to a high diffusion along the zigzag direction. On the other hand, the puckered structure is also expected to have large space between phosphorene layers, which increase the possibility to accommodate more Li-ions. Thus, the Li capacity on phosphorene may be expected to be higher than that on other 2D layers. Based on these considerations, we are interested in whether phosphorene can be the high-performance anode materials for Li-ion battery, through studying the lithium adsorption

7

energy landscape, the lithium diffusion mobility, the lithium intercalation, and the lithium capacity of phosphorene.

1.5   Develop the SCED Hamiltonian for Phosphorus and Lithium elements

In recent years, the phosphorus-carbon nanocomposite anodes for lithium-ion have been studied by experimentalists, which displays high initial capacities (1700 *mAh/g*) [71]. That inspires researchers to explore the performance of Li-ion battery with the phosphorene-graphene layered heterostructure as the anode material [72] since graphene covered on top/bottom of the phosphorene can protect the phosphorene not to be affected by the environment and its flexibility can provide large free space for Li intercalation and holds the backbone of phosphorene during Li extrication. Studying the stability, diffusion, and capacity of such large graphene-phosphorene heterostructure is beyond the ability of the DFT calculations. In this case, it is necessary to develop a semi-empirical method that fast, reliable, robust, transferable with predictive power and can handle large systems of atoms.

The self-consistent and environment-dependent (SCED) Hamiltonian within the framework of the linear combination of atomic orbitals (LCAO), referred to as SCED-LCAO Hamiltonian. was, therefore, proposed by the Condensed Matter Theory (CMT) group of the University of Louisville [73-75]. The particularity of this method is that the charge redistribution is calculated using self-consistency and also not only two-center interactions are considered within its environment-dependent term but multi-center interactions in electron-electron, electron-ion and ion-ion are also considered. The electrons screening effects are therefore considered during simulations. A thorough optimization and robust testing of parameters for SCED-LCAO Hamiltonian ensures its

transferability. In this work, we further developed the SCED-LCAO Hamiltonian for phosphorous and lithium elements which could be applied to study the large C-P-Li system for Li-ion battery applications.

1.6   Outline of thesis

The fundamental theory employed in our computational simulations for discovery, characterization and application of 2D nanomaterials will be first introduced in chapter 02. Both the first principle DFT methods and the semi-empirical SCED-LCAO approach will be discussed in detail. In chapter 03, we report our recent systematic study on seeking energetically preferential 2D monolayers of GaP and InP binary compounds beyond the low buckled honeycomb structured GaP/InP sheets. In chapter 04, we performed a systematical study of the Li adsorption energy landscape, the diffusion process, the ability of phosphorene to accommodate Li atoms, and the capacity of Li in phosphorene using the first-principles calculations. Chapter 05 will describe in detail how to optimize the SCED-LCAO Hamiltonian for Phosphorus and Lithium elements.

The future works will be discussed in chapter 06. The first ongoing work focuses on the Li intercalation. The idea of phase transition from phosphorene to blue phosphorene comes from our study on the Li interaction discussed in chapter 04. We propose to develop a new guideline for producing blue phosphorene by insert Li to the black phosphorus under ambient condition. The second ongoing work is to study the vibration modes of black phosphorus under high pressure. We will figure out the reason for the vibration modes shift under high pressure found experimentally. The third ongoing work motivated by the newly discovered single crystal of BAs with ultrahigh thermal conductivity BAs layer [76]. We are seeking if there exist new 2D allotropes of BAs family, which has novel anisotropic

properties, as found in 2D Gap/InP (discussed in chapter 03). In particular, we are interested in if such 2D BAs possesses high thermal conductivity.

CHAPTER II

METHODOLOGY FOR MATERIAL PREDICTION AND CHARACTERIZATION

2.1   Quantum mechanics based simulations

Quantum mechanics (QM) based simulation, which describes physical and chemical properties at the atomic/molecular level by combining electronic structure calculations and Newtonian dynamics, is the key to predict 2D materials. Computational simulation attempts to discover 2D materials by employing the molecular dynamics (MD) simulations based on QM, referred to as QM-MD.

The key for QM-MD simulations is to solve the many-body Schrödinger equation of the system. For a many-body system, the Hamiltonian is expressed by

$$H = -\sum_i \frac{\hbar^2}{2m_e} \nabla^2_{r_i} - \sum_I \frac{\hbar^2}{2M_I} \nabla^2_{R_I} - \sum_{I,i} \frac{z_i e^2}{|r_i - R_I|} + \frac{1}{2}\sum_{i,j} \frac{e^2}{|r_i - r_j|} + \frac{1}{2}\sum_{I,J} \frac{z_I z_J e^2}{|R_I - R_J|} \quad (2\text{-}1)$$

Where, m_e, M_I, r and R are the masses and the coordination of electron and nucleus, respectively. The five terms in equation (1) include the kinetic energies of electrons (the 1st term) and ions (the 2nd term), and the interactions between electron-ion (the 3rd term), electron-electron (the 4th term) and ion-ion (the 5th term).

Nuclei have much larger masses than the electrons, therefore, electrons move much faster than nuclei and respond instantaneously to the motion of the nuclei. Based on this fact, Max Born and J. Robert Oppenheimer assumed that the motion of nuclei and electrons in a molecule can be separated. The Born-Oppenheimer approximation treats nuclei as

temporarily stationary point particles, which makes the kinetic energy of nuclei (the 2nd term in equation (1)) to be negligible, and the ion-ion interaction (the 5th term in equation (1)) to be an additive constant to the energy. Therefore, the Schrödinger equation is solved for the wave-function of the electrons alone. The expression of the Hamiltonian for the electrons in the system is then given by,

$$H = -\sum_i \frac{\hbar^2}{2m_e} \nabla_{r_i}^2 - \sum_{I,i} \frac{Z_i e^2}{|r_i - R_I|} + \frac{1}{2}\sum_{i,j} \frac{e^2}{|r_i - r_j|} \qquad (2\text{-}2)$$

Even though the Born-Oppenheimer approximation simplified the Hamiltonian of the many-body system significantly, it is still impossible to give an exact solution for a system with lots of electrons and ions. The N electrons in the system indicates the $3N$ dimension of the Hamiltonian, which increases the calculation amount extensively for only one MD step. As the consequence, much more calculation time and storage of the computer are required for relaxing the system. Thus, Researchers tried to find other approximations to reduce the computational cost. Based on the Born-Oppenheimer approximation, the quantum mechanical methods may be classified into two flavors: the first-principles based methods (include the wave-function based ab-initio methods [77-81] and charge density-based DFT methods[43, 44, 82]) and the semi-empirical methods.

The wave-function based first-principles MD simulations, usually begin with a HF calculation, where the wave-function expressed in terms of a set of single-electron states (*i.e.* $\Psi(r_1, r_2, \dots r_N,) = \phi_1(r_1)\phi_2(r_2)\dots\phi_N(r_N)$), and subsequently add the correction for electron-electron interactions. The wave-function based methods are highly accurate methods, but the calculations are still very slow and need very large computational memory. Therefore, the applications of these methods are limited to systems with their size up to a

few tens of atoms. They are mostly used in quantum chemistry to deal with the small systems.

In the DFT-based methods [43, 44, 82], the 3-dimensional charge density replaces the $3N_{electrons}$-dimensional wave functions, which rapidly reduces the computational cost. DFT based computational simulations are accurate and the most widely used methods in the condensed matter physics and the materials science communities even though they are still limited by the size of systems (up to few hundreds or about a thousand by employing a linear scaling algorithm (order-N scheme) [83, 84]).

Semi-empirical methods, on the other hand, treat the Hamiltonian matrix elements by parametric functions and make the calculations more efficient. There are different semi-empirical flavors in dealing with the Hamiltonian including the conventional two-center tight-binding (TB) Hamiltonians [85, 86] and latterly developed TB Hamiltonians with either considering the self-consistency and/ or the environment-dependency [87-90]. They are widely used in chemistry, solid state physics, and materials science [73, 89, 91, 92]. These methods can handle larger systems in the order of tens of thousands of atoms with a simulation time few nanoseconds (*ns*). However, the semi-empirical Hamiltonians need to be developed for its transferability. In order to improve the transferability and therefore, have the predict power, a decade ago, our CMT group developed the SCED-LCAO method. The main feature of the SCED-LCAO method compared to other semi-empirical approaches is that environment-dependency and charge re-distributions are treated on equal footing. We have also implemented an order-N scheme [93, 94] in the SCED-LCAO framework that has enabled us to perform full geometry optimization of systems of sizes about 20,000 atoms using *sp*3 basis set [95]. Thus, highly efficient and reliable large-scale

QM-MD simulations are now attainable using the SCED-LCAO scheme. So far, the SCED-LCAO method has shown its reliability and transferability on simulating the C, Si, Ge, and B elements-based systems [56, 73-75, 96-98].

In this thesis, the DFT-based methods were employed to predict the new 2D anisotropic phosphide binary compounds and to investigate the performance of phosphorene as the anode material of Li-ion battery. On the other hand, the reliable and transferable SCED-LCAO Hamiltonian was developed for P and Li elements which will be applied to deep study the graphene-phosphorene layered heterostructure as the anode material of Li-ion battery.

2.2   Density functional theory

In the density-functional theory (introduced in 1964 by Hohenberg and Kohn [43]), the electronic density $n(\vec{r})$ was introduced to replace the wave function, (i.e., $n(\vec{r}) = \sum_{i=1}^{N} |\varphi_i(\vec{r})|^2$). Kohn and Sham proposed an approach to promote the density functional theory, in which the complicate electron-electron interactions are treated as the part of the exchange and correlation. The Hamiltonian in equation (3) can be simplified as,

$$H = -\frac{\hbar^2}{2m}\nabla^2 + V_{eff} \qquad (2\text{-}3)$$

where V_{eff} is defined as the effective potential, and is expressed within the Kohn-Sham [43, 44] approximation as:

$$V_{eff}^{KS} = V_{ext}(\vec{r}) + V_{xc}(\vec{r}) + \int \frac{n(\vec{r}\prime)}{|\vec{r} - \vec{r}\prime|} d\vec{r} \qquad (2\text{-}4)$$

where the Coulomb potential arising from the nuclei is treated as an external potential $V_{ext}(r)$, and the exchange-correlation potential $V_{xc}(\vec{r})$ is

$$V_{xc}(\vec{r}) = \frac{\delta E_{xc}[n(\vec{r})]}{\delta n(\vec{r})}\Big|_{n_v(\vec{r})=n(\vec{r})} \tag{2-5}$$

The corresponding energy can be written as

$$E = 2\sum_i^{occ}\varepsilon_i + E_{xc}[n(\vec{r})] - \int V_{xc}(\vec{r})\,n(\vec{r})d\vec{r} - \frac{e^2}{2}\int\frac{n(\vec{r})n(\vec{r}\prime)}{|\vec{r}-\vec{r}\prime|}d\vec{r}d\vec{r}\prime \tag{2-6}$$

The challenge now is to deal with the $E_{xc}[n(\vec{r})]$ term to solve the exact ground state energy and density. Two charge density-based approximations were widely used to describe this term: the local density approximation (LDA)[43], and the generalized gradient approximation (GGA)[99].

The LDA assumed that the exchange-correlation energy at every position in space equal to the uniform electron gas having the same density as found at that position.

$$E_{xc}^{LDA} = \int \in_{xc}\left(n(\vec{r})\right)n(\vec{r})d\vec{r} \tag{2-7}$$

In molecules, the electron density can vary rapidly over a small region of space, the uniform electron gas seems not to be such a great model. The GGA was developed by making the functional dependance on both the density and the gradient of the density,

$$E_{xc}^{GGA} = \int \in_{xc}\left(n(\vec{r}), |\nabla n(\vec{r})|\right)n(\vec{r})d\vec{r} \tag{2-8}$$

To give a reliable prediction, the computational simulation of the system should be built on selecting the "right" approximation. To do so, we should use different calculation methods for the same system, compare the theoretical results with the experimental measurements, and then choose the one which is closer to the experimental observations.

The DFT-based computational packages include VASP, SIESTA, WIEN2k, ABINIT, CASTEP, etc. VASP[100] (Vienna Ab initio Simulation Package), which was employed

in our DFT calculations, is a complex package for atomic scaled materials modeling. In VASP, the interactions between the electrons and ions are described using either ultra-soft pseudopotentials (US-PP)[101], or the projector-augmented-wave method (PAW)[102]. As for the electrons-electrons interaction, the exchange-correlation functional approximations include LDA and GGA. The popular GGA methods include Perdew-Wang 91(PW91) and Perdew-Burke-Ernzerhof (PBE) [103]. For all elements, VASP provides 5 pseudopotentials files in different flavors: US-PP-LDA, US-PP-GGA, PAW-LDA, PAW-GGA-PW91, and PAW-GGA-PBE.

The van der Waals weak interactions are taken into account in VASP by a parametric function which is added to the conventional Kohn-Sham DFT energy,

$$E_{DFT-VDW} = E_{KS-DFT} + E_{disp} \tag{2-9}$$

where E_{disp} is the dispersion energy, calculated using various approximate methods. For example, the Grimme's D2 method [104], (referred DFT-D2 in VASP), takes the correction term by

$$E_{disp} = -\frac{1}{2}\sum_{i=1}^{Nat}\sum_{j=1}^{Nat}\sum_{L}\frac{C_{6ij}}{r_{ij,L}^6}f_{d,6}(r_{ij},L) \tag{2-10}$$

where the summations are over all atoms *Nat* and all translations of the unit cell $L = (l_1, l_2, l_3)$, the prime indicates that $i \neq j$ for $L = 0$, C_{6ij} denotes the dispersion coefficient for the atom pair *ij*, r_{ij}, L is distance between atom *i* located in the reference cell $L = 0$, and atom *j* in the cell *L*, and the term , $f(r_{ij})$ is a damping function whose role is to scale the force field such as to minimize contributions from interactions within typical bonding

distances. In the D3 correction method of Grimme et al. [105] (referred as DFT-D3 in VASP), the following vdW-energy expression is used:

$$E_{disp} = -\frac{1}{2}\sum_{i=1}^{Nat}\sum_{j=1}^{Nat}\sum_{L}\left(f_{d,6}(r_{ij},L)\frac{C_{6ij}}{r_{ij,L}^6} + f_{d,8}(r_{ij},L)\frac{C_{8ij}}{r_{ij,L}^8}\right) \qquad (2\text{-}11)$$

Unlike in the method D2, the dispersion coefficients C_{6ij} are geometry-dependent as they are adjusted on the basis of local geometry (coordination number) around atoms i and j. In the zero damping D3 method (D3 (zero)), damping of the following form is used:

$$f_{d,n}(r_{ij},L) = \frac{S_n}{1+6\left(r_{ij}/(S_{R,n}R_{0ij})\right)^{-\alpha_n}} \qquad (2\text{-}12)$$

Where $R_{0ij} = \sqrt{\frac{C_{8i}}{C_{6ij}}}$, the parameters α_6, α_8, $S_{R,8}$ are fixed at values of 14, 16 and 1, respectively, and S_6, S_8, $S_{R,6}$ are adjustable parameters whose values depend on the choice of exchange-correlation functional.

Furthermore, for the local and semi-local density functional approximations, the most affordable type of Kohn-Sham functionals for solids, badly underestimate the band gaps of semiconductors (the materials of principle interest in practical applications) and insulators due to self-interaction error [106, 107]. Hybrid functionals that incorporate a fraction of nonlocal Hartree-Fock (HF) exchange overcome this issue; however, computing HF exchange in solids is considerably more expensive than evaluating a semi-local density functional. Methods based on the GW [108, 109] approximation can also be used to compute band gaps more accurately, but these techniques are even more expensive than hybrids. A good compromise between cost and accuracy is provided by short-range screened hybrids: functionals that include HF exchange only for the short-range part of the

electron-electron interaction, which significantly reduces the cost of evaluating the nonlocal HF part of the exchange as compared to standard hybrids [110]. Hybrid functional calculation using the HSE06 functional (referred HSE06 in VASP) provided the most accurate results (in comparison with experiments) [111].

2.3   Optimization, prediction, and characterization of 2D materials

2.3.1   Structural Optimization

In the structural optimization process, we need to perform the QM-MD calculations where the total energy of the system is obtained by solving Schrödinger equation of the many-body system: $\hat{H}|\Psi_\lambda\rangle = \varepsilon_\lambda|\Psi_\lambda\rangle$, $E_{tot} = \sum_\lambda f_\lambda \varepsilon_\lambda + E_{ion}$, and the forces on each atom are calculated by $\vec{F} = -\nabla_i E_{tot} = -\nabla_i(\sum_\lambda f_\lambda \varepsilon_\lambda) - \nabla_i E_{ion}$, where the band structure part (the 1st term) is calculated through the Hellmann-Feynman theorem [112-114]. Based on the forces exerted on each atom, a new set of coordinates of the system is predicted by solving the equation of motion (*e.g.,* the Congregate-Gradient algorithm [115] in VASP). When the energy difference and forces obtained from two adjacent MD steps reach to the criteria (e.g., 10^{-4} eV for energy and 10^{-3} for eV/Å for force, respectively), which indicates the almost same configurations simulated from these two adjacent MD steps, the system is fully relaxed. The optimized structure with a given symmetry will be obtained by scaling the lattice constants of the system and repeating QM-MD the relaxation process mentioned above for each set of scaled lattice constants. Finally, the scaled system with the lowest energy is the optimized structure at equilibrium (*e.g.*, the optimized WS_2 sheet using GGA-PAW-PBE in Figure 2.1)
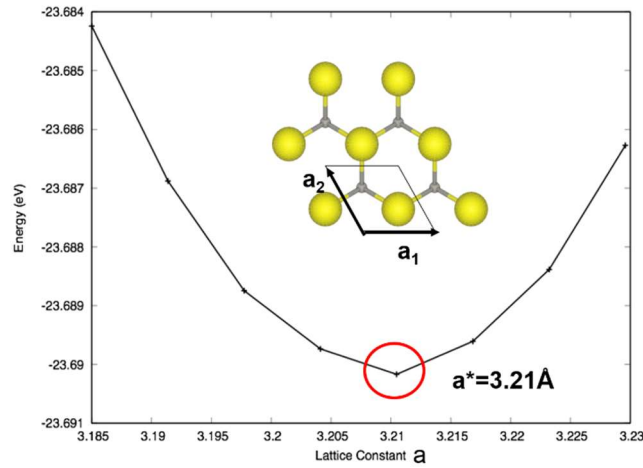
Figure 2.1 The total energy of the 2D WS$_2$ sheet as the function of the lattice constant a with its minimum at a^* =3,21 Å (indicated with the red circle). The inset is the top view of the 2D WS$_2$ with the unit vectors $a_1 = (a, 0)$, $a_2 = (-\frac{a}{2}, \frac{\sqrt{3}}{2})$ [116].

To predict the new structures, a global optimization process is required, where structures with different geometric symmetries will be optimized. The structures without local energy minimum during the optimization process indicating that such structures are energetically unstable (e.g., the low buckled (LB) BAs honeycomb sheet shown in Figure 2.2(a)), and the structures with local energy minimum demonstrate that they are energetically stable and exist (e.g., the flat (FL) BAs honeycomb sheet in Figure 2.2(a) and high-buckled (HB), low-buckled, flat 2D honeycomb structures of Si and Ge in Figure 2.2 (b) [10], respectively.)
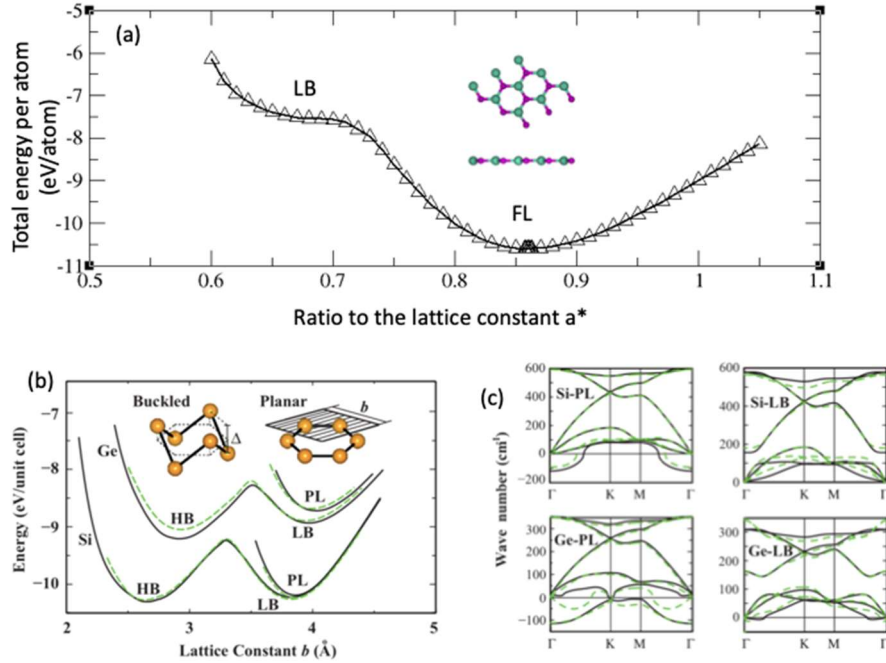
Figure 2.2 (a) The total energy per atom of BAs monolayer as a function of the ratio to a*, where a*= 3.946 Å. The insert is the energetically stable BAs flat layer; (b) the energies per unit cell of 2D Si and Ge as the function of the lattice constant. In which the hexagonal unit cell and the buckling parameter Δ are inserted; (c) phonon dispersion curves of the flat layers and low buckled layers of Si and Ge obtained in figure (b).

2.3.2   Lattice vibration and phonon dispersion

Even through structures are energetically stable from optimization process, they might not be dynamically stable, if any of their low lattice vibration frequencies are negative. Examples are shown in Figure 2.2 (c), where LB, and FL honeycomb structures of Si and Ge are energetically stable (as shown in Figure 2.2 (b)), but the low lattice vibration modes (i.e., phonon dispersion) for FL structures calculated from the force-constants and linear response theory are negative, indicating that FL honeycomb Si (Ge) sheet is not dynamically stable and does not exist. Therefore, to predict new 2D structure, one must

20

check, in addition to the total energy calculation, the lattice vibration frequencies and phonon dispersion spectrum.

The dynamic stability of 2D materials can be examined from the analysis of the lattice vibrational modes using the combination of the phonon Boltzmann transport equation and the first-principles phonon calculations, as implemented in PHONOPY [117] code, which can directly use the force constants calculated by density functional perturbation theory. The phonon spectrum of a material is in principle can be determined by the first principles phonon calculations. Several approximation methods were introduced to calculate the phonon (*e.g.*, the harmonic approximation, the mean square atomic displacements and the quasi-harmonic approximation). The harmonic approximation is done by considering the displacement of each atom from its equilibrium position. The force constant matrix expresses as the following:

$$C_{i\alpha,j\beta}(\vec{R} - \vec{R}') = \frac{\partial^2 E}{\partial u_{i\alpha}(\vec{R})\partial u_{j\beta}(\vec{R}')} \tag{2-13}$$

where E is the energy of the system, u is displacement from its equilibrium position, $\vec{R}$ and $\vec{R}'$ are the lattice vectors, i and j are the ith and j^{th} atoms of the unit cell, α and β are the directions of the coordinate axes. The dynamical matrix could be expressed:

$$D_{i\alpha,j\beta}(\vec{q}) = \frac{1}{\sqrt{M_i M_j}} \sum_{\vec{R}} C_{i\alpha,j\beta}(\vec{R}) \, e^{-i\vec{q}\cdot\vec{R}} \tag{2-14}$$

where M_i and M_j are the masses of the ith and j^{th} atoms, and $\vec{q}$ is the wave vector. The dynamical property of atoms in the harmonic approximation is obtained by solving eigenvalue problem of dynamical matrix:

$$\omega^2(\vec{q})u_{i\alpha}(\vec{q}) = \sum_{j\beta} D_{i\alpha,j\beta}(\vec{q})u_{j\beta}(\vec{q}) \tag{2-15}$$

21

Modified and simplified Parlinski-Li-Kawazoe method is employed which is based on the supercell approach with the finite displacement method. The calculation and symmetrization of force constants are executed by using singular-value decomposition (pseudo-inverse). The key of this method would be the matrix formulations of equations, which leads to the coherent and flexible implementation.

Figure 2.3 shows, as an example, the calculated phonon spectrum for black phosphorus. For a unit cell containing N atoms, the dynamical matrix will have $3N \times 3N$ components and the number of optical modes is $3N$-3. Each mode can be represented by the Mulliken symbols [118, 119] according to the symmetric properties. For example, as shown in Figure 2.3, 'A' and 'B' are the non-degenerate modes, in which 'A' means the symmetric vibration with respect to rotation around the principle rotational axis, and 'B' means anti-symmetric vibration with respect to rotation around the principle rotational axis. 'E' means degenerate mode. Furthermore, the subscript '1' represents the symmetric vibration with respect to a vertical mirror plane perpendicular to the principal axis. The subscript '2' represents the anti-symmetric vibration with respect to a vertical mirror plane perpendicular to the principal axis. The subscript 'g' means the symmetric vibration with respect to a center of symmetry. The subscript 'u' means the anti-symmetric with respect to a center of symmetry. The prime (') indicates the symmetric vibration with respect to a mirror plane horizontal to the principal rotational axis, and the double prime (") indicates the anti-symmetric vibration with respect to a mirror plane horizontal to the principal rotational axis.
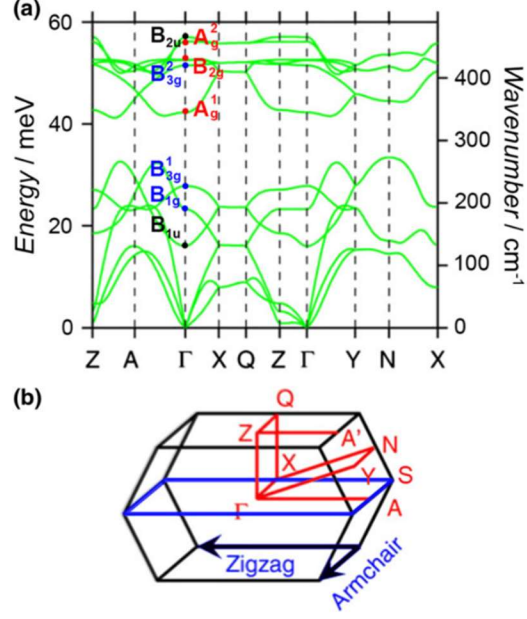
Figure 2.3 (a) The phonon dispersion spectrum of the black phosphorous. (b) The Brillouin zone with high symmetry points. The indices denote the nine vibration modes [120].

The Raman-scattering activity associated with a given vibrational mode is related to the change in the electrical polarizability of the materials due to the normal-mode displacements of the atoms. The essential ingredients are the gradients of the polarizability with respect to the nuclear coordinates [121]:

$$\frac{\partial \alpha_{ij}}{\partial R_k} = -\frac{\partial^3 E}{\partial G_i \partial G_j \partial R_k} = \frac{\partial^2 F_k}{\partial G_i \partial G_j} \tag{16}$$

where G_i and G_j are the ith and j^{th} component of an external electric field, and F_k is the calculated force on the kth atomic coordinate.

2.3.3   Electronic densities of states and band structures

In condensed matter physics the electronic density of states (DOS) of a system describes the number of states per an interval of energy at each energy level available to

be occupied. The density of states is obtained as the number of electronic states per unit volume, per unit energy, for electron energies near ε: $\bar{n}\left(\varepsilon_i\right)=\left(N(\varepsilon_i)-N(\varepsilon_{i-1})\right)/\Delta\varepsilon$, where $\Delta\varepsilon$ is the distance between two pins (energy difference between two grid point), and $N(\varepsilon_i)$ is the integrated DOS: $N(\varepsilon_i)=\int_{-\infty}^{\varepsilon_i}n(\varepsilon)d\varepsilon$. This method conserves the total number of electrons exactly. A high 'DOS' at a specific energy level means that there are many states available for occupation. A DOS of zero means that no states can be occupied at that energy level. The density of states function is important for calculations of effects based on band theory.

The electronic band structure (or simply band structure) of a solid describes the range of energies $\varepsilon_{i\vec{k}}$ that an electron within the solid may have (called *energy bands*, *allowed bands*, or simply *bands*) and ranges of energy that it may not have (called *band gaps* or *forbidden bands*). It is determined by solving the single electron Schrödinger equation: $H\psi_{i\vec{k}} = \varepsilon_{i\vec{k}}\psi_{i\vec{k}}$, where $\vec{k}$ is the wavevector given by $\vec{k} = n_1\vec{B}_1 + n_2\vec{B}_2 + n_3\vec{B}_3$. The reciprocal lattice vectors $\{\vec{B}_i\}$ in k-space are determined from the real space lattice vectors $\{\vec{A}_i\}$: $\vec{B}_1 = \frac{2\pi(\vec{A}_2\times\vec{A}_3)}{\vec{A}_3\cdot(\vec{A}_1\times\vec{A}_2)};\vec{B}_2 = \frac{2\pi(\vec{A}_3\times\vec{A}_1)}{\vec{A}_3\cdot(\vec{A}_1\times\vec{A}_2)};\ \vec{B}_3 = \frac{2\pi(\vec{A}_1\times\vec{A}_2)}{\vec{A}_3\cdot(\vec{A}_1\times\vec{A}_2)}$. In case of 2D systems, $\vec{k} = n_1\vec{B}_1 + n_2\vec{B}_2$, $\vec{B}_1 = \frac{2\pi(\vec{A}_2\times\vec{n})}{|\vec{A}_1\times\vec{A}_2|};\vec{B}_2 = \frac{2\pi(\vec{n}\times\vec{A}_1)}{|\vec{A}_1\times\vec{A}_2|}$, where $\vec{n}$ is the unit vector perpendicular to the 2D plane. Band theory derives these bands and band gaps by examining the allowed quantum mechanical wave functions for an electron in a large, periodic lattice of atoms or molecules. The formation of bands is mostly a feature of the outermost electrons (valence electrons) in the atom, which are the ones involved in chemical bonding and electrical conductivity. The inner electron orbitals do not overlap to a significant degree, so their bands are very narrow. Figure 2.4 Shows, as an example, the DOS and band structures of

the black phosphorous. Band theory has been successfully used to explain many physical properties of solids, such as electrical resistivity and optical absorption, and forms the foundation of the understanding of all solid-state devices (transistors, solar cells, etc.).
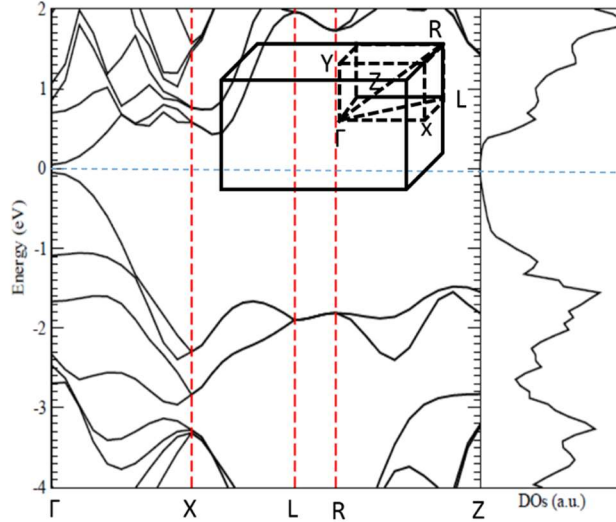
Figure 2.4 The band structure and the DOS of black phosphorus, the first Brillouin zoon is inserted. The blue dash line represents the Fermi level, the red dash lines represent the special K points in the insert.

2.3.4   Mechanical properties

Mechanical properties characterize how the structures response to the strain exerted by various stresses. Analogous to the first and second Piola-Kirchhoff Stress in 3D [122], the 2D nominal stress P_{iJ} and 2D membrane stress tensor S_{IJ} [122] are defined as,

$$P_{iJ} = \frac{\partial \Psi}{\partial F_{iJ}}, S_{IJ} = \frac{\partial \Psi}{\partial E_{IJ}} \tag{2-17}$$

Here, the strain energy density function Ψ as a function of the strain ε along different directions is defined by

$$\Psi = \frac{E_{total}(\varepsilon) - E_{total}(0)}{A_{cell}}, \tag{2-18}$$

where $E_{total}(\varepsilon)$ is the total energy per atom with the strain, $E_{total}(0)$ is the total energy per atom without the strain, A_{cell} is the area of the unit cell at zero strain, respectively. The deformation gradient tensor $\vec{F}$ is given by $F_{i,J} = \frac{\partial x_i}{\partial X_J}$, in which ∂X_J ($J = 1, 2$ because 2D sheet has only two in-plane components) is the infinitesimal segment along J direction at a reference state and ∂x_i is the segment along i direction at the deformed state. Considering homogeneous deformation of a 2D structure, a uniaxial stretch is applied in the 1-direction, we have $F_{11} = \frac{\partial x_1}{\partial X_1} = \lambda$; $F_{22} = \frac{\partial x_2}{\partial X_2} = \lambda$; $F_{12} = F_{21} = F_{31} = F_{32} = 0$. Furthermore, the Green-Lagrange strain tensor E_{IJ} [122] which used to evaluate the deformation is defined as

$$E_{JK} = \frac{1}{2}(F_{iJ}F_{iK} - \delta_{JK}), \delta = \begin{cases} 0, & J \neq K \\ 1, & J = K \end{cases} \tag{2-19}$$

The nominal strain ε in the 1-direction is defined as $\varepsilon = \lambda - 1$. Hence, for the uniaxial stretch in the 1-direction, we have,

$$P_{11}(\varepsilon) = \frac{\partial \Psi}{\partial F_{11}} = \frac{\partial \Psi}{\partial \lambda} = \frac{\partial \Psi}{\partial \varepsilon}\frac{\partial \varepsilon}{\partial \lambda} = \frac{\partial \Psi}{\partial \varepsilon} \tag{2-20}$$

$$S_{11}(\varepsilon) = \frac{\partial \Psi}{\partial E_{11}} = \frac{\partial \Psi}{\partial \varepsilon}\frac{\partial \varepsilon}{\partial E_{11}} = \frac{\partial \Psi}{\partial \varepsilon}\left(\frac{1}{1+\varepsilon}\right) = \frac{P_{11}}{1+\varepsilon} \tag{2-21}$$

The stress-strain relationship for 2D sheet under uniaxial stress [123] is given by,

$$S_{11} = Y^{2D}E_{11} + D^{2D}E_{11}^2 \tag{2-22}$$

From which the 2D first-order (effective linear) Young's modulus at infinitesimal strain $Y^{2D} = \frac{\partial S_{11}}{\partial E_{11}}$, and the second-order (effective nonlinear) elastic modulus $\frac{\partial^2 S_{11}}{\partial E_{11}^2} = 2D^{2D}$ can be analyzed in details. Example for graphene is shown in Figure 2.5, the stresses along the armchair direction are slightly stronger than that along the zigzag direction, showing strong anisotropic nature. The graphene could sustain strong load (*i.e.,* 20%) in both armchair and zigzag directions. Obtained 2D Young's modulus at infinitesimal strain and the second-order (effective nonlinear) elastic modulus are in good consistent with the experimental observation (see Table1). Furthermore, the extraordinarily different behavior for compression and extension is demonstrated for the first time.
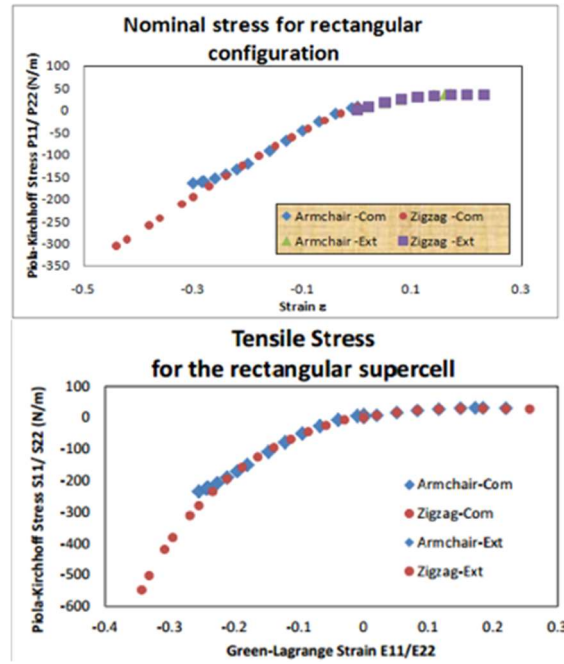
Figure 2.5 Upper panel: Piola-Kirchhoff Stress P_{ij} as functions of strain ε; lower panel: Piola-Kirchhoff Stress S_{ij} as functions of strain E_{ij}. The negative strain indicates graphene was compressed; and positive, extended. P_{11}, S_{11} are the stresses, and E_{11} is the strain along the armchair direction. P_{22}, S_{22} and E_{22} are the stresses along the zigzag direction.

Table 1. Experimental observation and theoretical calculation of the elastic modulus of graphene [123-127]

Calculated and measurement results	Y^{2D} (Nm^{-1})	D^{2D}(Nm^{-1})
Along the armchair direction	356.3	-1190
Along the zigzag direction	414.7	-1833
AFM Experimental Data [a][122]	340±40	-690±120
ab initio calculation [123]	345	N/A
Tersoff-Brenner calculation [124]	235	N/A
ab initio calculation [125]	350	N/A
Tight binding+ continuum elasticity theory [126]	312	-582.9

2.4   SCED-LCAO approach

2.4.1   SCED-LCAO Hamiltonian

The SCED-LCAO Hamiltonians developed in our group is constructed within the framework of a linear combination of atomic orbitals that allows a coherent treatment of the self-consistent determination of the charge redistribution and the environment-dependent multi-center interactions. Within the framework of LCAO, the total wave function is made up of a linear combination of orbitals of isolated atoms and applied in the generalized eigenvalue problem.

$$|\psi_\lambda(\vec{r})\rangle = \sum_i \sum_\alpha C_{i\alpha} |\varphi_\alpha(\vec{r} - \vec{R}_i)\rangle \tag{2-23}$$

$$\langle\varphi_{i\alpha}|\hat{H}|\varphi_{j\beta}\rangle C_{i\alpha}^\lambda = \epsilon_\lambda C_{i\alpha}^\lambda \langle\varphi_{i\alpha}|\varphi_{j\beta}\rangle \tag{2-24}$$

where the overlap $S_{i\alpha,j\beta} = \langle\varphi_{i\alpha}|\varphi_{j\beta}\rangle$.

Similar to DFT, SCED-LCAO Hamiltonians were built based on the one-particle approximation. Within the framework of LCAO, the on-site and off-site Hamiltonian matrix elements can be written as,

$$H_{i\alpha,i\alpha} = \varepsilon_{i\alpha}^0 + u_{i\alpha}^{intra} + u_{i\alpha}^{inter} + v_{i\alpha}^{inter}$$

$$H_{i\alpha,j\beta} = \frac{1}{2}(\varepsilon_{i\alpha}^0 + \varepsilon_{j\beta}^0 + u_{i\alpha}^{intra} + u_{j\beta}^{intra} + u_{i\alpha}^{inter}$$

$$+ u_{j\beta}^{inter} + v_{i\alpha}^{inter} + v_{j\beta}^{inter})S_{i\alpha,j\beta} \tag{2-25}$$

Where the ε terms are the kinetic energies, u^{intra} terms are interactions of the onsite electron with other electrons associated with the same ionic site, u^{inter} terms are interactions of the onsite electron with other electrons associated with other ionic site, and v^{inter} terms are interactions of the onsite electron with ions at other sites. In the SECD-LCAO scheme, these terms are represented by,

$$\varepsilon_{i\alpha}^0 = \varepsilon_{i\alpha} - Z_i U_i + \sum_{k \neq i} W_{i\alpha}(R_{ik})$$

$$u_{i\alpha}^{intra} = N_i U_i$$

$$u_{i\alpha}^{inter} + v_{i\alpha}^{inter} = \sum_{k \neq i}\{N_k V_N(R_{ik}) - Z_k V_z(R_{ik})\} \tag{2-26}$$

The diagonal and off-diagonal terms of the electronic Hamiltonian matrix elements can be rewritten represented by,

$$\widehat{H}_{i\alpha,i\alpha} = \varepsilon_{i\alpha} + \sum_{k \neq i} W_{i\alpha}(R_{ik}) + (N_i - Z_i)U_i + \sum_{k \neq i}\{N_k V_N(R_{ik}) - Z_k V_z(R_{ik})\}$$

$$\hat{H}_{i\alpha,j\beta} = \frac{1}{2}[\varepsilon'_{i\alpha} + \varepsilon'_{j\beta}]K(R_{ij})S_{i\alpha,j\beta}(R_{ij}) + \frac{1}{2}[\sum_{k\neq i} W_{i\alpha}(R_{ik}) +$$

$$\sum_{k\neq j} W_{j\beta}(R_{jk})]K(R_{ij})S_{i\alpha,j\beta}(R_{ij}) + \frac{1}{2}[(N_i - Z_i)U_i + (N_j - Z_j)U_j]S_{i\alpha,j\beta}(R_{ij}) +$$

$$\frac{1}{2}[\sum_{k\neq i}\{N_kV_N(R_{ik}) - Z_kV_z(R_{ik})\} + \sum_{k\neq j}\{N_kV_N(R_{jk}) - Z_kV_z(R_{jk})\}]S_{i\alpha,j\beta}(R_{ij}) \quad (27)$$

In the new diagonal and off-diagonal Hamiltonian matrix, the first term includes the two-center interaction term followed by the expression with the W term that considers the possible occupation of the excited local orbitals in an atomic aggregation and the effects of interactions with neighboring atoms. The on-site electron-electron interactions in the third term provide the framework for the charge redistribution calculation. The last terms indicate the environment dependence and multi-center interactions.

The total energy of an atom of the system at a given site is:

$$E_{total} = \sum_{\lambda}^{occ} n_\lambda \varepsilon_\lambda + \frac{1}{2}\sum_i (Z_i^2 - N_i^2)U_i - \frac{1}{2}\sum_i \sum_{j\neq i} N_i N_j V_N(R_{ij}) +$$

$$\frac{1}{2}\sum_i \sum_{j\neq i} Z_i Z_j \frac{E_0}{R_{ij}} \quad (2\text{-}28)$$

and the lth component (where $l = x$, y or z) of the force acting on the atom at a given site k is:

$$F_k^l = -\sum_{\lambda}^{occ} \sum_{i\alpha} \sum_{j\beta} n_\lambda (C_{i\alpha}^\lambda)^* C_{j\beta}^\lambda \left[\frac{\partial H_{i\alpha,j\beta}^{SCED-LCAO}}{\partial x_k^l} - \varepsilon_\lambda \frac{\partial S_{i\alpha,j\beta}}{\partial x_k^l}\right] +$$

$$\frac{1}{2}\sum_i \sum_{j\neq i} \frac{\partial\left(N_i N_j V_N(R_{ij})\right)}{\partial x_k^l} - \frac{1}{2}\sum_i \sum_{j\neq i} Z_i Z_j \frac{\partial\left(\frac{E_0}{R_{ij}}\right)}{\partial x_k^l} \quad (2\text{-}29)$$

The charge projected on each site will be obtained from the solution of the eigenvalue problem

$$N_i = \sum_{\lambda}^{occ} \sum_\alpha \sum_{j\beta} C_{i\alpha}^\lambda C_{j\beta}^\lambda n_\lambda S_{i\alpha,j\beta} \quad (2\text{-}30)$$

The self-consistency of SCED-LCAO approach is illumined by the following calculation loop (as seen in Figure 2.6). For a given system with charge N_i^{in}, we first calculate the SCED Hamiltonians, following by solving for the eigenvalue problem. Base on the solution of the eigenvalue problem, the new charge N_i^{out} can be obtained and compared with N_i^{in}. Then continue the loop until the difference between N_i^{out} and N_i^{in} is very close to zero or reach the cut-off setup.
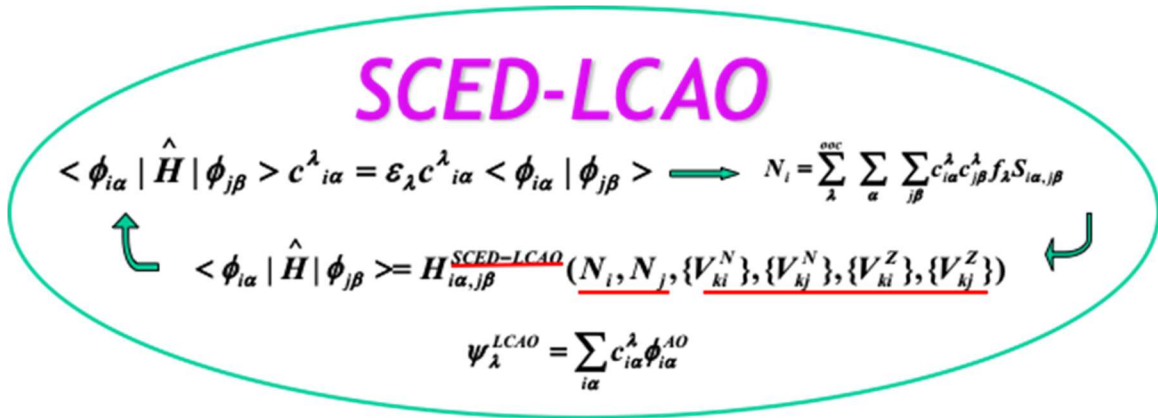
Figure 2.6 The framework of the SCED-LCAO approach

2.4.2   Parameters in constructing SCED-LCAO Hamiltonian

As shown in equation (27), the SCED-LCAO Hamiltonian is constructed by a set of parameterized functions and parameters, where $\varepsilon'_{i\alpha}$ and $\varepsilon'_{j\beta}$, and U are parameters; and $K(R_{ij})$, $S_{i\alpha,j\beta}(R_{ij})$, $W_{i\alpha}(R_{ik})$, $V_N(R_{ik})$ and $V_z(R_{ik})$ are parametric functions.

The overlap matrix $S_{i\alpha,j\beta}(R_{ij})$ is expressed as,

$$S_{ij,\tau}(R_{ij}) = \left(A_{ij,\tau} + B_{ij,\tau}R_{ij}\right)\frac{1+e^{-\alpha_{i\alpha,\tau}d_{ij,\tau}}}{1+e^{-\alpha_{i\alpha,\tau}(d_{ij,\tau}-R_{ij})}} \qquad (2\text{-}31)$$

In which τ refers to the different overlapping orbitals, for a system with only s and p orbitals, τ can be $ss\sigma, sp\sigma, pp\sigma$ and $pp\pi$. For $ss\sigma$ hybridization, $A_{ij,\tau}$ is 0, and for others $A_{ij,\tau}$ is 1. For a heterogeneous system, a weighting factor δ_{ij} was introduced to characterize the overlap matrix elements.

Then four groups of parameters in the overlap matrix can be rewritten as,

$$A_{ij,\tau} = \frac{\delta_{ij}|\varepsilon_{i,\mu}|A_{i,\tau} + (1-\delta_{ij})|\varepsilon_{j,v}|A_{j,\tau}}{\delta_{ij}|\varepsilon_{i,\mu}| + (1-\delta_{ij})|\varepsilon_{j,v}|} \;;\; \alpha_{ij,\tau} = \frac{\delta_{ij}|\varepsilon_{i,\mu}|\alpha_{i,\tau} + (1-\delta_{ij})|\varepsilon_{j,v}|\alpha_{j,\tau}}{\delta_{ij}|\varepsilon_{i,\mu}| + (1-\delta_{ij})|\varepsilon_{j,v}|}$$

$$B_{ij,\tau} = \frac{\delta_{ij}|\varepsilon_{i,\mu}|B_{i,\tau} + (1-\delta_{ij})|\varepsilon_{j,v}|B_{j,\tau}}{\delta_{ij}|\varepsilon_{i,\mu}| + (1-\delta_{ij})|\varepsilon_{j,v}|} \;;\; d_{ij,\tau} = \frac{\delta_{ij}|\varepsilon_{i,\mu}|d_{i,\tau} + (1-\delta_{ij})|\varepsilon_{j,v}|d_{j,\tau}}{\delta_{ij}|\varepsilon_{i,\mu}| + (1-\delta_{ij})|\varepsilon_{j,v}|} \qquad (2\text{-}32)$$

where i and j the sites occupied by the atom, μ and v are the orbitals of the atom. δ_{ij} has values in the range $0 < \delta_{ij} < 1$. When the two sites i and j are occupied by the same type of atom, $\delta_{ij} = \frac{1}{2}$.

The Two center interaction term's dependence on the separation R_{ij} is described by the scaling function,

$$K(R_{ij}) = K_{ij}^0 e^{\alpha_{ij,k}R_{ij}} \qquad (2\text{-}33)$$

Where,

$$\alpha_{ij,K} = \delta_{ij}\alpha_{i,K} + (1 - \delta_{ij})\alpha_{j,K} \qquad (2\text{-}34)$$

The $W_{i\alpha}(R_{ij})$ term is used as an additional term on minimal basis sets when an aggregate of atoms exist, and it tends to zero as the separation approaches infinity.

$$W_{i\alpha}(R_{ij}) = W_{i\alpha}^0 e^{-\alpha_{i\alpha,w}R_{ij}} \qquad (2\text{-}35)$$

The electron-electron interaction $V_N(R_{ij})$, electron-ion interaction $V_Z(R_{ij})$ and short-range function $\Delta V_{i,N}(R_{ij})$ define the potential functions in SCED-LCAO Hamiltonian. Their respective expressions are:

$$V_N(R_{ij}) = \delta_{ij}V_{i,N}(R_{ij}) + (1 - \delta_{ij})V_{j,N}(R_{ij})$$

$$V_Z(R_{ij}) = \delta_{ij}V_{i,Z}(R_{ij}) + (1 - \delta_{ij})V_{j,Z}(R_{ij}) \qquad (2\text{-}36)$$

where:

$$V_{i,N}(R_{ij}) = V_{i,Z}(R_{ij}) + \Delta V_{i,N}(R_{ij})$$

$$V_{i,Z}(R_{ij}) = \frac{E_0}{R_{ij}}\left[1 - (1 + B_{i,Z}R_{ij})e^{-\alpha_{i,Z}R_{ij}}\right] \qquad (2\text{-}37)$$

$$\Delta V_{i,N}(R_{ij}) = (A_{i,N} + B_{i,N}R_{ij})\frac{1 + e^{-\alpha_{i,N}d_{i,N}}}{1 + e^{-\alpha_{i,N}(d_{i,N}-R_{ij})}}$$

In summary, totally 25 parameters needed to be optimized for each element include ε'_s; ε'_p; α_K; $B_{ss\sigma}$; $B_{sp\sigma}$; $B_{pp\sigma}$; $B_{pp\pi}$; $\alpha_{ss\sigma}$; $\alpha_{sp\sigma}$; $\alpha_{pp\sigma}$; $\alpha_{pp\pi}$; $d_{ss\sigma}$; $d_{sp\sigma}$; $d_{pp\sigma}$; $d_{pp\pi}$; W_s^0; W_p^0; $\alpha_{s,w}$; $\alpha_{p,w}$; U_i; $A_{i,N}$; $B_{i,N}$; $B_{i,Z}$; $d_{i,N}$ and $\alpha_{i,Z}$. The SCED-LCAO Hamiltonian parameters are obtained by fitting them to an accurate ab-initio database which contains properties of clusters and bulks. A thorough optimized and robust test of SCED-LCAO Hamiltonian parameters needs to be completed to ensure its transferability and reliability.

2.4.3   Strategies in developing of the SCED-LCAO Hamiltonian for a specific element

To develop the transferable and reliable SCED-LCAO Hamiltonian for a specific element, we first built up the databases which include the properties of small clusters and

the bulk phases obtained by ab-initio calculations, and then optimize the parameters by fitting the calculated SCED-LCAO results to database fairly well until reaching a low residual. To confirm the transferability, we choose the best set of parameters obtained in the fitting process and perform the robustness checks with larger and complex systems (*e.g.,* larger clusters, surfaces, layers and other nanostructures). The details of the fitting processes are described in the following steps.

Step 1. Buildup the database

As we mentioned above, the SCED Hamiltonian have 25 parameters for each element, which means more than 25 properties are needed in the database to fit parameters. Considerable amount of resources (both time and computer cost) is required during the fitting process. On the other hand, the stabilized geometric parameters and associated energy are the most fundamental properties for any clusters and bulks. Due to these considerations, we built up the database with more than 25 properties by mainly considering the binding energy and geometric parameters characterizing the symmetry.

The first principle methods implemented in the commercial packages GAUSSIAN03 and VASP were used to create a database. The Gaussian basis based GAUSSIAN03 was used for small clusters with finite of atoms; and the plane wave basis based VASP code was used for the bulk with periodic boundary conditions.

Step 2. Optimizing SCED-LCAO Hamiltonian

The parameters characterizing our SCED-LCAO Hamiltonian are determined by an efficient global optimization procedure against an appropriately chosen database, by adapting a local least-squares algorithm, the Marquardt-Levenberg algorithm [128] to the global problem. We start from an initial set of the parameters with physically intuitive guess and seek the best set of parameters by optimizing the parameters through the fitting code which was written by the CMT Group at the University of Louisville. During the fitting process, we set the properties obtained by GAUSSIAN03 or VASP in the database as the standard properties, optimize our SCED-LCAO results to the standard results. A residual or objective function R which depends on the parameters S_i of the SCED-LCAO Hamiltonian, and for which the minimum value of R is interpreted as the best value. We use a least-squares sum of the differences between the calculated properties P_{calc} and the reference values P_{ref}. $R(S_i) = \sqrt{\frac{1}{N_P} \sum_k \left(P_{weigh}^k \frac{P_{calc}^k - P_{ref}^k}{P_{weigh}^k} \right)^2}$. This expression also includes the characteristic scale P_{scale} of each property, a weight factor P_{weig} which represents the relative importance of each property, and the total number of properties N_P. The use of the scale, weight, and number of properties allows for the interpretation of the residual as the average relative deviation of the calculated values from the reference values.

Step 3. Reliability and robustness

Once a best set of parameters with low residual and reasonable Hamiltonian and Overlap was obtained, a robust test is needed to examine whether the fitted parameters are transferable. The reason is that the database cannot contain all properties of the element. Thus, structures with more complicated geometric, physic, and chemical feature are needed as robust check.

We usually check more than one larger and more complicated system by using the SCED-LCAO method and compared to DFT results. A manual adjustment of the parameters or an expansion of database may be needed based on the robustness test results. The modified parameters will be sent back to the fitting process and to optimize them again until we finally obtain the best set of reliable and transferable parameters for the SCED-LCAO Hamiltonian for a specific element.

In summary, the fitting process includes the following steps:

1, Build up a database which contains the structural properties and energies of small clusters and bulks in the fitting code.

2, Set up an initial guess of parameters based on the physical intuition.

3, Optimize the parameters until a best set of parameters is obtained which meets the requirement of low residual.

4, Preform the robust check with larger and complex systems. If the SCED-LCAO results are consistent with the DFT results, we obtain a set of reliable and transferable parameters. If not, we modify some parameters or add more properties to the database, then go back to step 3.

The third and fourth steps are the key to obtain the best optimized parameters. We should always keep an eye on the following two parts: Overlap and Hamiltonian curves and the physical meaning of all parameters. They are the basics of the optimized parameters.

CHAPTER III

FIRST PRINCIPLE PREDICTION OF UNIQUE ANISOTROPIC PHYSICAL

PROPERTIES OF SANDWICHED 2D PHOSPHIDE BINARY COMPOUNDS

SHEETS

3.1   Introduction

Exploring unknown 2D nanomaterials that have targeted physical properties for
nanoscale electronic and optoelectronic devices is urgently demanded in 2D nanomaterial
research in the post-graphene era [7-26]. Tremendous interests were mainly focused on the
discovery of analogous 2D nanomaterials from their layered bulk counterparts (*i.e.*, those
with Van der Waals interaction between layers). Those newly discovered 2D materials
were energetically preferential and indeed show their unique electronic, optical, chemical,
and mechanical properties, indicating their remarkable promising applications for
nanoelectronics, optics, catalysts, etc. [7-9, 27-33, 39-42]. Simutaneously, the discovery of
other possible types of 2D nanomaterials with no corresponding layered bulk counterpatrts
in nature also attracted extensive interesting.   One of the big breakthroughs was the
prediction of the elemental 2D sheets including silicene and germanene [10, 13-26].
Theoretical calculations pointed out that they are dynamically stable as free standing sheets
with low buckled honeycomb lattice structures (*i.e.*, the two sublattices are relatively
shifted in the direction perpendicular to the atomic plane with buckling of 0.44 Å for
silicene and 0.67 Å for germanene, respectively) [19-21]. Several experimental results

found that, instead of free standing sheets, they can be realized on metal substracts [23-25] Borophene, another new member of elemental monolayers with various patterns in structure, was also theoretically predicted quite recently [61, 62], and has been successfully synthesized on the Ag (111) surface with novel properties of Dirac fermions [60, 63].

These new discoveries stimulated us to explore other unknown 2D materials, in particular, the unkonwn 2D binary compounds such as SiC, GeC, and III-V binary compounds [9, 12, 58, 59]. Low buckled honeycomb InP and GaP monolayers were first predicted by H. Sahin *et al*. [12] when they studied monolayer honeycomb structures of group-IV elements and III-V binary compounds. Their density functional theory (DFT) calculations showed that those low buckled honeycomb InP and GaP binary compounds have indirect energy bandgaps in the range of 1~2 eV, indicating their possible applications for optoelectronic devices. However, it is not clear, whether these low buckled honeycomb structures are the only form of the 2D GaP/InP binary compound sheets, and if there exist any other allotropes of 2D GaP/InP binary compounds sheets which are even energetically more stable.

Recently, we carried out a systematic study on seeking stable and energetically preferential 2D monalayers of GaP and InP binary compounds sheets. Our first principle molecular dynamics simulations show that, in addition to the low buckled honeycomb structures, a new 2D monolayer structure can be obtained by bulk truncation along a special orientation, called 'armchair truncation'. These newly discovered allotropes of 2D GaP/InP binary compounds possess high puckered and sandwiched monolayer structures with orthorhombic lattice symmetry, and are energetically much stable than the previously

predicted [12] low buckled honeycomb GaP/InP sheets. More interesting, they possess strong anisotropic electronic and mechanical properties. Their fundamental bandgaps are wider than those of low buckled honeycomb sheets and even wider than their bulk counterparts. Such bandgaps are found to be tunable under the strain along armchair/zigzag direction, and a transition from the indirect to the direct band gap could occur along particular orientations.

3.2   Computational methods

In the processes of seeking new allotropes of 2D monolayer GaP/InP binary compounds, we employed the DFT [43, 44] framework, as implemented in the VASP [100], and performed the structure optimization, dynamic stability analysis, and electronic and mechanical properties calculations. The electron-ion interactions were described by the PAW [102], while electron exchange-correlation interactions were treated by the GGA [99] in the scheme of PBE [103]. The structural relaxation was performed using Congregate-Gradient algorithm [115] implemented in VASP. The periodic boundary conditions were chosen in the layered plane with a vacuum space of 15 Å between adjacent layers to avoid any mirror interactions. An energy cutoff was set to be 500 eV for the plane wave basis in all calculations, and the criteria for the convergences of energy and force in relaxation processes were set to be 10^{-5} eV and 10^{-4} eV/Å, respectively. A 1×1 rectangular primitive cell was chosen to study the 2D GaP and InP monolayer structures, and the Brillouin zones (BZ) were sampled by $25 \times 25 \times 1$ K-point meshes generated in accordance with the Monkhorst-Pack scheme [129] in the optimization and band structure calculations.

A benchmark for zinc blende bulk GaP/InP crystalline structures was carried out (see the last columns of Tables 2 and 3). The optimized lattice constants are 5.53 Å for bulk

GaP and 6.02 Å for bulk InP, respectively, which are only ~ 1.47% for GaP and 2.38% for InP overestimated compared to the experimental measurements [130]. Calculated cohesive energies (i.e., -8.54 eV/pair for GaP and -7.78 eV/pair for InP, respectively), on the other hand, is about 1 eV per pair lower than the experimental values, which are typical in DFT-GGA calculations. It is also common that calculated DFT band gaps (i.e., ~1.52 eV for GaP and ~ 0.38 eV for InP, respectively) are ~ 1 eV underestimated compared with the experimental results (i.e., 2.26 eV for GaP and 1.34 eV for InP), mostly due to the lack of self-energies corrections in DFT calculations. Such big errors in the DFT band gap calculations were reduced using HSE06 [111] as implemented in VASP. The calculated HSE06 band gaps are 2.37 eV for bulk GaP and 1.10 eV for bulk InP, resulting in a mean absolute error of only ~ 0.11 eV and ~0.24 eV, as compared with the experimental measurements.

3.3   Anisotropic crystalline structures

The most stable phase of GaP/InP binary compounds in nature is the zinc blende crystalline structure, followed by the wurtzite structure. In both phases, Ga (In) and P atoms prefer to form sp^3 type of hybrid orbitals. Based on this chemical bonding nature, we proposed to search the possible existence of unknown allotropes of 2D GaP/InP binary compounds by truncating the bulk GaP/InP, *e.g.,* the zinc blende structure, along with certain orientations. As illustrated in Figure 3.1 (a), the zinc blende crystalline structures of GaP and InP binary compounds along (111) orientation can be viewed as a series of bilayers aligned with ABC stacking sequences and interacted by strong Coulomb interactions, in which the yellow balls represent P atoms, and the green balls represent the Ga/In atoms, respectively. When a zigzag truncation is performed (shown by the red-

dashed box in Figure 3.1 (a)), a buckled bilayer sheet was constructed (shown in Figure 3.1 (b)). During the structural relaxation, this initial configuration was then stabilized to a so-called low buckled honeycomb structure with the buckling of 0.36 Å and 0.54 Å for GaP and InP sheets, respectively, consistent with the previous results predicted by H. Şahin *et al.* [12]. Alternatively, when an armchair truncation is performed (shown by the blue-dashed box in Figure 3.1(a)), a puckered bilayer sheet, analogous to phosphorene, was constructed (shown in Figure 3.1 (c)). Very interesting, such initial configuration underwent a structure transition during the structural relaxation.
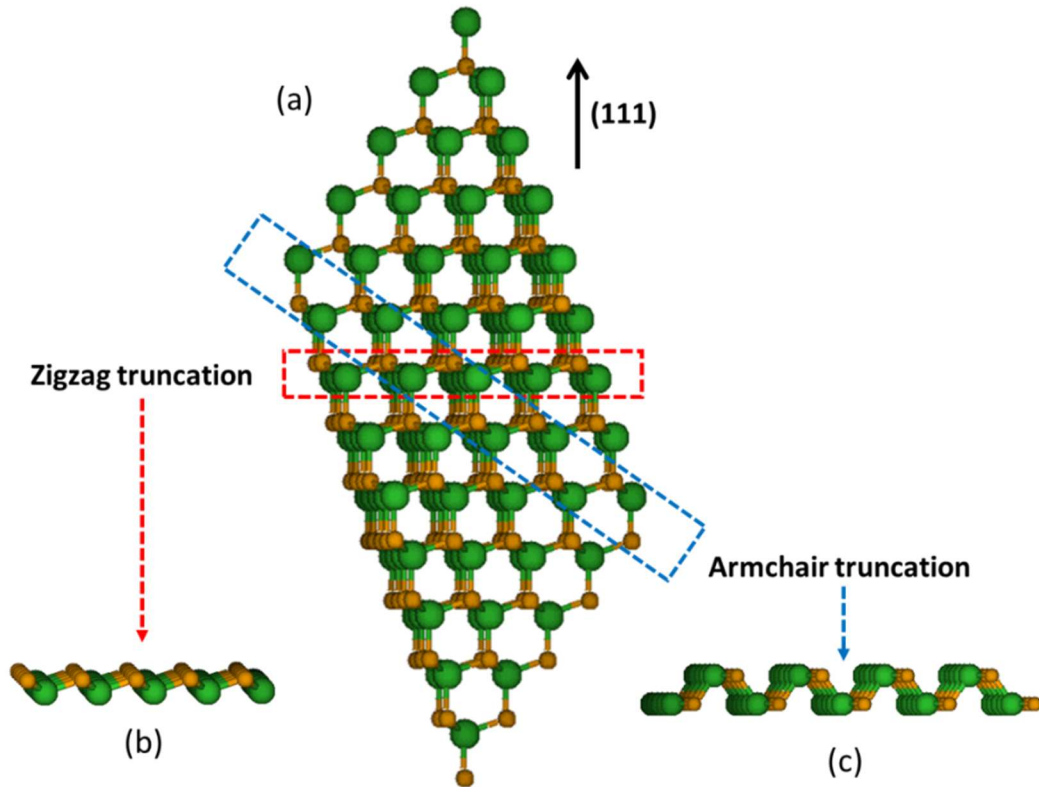
Figure 3.1 (a) Schematic illustrations of the zinc blende GaP/InP crystalline structures along (111) orientation; (b) a bilayer sheet truncated along the zigzag direction (indicated by the red-dashed box in (a)); and (c) a bilayer sheet truncated along the armchair direction (indicated by the blue-dashed box in (a)).

41

The corresponding molecular dynamics process is illustrated in Figure 3.2 (a)-(c). It is found that Ga/In atoms initially located on the ridge and in the valley (shown in Figure 3.2 (a)) move towards each other vertically during the relaxation (shown in Figure 3.2 (b)), and finally, the bilayer sheet stabilized to a highly puckered structure where hexagons form a semi-chair type of shape (shown in Figure 3.2 (c)). In Figure 3.2 (a), the middle structure is the side view seen from the front and the bottom structure is the side view seen from the left, respectively. In Figure 3.2 (b), we use InP monolayer as an example, shows the total energy of the 2D InP monolayer as a function of MD steps. Inserts in Figure 3.2 (b) are the side views corresponding to some intermediate MD steps (marked with stars), demonstrating the evolution of the structure during the relaxation. The two open arrows indicate the structures at the initial (shown in (a)) and the final (shown in (c)) MD steps, respectively. The top and side views of the stabilized structure are shown in Figure 3.2 (c). The black-dashed box represents the rectangular primitive unit cell with lattice constants a and b; b_1 and b_2 denote two types of Ga-P/In-P bonds; α_1, α_2, and α_3 denote three types of angles; and Δz_1 and Δz_2 denote two buckling parameters, respectively.
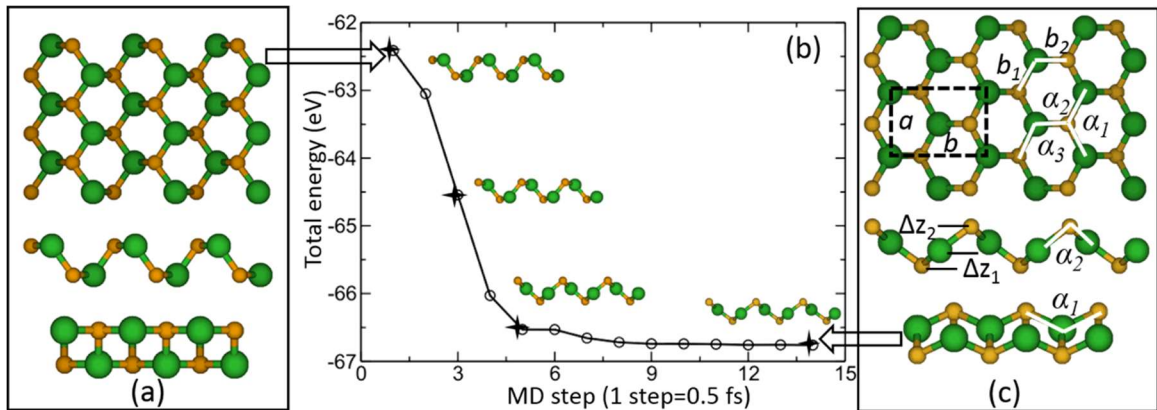
Figure 3.2 (a) Schematic illustrations of the top and two side views of the proposed initial configurations of 2D GaP/InP monolayers (illustrated in Figure 3.1 (c)); (b) The total

energy of the 2D InP monolayer as a function of (MD) steps; and (c) Schematic illustrations of the top and two side views of the stabilized high puckered orthorhombic 2D GaP/InP monolayers.

To provide more fundamental guidelines for experimental synthesis, we conducted various computational simulations and found that by substituting P atom alternatively with Ga/In atoms on phosphorene, the puckered lattice structures can automatically transform to the high puckered orthorhombic lattice (see Figure 3.3). Recently, synthesizing 2D binary compounds using graphene or *h*-BN as host materials become possible by plasma assisted substitutional doping CVD [131-133], in particular, for those binary compounds whose bulk counterparts have strong cohesive bonds between layers. It may be a possible way to synthesise the 2D buckled honeycomb GaP/InP layers on blue phosphorene which was predicted theoretically [134] but has not yet realized experimentally. Promoted by this newly developed technique, we proposed here to take phosphorene (which has been successfully synthesized by mechanical exfoliation) as the host material and search if there exists another unknown allotrope of 2D GaP and InP binary compounds monolayer structures by alternatively substituting P atoms with Ga/P atoms on phosphorene (as shown in Figure 3.3 (b)). These structures are then fully relaxed using GGA-PAW-PBE in VASP. During the relaxation, P atoms slowly move away from the middle of the layer while Ga/In atoms move close to the middle of the layer, and finally, the structures stabilized to, instead of the buckled honeycomb structure, a three-atom-thick of V-type layer (as shown in Figure 3.3 (c)), which is same as the fully relaxed layer truncated from zinc blende GaP/InP (in Figure 3.2 (c)).
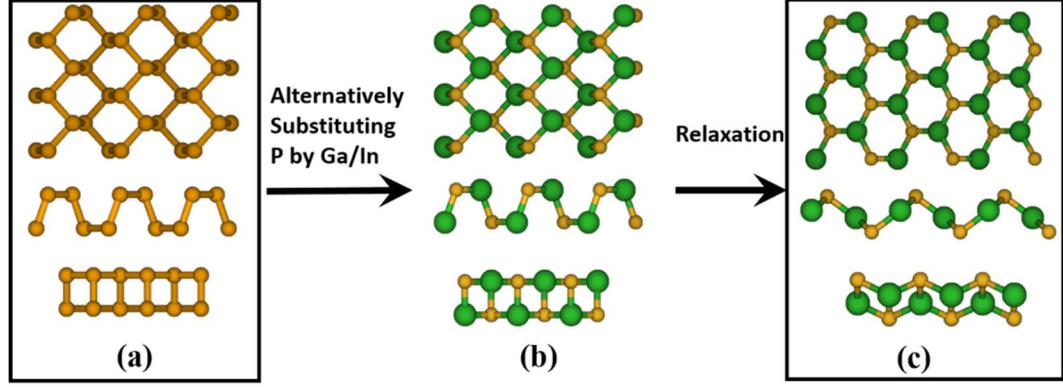
Figure 3.3 Schematic illustration of the fundamental guidance for synthesizing high puckered orthorhombic GaP/InP monolayers from phosphorene: (a) top and side views of phosphorene, (b) alternatively substituting Ga or In atoms on phosphorene, and (c) a high puckered orthorhombic GaP/InP monolayer is realized after a full relaxation.

Different from the low buckled honeycomb 2D GaP/InP with rhombohedral lattice symmetry and three-fold rotation symmetry C_3, the new 2D allotropes of GaP/InP binary compound possess orthorhombic lattice symmetry which belong to the space group of P11m and point group of C_s^1. The primitive translational vectors A_1 (a, 0, 0) and A_2 (0, b, 0) are given in terms of two optimized lattice constants a and b. The rectangular primitive cell contains four atoms with two nearly equaled Ga-P/In-P bonds (b_1, b_2) and three different angles (α_1, α_2, α_3). Their positions are given by

$$(0,0,0), \quad (\frac{a}{2},\frac{b}{2}-v\Delta z_2,\Delta z_1), \quad (\frac{a}{2},\frac{b}{2},\Delta z_1+\Delta z_2), \quad (0,b-v\Delta z_2,\Delta z_2) \tag{3-1}$$

where $v = \sqrt{\left(\frac{b_2}{\Delta z_2}\right)^2 - 1}$, and Δz_1 and Δz_2 are buckling parameters which determine the total buckling $\Delta z_1 + \Delta z_2$.
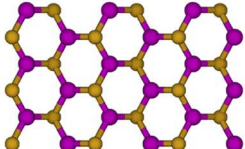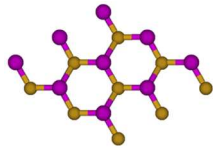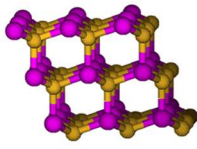
Optimized structural properties of the newly obtained 2D GaP/InP monolayer structures (referred as high puckered orthorhombic monolayer hereafter), their cohesive energies, and bandgaps (calculated with DFT and HSE06, respectively) are listed in Table 2 and 3, respectively. In Table 2 and 3, b_1, b_2, α_1, α_2, and α_3 are the bond lengths and angles of the high puckered orthorhombic GaP monolayer, respectively, as shown in Figure 3.2 (c); numbers in parentheses in the fourth column are experimental results [130]. The corresponding values for the low buckled honeycomb 2D GaP/InP monolayers, as well as their bulk counterparts, are also listed for comparisons. It is found that the two bond lengths (b_1 and b_2 in Figure 3.2 (c)) are nearly equal (*i.e.*, 2.32 Å and 2.33 Å for GaP, and 2.53 Å and 2.54 Å for InP, respectively). The three angles, on the other hand, are quite different and clearly demonstrate the anisotropic behaviors in these new high puckered orthorhombic structures. The first angle along the zigzag direction (*i.e.*, 110.2^0 for GaP and 108.6^0 for InP) is close to the tetrahedral angle of 109^0. The second one, characterising the dihedral angle, is 99.3^0 for GaP and 97.5^0 for InP, indicating a high buckling (*i.e.*, $\Delta z_1 + \Delta z_2$ is 2.14/2.46 Å for GaP/InP monolayers, which is about 5.94/4.56 times higher than those of the low buckled honeycomb GaP/InP monolayers). The third one on the semi-chair type of hexagon plane formed by the two Ga/In atoms and three P atoms is 124.6^0 for GaP and 125.5^0 for InP, slightly larger than the angle of the flat hexagon (120^0). The characteristic of the three angles represents a mixture of the sp^3-like and sp^2-like hybridizations. Among the four sp^3-like orbitals, three of them bond with three nearest-neighbor atoms and the remaining one is perpendicular to the atomic layers of the 2D high puckered orthorhombic GaP/InP binary compounds. The π-like orbitals in sp^2-like hybridization, on the other hand,

are perpendicular to the semi-chair type of hexagon planes. In addition to their unique structural properties, another interesting point is their energetics.
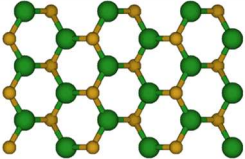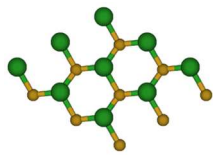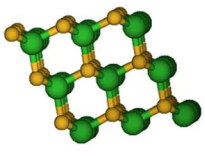
The cohesive energies per GaP/InP pair (defined as $E_C = E_{total} - E_{Ga/In} - E_P$, where E_{total} is the total energy of the GaP/InP sheet per GaP/InP pair, $E_{Ga/In}$ and E_P are the energies of single Ga/In and P atoms, respectively) are ~0.144 and 0.173 eV/pair lower than those of the low buckled honeycomb 2D GaP and InP structures (see the 6th row in Table 2 and 3), demonstrating that these newly predicted 2D GaP and InP monolayer structures are energetically preferential. Namely, the 2D GaP/InP monolayers prefer to maintain with high puckering, instead of low buckling. This tendency may be interpreted in terms of Jahn-Teller effect as the degeneracy at top valence band of the low buckled honeycomb 2D GaP/InP sheets [12] is removed in the new discovered high puckered orthorhombic 2D GaP/InP sheets by lowing the geometric symmetry, and the total energy is lowered.

Table 2. Optimized structural properties, cohesive energies, and DFT/HSE06 bandgaps of GaP allotropes.

GaP allotropes	High puckered orthorhombic monolayer	Low buckled honeycomb monolayer	Zinc Blende bulk
Structure			
Lattice constants (Å)	3.84 (a), 5.91 (b)	3.92	5.53 (5.45)
Bond lengths (Å)	2.32 (b_1), 2.33 (b_2)	2.29	2.39 (2.36)
Bond angles (degree)	110.2^0 (α_1), 99.3^0 (α_2), 124.6^0 (α_3)	117.6^0	109.0^0
Buckling parameters (Å)	0.86 (Δz_1), 1.28 (Δz_2)	0.36	-

Cohesive energies (eV/pair)	-7.79	-7.65	-8.54 (-7.54)
Band gaps (eV)	1.97/2.89	1.54/2.51	1.52/2.37 (2.26)

Table 3. Optimized structural properties, cohesive energies, and DFT/HSE06 bandgaps of InP allotropes.

InP allotropes	High puckered orthorhombic monolayer	Low buckled honeycomb monolayer	Zinc Blende bulk
Structure			
Lattice constants (Å)	4.13 (a), 6.33 (b)	4.249	6.02 (5.88)
Bond lengths (Å)	2.53 (b_1), 2.54 (b_2)	2.51	2.61 (2.55)
Bond angles (degree)	108.6^0 (α_1), 97.5^0 (α_2), 125.5^0 (α_3)	115.6^0	109.0^0
Buckling parameters (Å)	0.98 (Δz_1), 1.48 (Δz_2)	0.54	-
Cohesive energies (eV/pair)	-7.06	-6.89	-7.78 (-6.88)
Band gaps (eV)	1.72/2.59	1.26/1.86	0.38/1.10 (1.34)

3.4 Phonon dispersion

The dynamic stability of the high puckered orthorhombic 2D GaP and InP monolayers was examined from the analysis of the lattice vibrational modes using the combination of the phonon Boltzmann transport equation and the first-principles phonon calculations, as implemented in PHONOPY [117] code, which can directly use the force constants calculated by density functional perturbation theory. Here, a 4×4×1 (64 atoms) large supercell was used and the Brillouin zone is chosen as a Monkhorst-Pack grid of 12×16×1. Analogous to phosphorene [135], there are three acoustical and nine optical modes in these

high buckled orthorhombic 2D GaP/InP monolayers. The atomic motions of lattice vibrational modes are illustrated in Figure 3.4, in which the upper panel illustrates B_{2g}, B_{1g}, B_{3g}^1, A_u, B_{2u} modes viewed from the top, and the bottom panel illustrates A_g^1, A_g^2, B_{1u}, B_{3g}^2 modes viewed from the side. The black-dashed boxes in the upper panel represent the primitive unit cell. Among the vibration modes, A_g^1, A_g^2, B_{1g}, B_{2g}, B_{3g}^1, and B_{3g}^2 are Raman active modes based on the momentum conservation and the group theory.
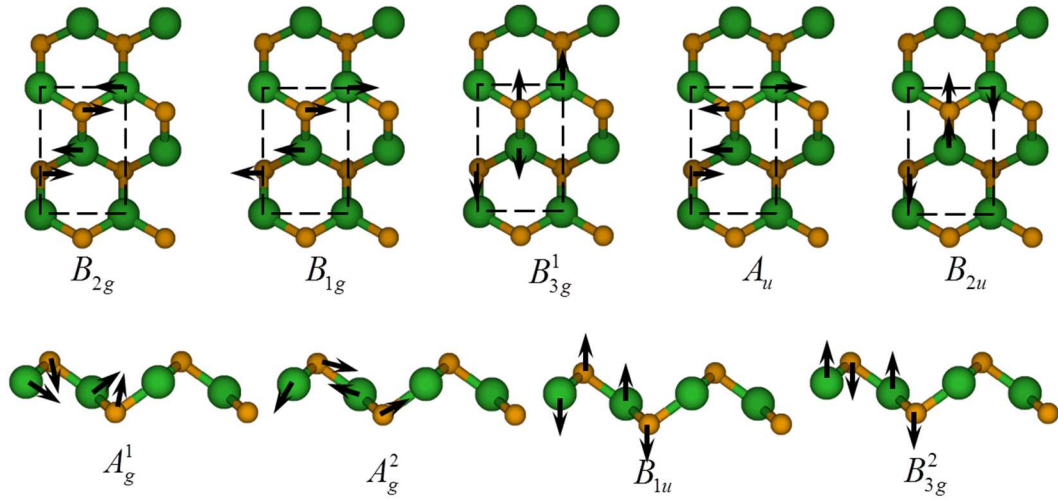
Figure 3.4 Schematic illustrations of the atomic motions of lattice vibrational modes of 2D high puckered orthorhombic GaP/InP monolayers.

Corresponding phonon dispersion spectra are presented in Figure 3.5 (a) and (b), respectively. The Brillouin zone and special K-points are inserted. The three acoustical modes are represented by the black curves, and the different color represents different vibration modes. Both spectra have similar profile: (1) no imaginary frequencies in Brillouin zone, confirming that these high puckered orthorhombic 2D GaP/InP monolayers are energetically located at local minima on the Born-Oppenheimer surface and dynamically stable; (2) different from the phonon dispersion of acoustical modes in the

low buckled honeycomb GaP/InP monolayers[12], the three acoustical modes in the high puckered orthorhombic GaP/InP monolayers are linear as the *k*-point closing to the Γ point, (3) the infrared-activeB_{1u} (red color in Figure 3.5) modes overlaps with the third acoustical mode in the BZ along Y-S and S-X, and merges to B_{1g}(light green in Figure 3.5) at Γ point; on the other hand, B_{1g}, B_{3g}^1(blue in Figure 3.5) modes merge each other between Y-S-X and begin to separate from Y and X points towards to the high symmetry Γ point; (4) the remaining high frequency modes are double-degenerate almost in the whole BZ, such as A_u(cyan in Figure 3.5) and B_{2g} (light purple in Figure 3.5), A_g^2 (pink in Figure 3.5) and B_{2u} (dark green in Figure 3.5), while A_g^1 (dark purple in Figure 3.5) and B_{3g}^2(origin in Figure 3.5) are partially degenerated. Such degeneracies are lifted at Γ point; (5) like the profile of the phonon dispersion in phosphorene[135]; the speeds of sound along the Γ-Y direction are higher than those along the Γ-X direction, reflecting anisotropy in their elastic constants. Because of the heavier masses of Ga/In elements, the frequencies of the new allotropes of 2D GaP/InP monolayers are slightly lower than those of phosphorene monolayer [135] (*e.g.*, ~240 cm^{-1} versus 365 cm^{-1} in A_g^1 mode, and ~360 cm^{-1} versus 420 cm^{-1} near the $A_g^2$and B_{2g}modes, respectively).
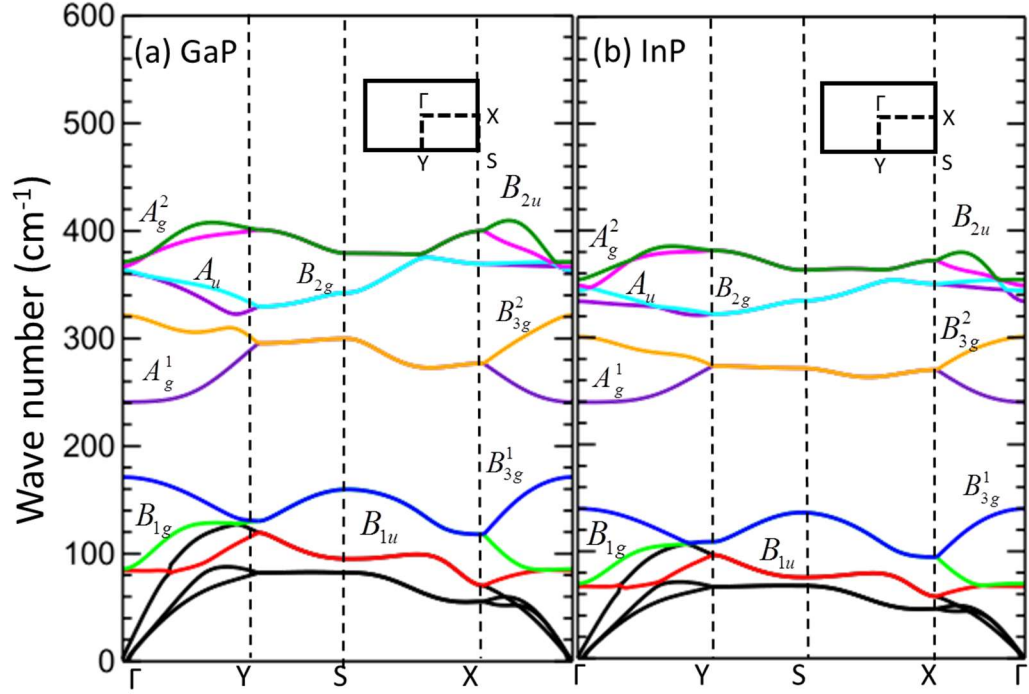
Figure 3.5 Calculated phonon dispersion spectra of the high puckered orthorhombic 2D GaP (a) and InP (b) monolayers.

3.5   Anisotropic electronic properties

The anisotropic electronic properties of the high puckered orthorhombic 2D GaP/InP monolayers were systematically studied from electronic band structures and density of states (DOS) calculations, as presented in Figure 3.6 (a) and (b). The Brillouin zones are inserted in Figure 3.6, the blue arrows in the band structures indicate directions from the tops of the valence bands to the bottoms of the conduction bands, and the blue dash lines in the DOS (right panels in (a) and (b)) denote the Fermi levels. Apparently, the band structures demonstrate semiconductor behaviors, where the high puckered orthorhombic 2D GaP monolayer has an indirect bandgap of 1.97 eV (or 2.89 eV in HSE06) between Γ and Y points (figure 3.6 (a)), and the high puckered orthorhombic 2D InP monolayer shows

a direct band gap of 1.72 eV (or 2.59 eV in HSE06) at Γ point (figure 3.6 (b)), maintaining the direct bandgap nature of its bulk counterpart. The dispersions of charge carriers near the Γ point also show anisotropic behavior, with higher speed towards to Y point and less speed towards to X point. Furthermore, it is found that calculated fundamental bandgaps are ~ 0.43/0.46 eV (or ~0.38/0.73 eV in HSE06) wider than those of the low buckled honeycomb GaP/InP monolayers and even ~ 0.45/1.34 eV (or ~ 0.52/1.49 eV in HSE06) wider than those of their bulk counterparts (see the 7th rows in Tables 2 and 3). These results indicate that the bandgaps in GaP/InP systems could be widened by reducing the dimension of the crystalline structures from 3D zinc blende structures to 2D high puckered orthorhombic structures.
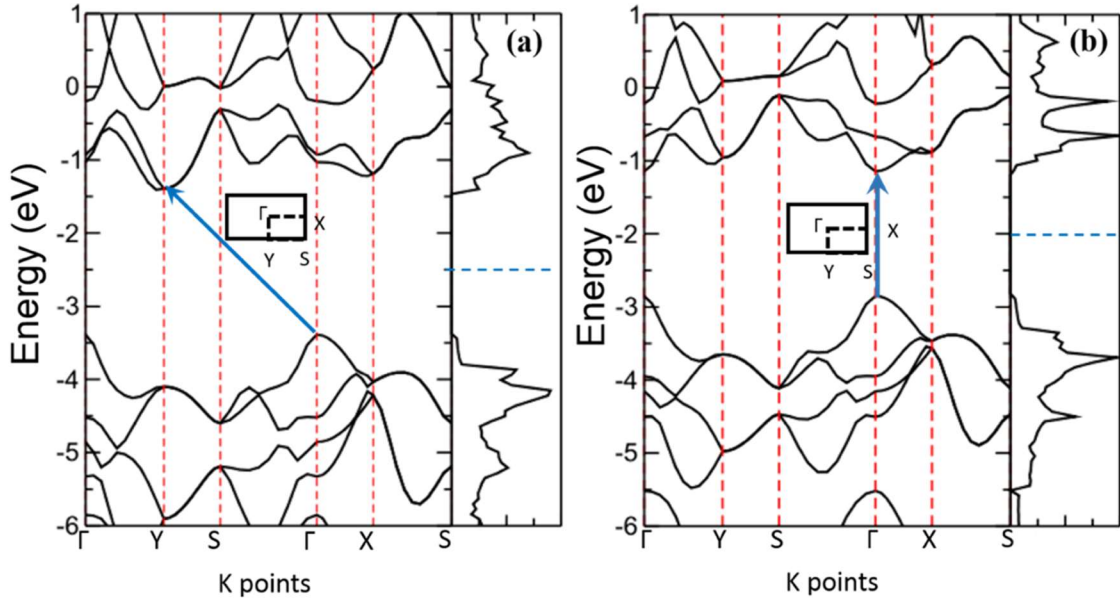
Figure 3.6 Band structures and DOSs of the high puckered orthorhombic GaP (a) and InP (b) monolayers.

The most interesting finding is that the fundamental bandgaps of the high puckered orthorhombic 2D GaP and InP monolayers can be tuned by introducing different types of

strain. Figure 3.7 (a) and (b) presented their fundamental bandgaps (E_g) as a function of the in-plane strain σ (in percentage). The corrected bandgaps calculated by HSE06 hybrid functions are also shown in Figure 3.7, where green open/solid squares denote the DFT/HSE06 bandgaps under the strain along the armchair direction, red open/solid diamonds denote the DFT/HSE06 bandgaps under the strains along the zigzag direction, and black open/solid triangles denote the DFT/HSE06 gaps under the biaxial strains, respectively. The red dotted-dash lines represent the direct/indirect transitions under the strain along the zigzag direction and black dash lines represent such transitions under the biaxial strains.
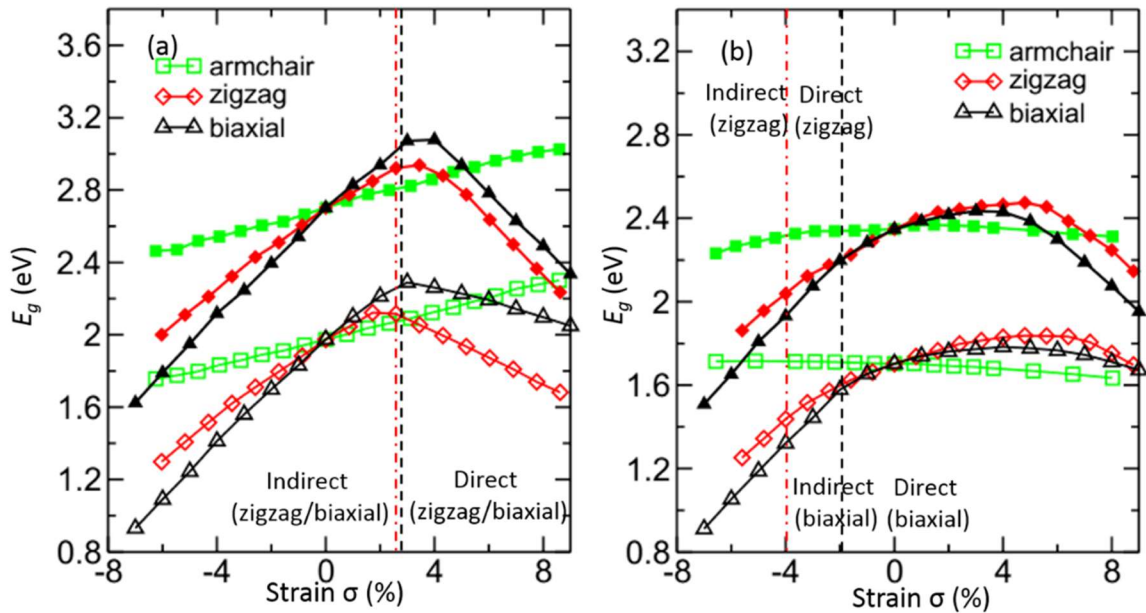
Figure 3.7 Calculated bandgaps (E_g) of the high puckered orthorhombic 2D GaP (a) and InP (b) monolayers as a function of the in-plane strains σ (in percentage).

The band structures of GaP sheet under different strains along the armchair direction are shown in Figure 3.8; the band structures of InP sheet under different strains along the

armchair direction are shown in Figure 3.9. In the case of GaP sheet, even though the bandgap increases linearly with the increase of the strain along the armchair direction (as shown in Figure 3.7 (a)), but the profiles of band structures have almost no change under different strain along the armchair direction (Figure 3.8). The indirect bandgap properties of GaP can be obtained when the in-plane strain σ along the armchair direction ranges from -6% to 9%. In Figure 3.7 (b), while stress or strength InP sheet along the armchair direction, the band gap almost keeps unchanged in the case of InP sheet. The profiles of band structures shown in Figure 3.9 also have almost no change under different strain along the armchair direction. The direct band gap properties of InP can be obtained when the in-plane strain σ along the armchair direction ranges from -7% to 8%.
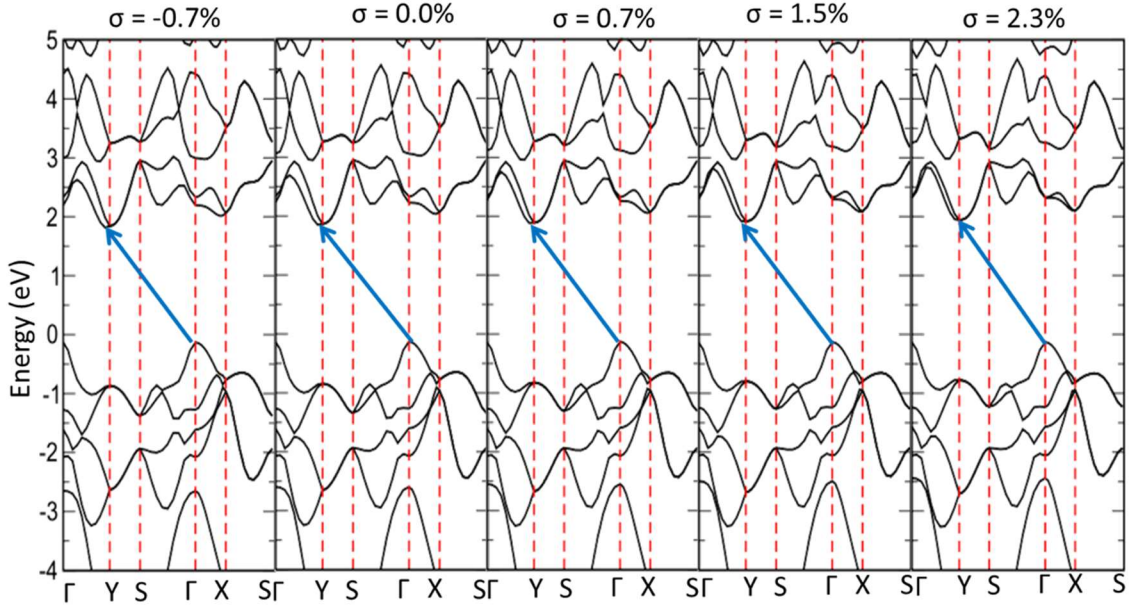
Figure 3.8 The band structures of the high puckered orthorhombic GaP monolayer under the strain σ (in %) along the armchair direction.
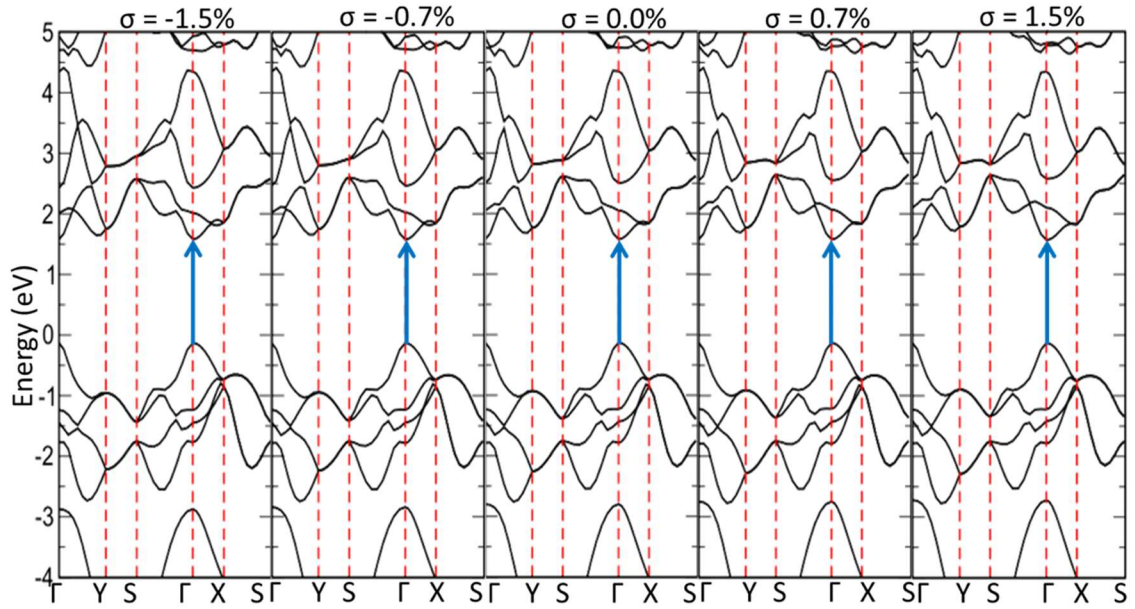
Figure 3.9 The band structures of the high puckered orthorhombic InP monolayer under the strain σ (in %) along the armchair direction.

While, as indicated red dashed lines in Figure 3.7 (a), a transition between indirect and direct bandgaps was found in GaP sheet when the stress was added along the zigzag direction. The DFT bandgap increases from the 1.25 eV (1.60 eV by HSE06) to 2.11 eV (2.84 eV by HSE06) at the transition points and then gradually decreases after the transition points. The band structures of GaP sheet under strains along the zigzag direction are illuminated Figure 3.10. The indirect bandgap nature of the high puckered orthorhombic 2D GaP, which is from the Γ to the Y points as shown in the first three band structures in Figure 3.10, can be tuned to the direct bandgap (at the Γ point as shown in the last two band structures in Figure 3.10) when the in-plane strain along the zigzag direction is over 2.6%.
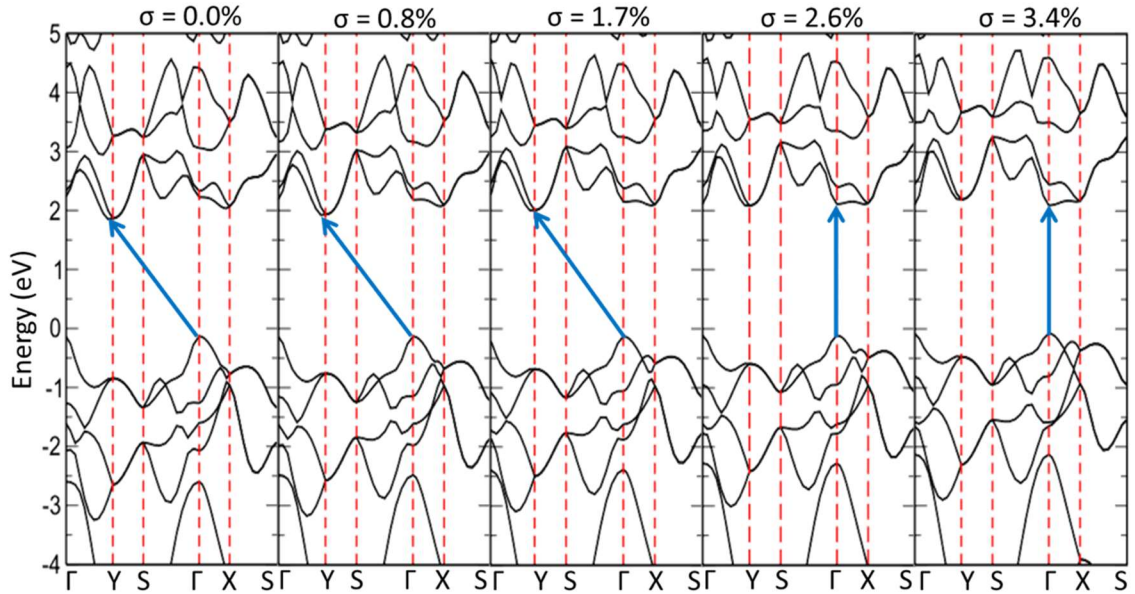
Figure 3.10 The band structures of the high puckered orthorhombic GaP monolayer under the strain σ (in %) along the zigzag direction.

Similarly, when the stress was added along the zigzag direction, a transition between indirect and direct bandgaps of InP sheet was also indicated by red dashed lines in Figure 3.7 (b). However, the transition of bandgap can only occur when the strain is negative, *i.e.*, -4% along the zigzag direction. The bandgap decreases as the decrease of the negative strain but increases as the increase of the positive strain, reaching a maximum at a strain of ~ 4%. Even the bandgap slightly decreases after 4% of strain but it still keeps as large as 1.72 eV (~ 2.0 eV in HSE06) at large strains of 8%. Figure 3.11 demonstrated the band structures of InP sheet with different strain along the zigzag direction, the direct Γ- Γ gap as shown in the last two band structures in Figure 3.11, was tuned to Γ- Y indirect gap as shown in the first three band structures in Figure 3.11 when the strain is under -4.0%.
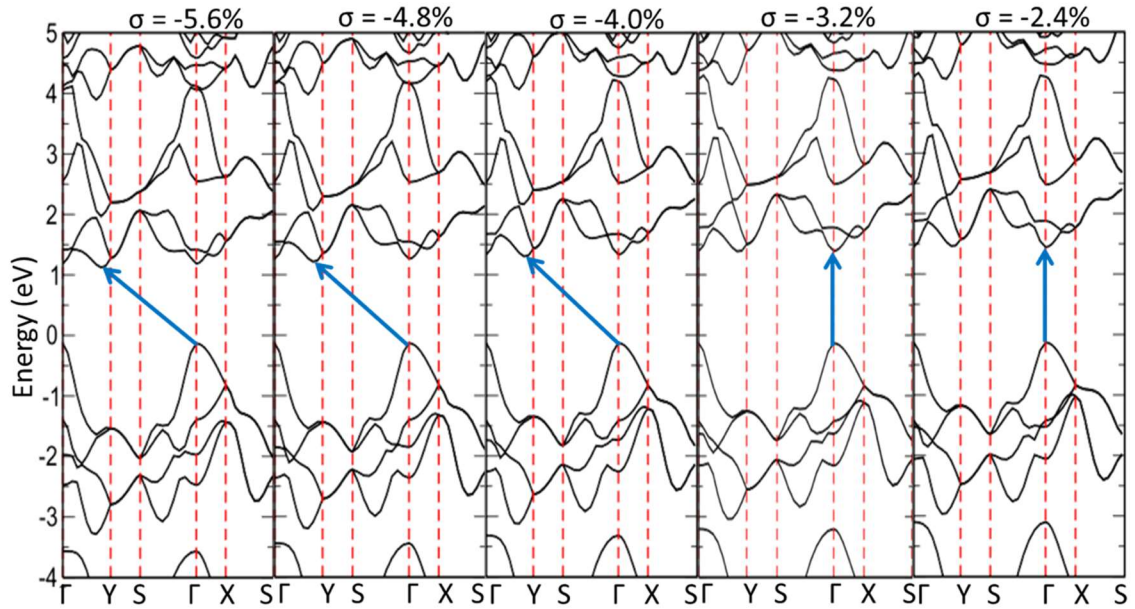
Figure 3.11 The band structures of the high puckered orthorhombic InP monolayer under the strain σ (in %) along the zigzag direction.

As indicated by black dashed lines in Figure 3.7, the indirect bandgap nature of both GaP and InP sheet can be tuned to the direct bandgap when the strain is along the biaxial direction. The transition happens when the in-plane strain of GaP is over 3% or in-plane strain of InP is under -2.0%. The corresponding band structures of GaP sheet and InP sheet are shown in Figure 3.12 and 3.13.
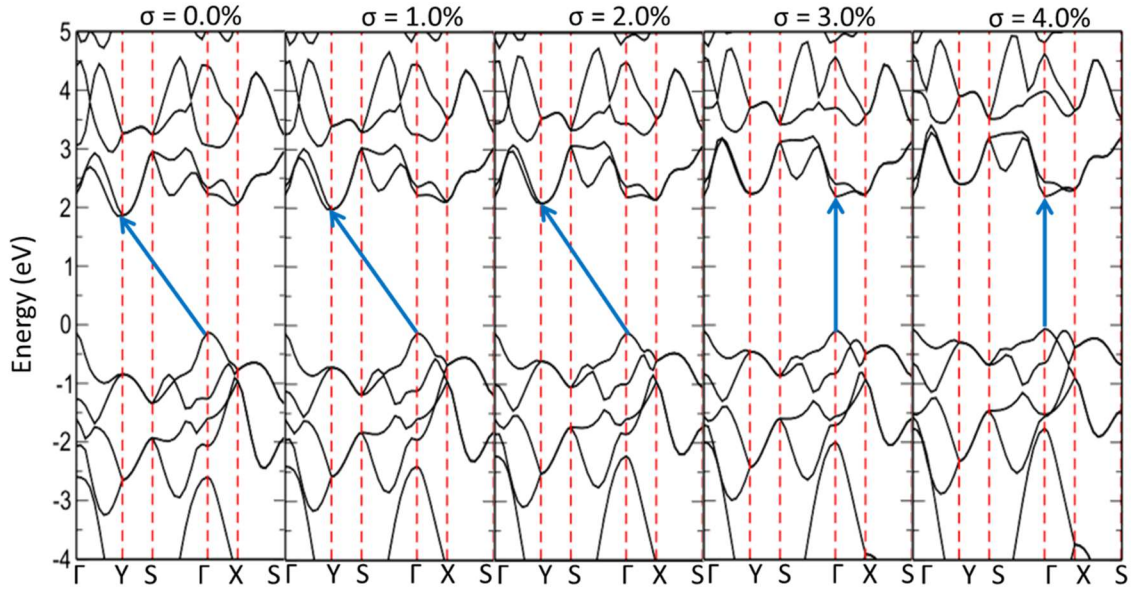
Figure 3.12 The band structures of the high puckered orthorhombic GaP monolayer under the strain σ (in %) along the biaxial direction.
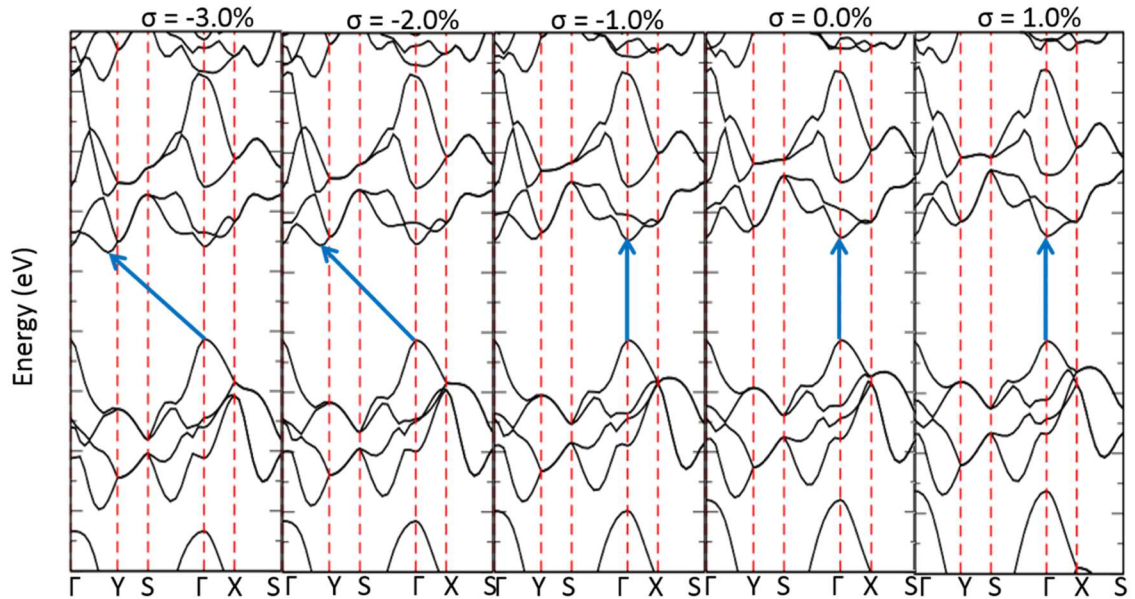
Figure 3.13 The band structures of the high puckered orthorhombic InP monolayer under the strain σ (in %) along the biaxial direction.

These results clearly demonstrate that the high puckered orthorhombic GaP monolayer can be easily tuned to direct bandgap under a small elastic expansion (by ~3%). The high puckered orthorhombic InP monolayer, on the other hand, can maintain its direct bandgap nature even in a large non-elastic expansion (by ~8%), providing a very important fundamental guidance for functionally designing desired 2D nanoelectronic, optoelectronic, and photovoltaic devices through strain-induced bandgap engineering.

3.6   Anisotropic mechanical properties

The unique anisotropic structures of the high puckered orthorhombic GaP/InP monolayer binary compounds lead to the anisotropic behaviors in their mechanical properties. Figures 3.14 - 3.17 show the strain energy density function Ψ as a function of the strain ε along different directions. Figure 3.14 and Figure 3.15 demonstrate the armchair and the zigzag expansion of GaP layer; while Figure 3.16 and Figure 3.17 demonstrate the armchair and the zigzag expansion of InP layer. Inserted structures in Figure 3.14 - 3.17 are the top and side views under different strains (marked with purple circles). The black dashed lines indicate the criteria of the strains after that the structures either broken or change to another type of lattice. The blue dash lines in each Figure are the fitted curves of the strain energy density function.

The inserted structures in each figure illustrate that the high puckered orthorhombic GaP and InP monolayers underwent an elastic expansion, a structural deformation, and then a structural broken process as the strain increases. Such processes strongly depend on the direction of the strain. The deformation will occur when the strain is over 0.2 for the armchair expansion (top and side views of structures at the left side of the black dashed lines in Figure 3.14 and Figure 3.16). However, it will easily occur if the expansion along

the zigzag is over 0.12 (top and side views of structures at the left side of the black dashed lines in Figure 3.15 and Figure 3.17). For large strain ($\varepsilon > 0.3$), the armchair expansion will lead to bond broken along the armchair direction and the structures are destroyed to formed zigzag chains at large strain (top and side views of structures at the right side of the black dashed lines in Figure 3.14 and Figure 3.16). The zigzag expansion, on the other hand, will lead to a lattice change from a hexagonal ring to a rectangular ring when the strain is larger than 0.18 (top and side views of structures at the right side of the black dashed lines in Figure 3.15 and Figure 3.17).
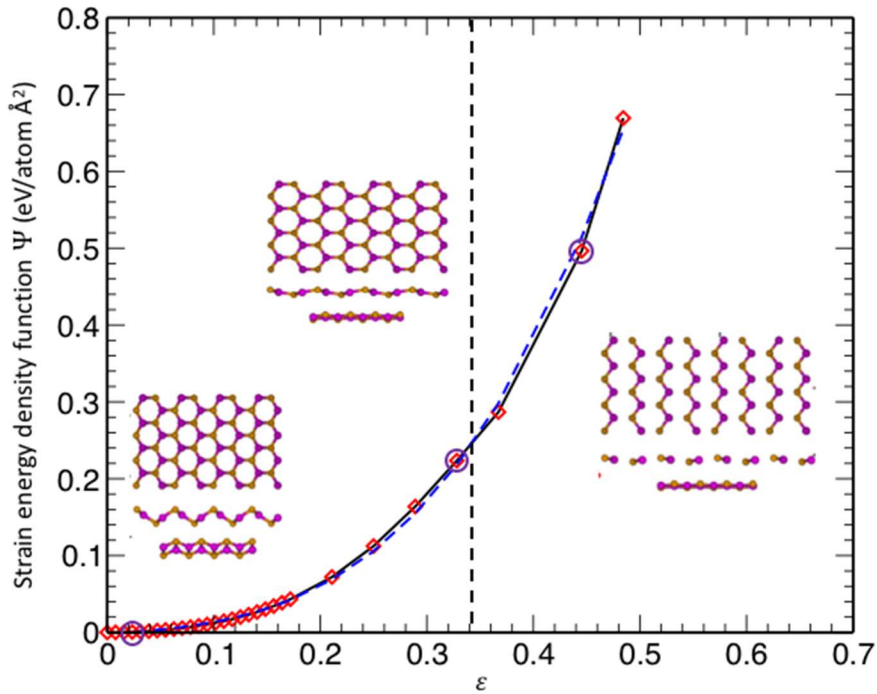
Figure 3.14 The strain energy density function Ψ as a function of the strain ε for the high puckered orthorhombic GaP along the armchair direction.
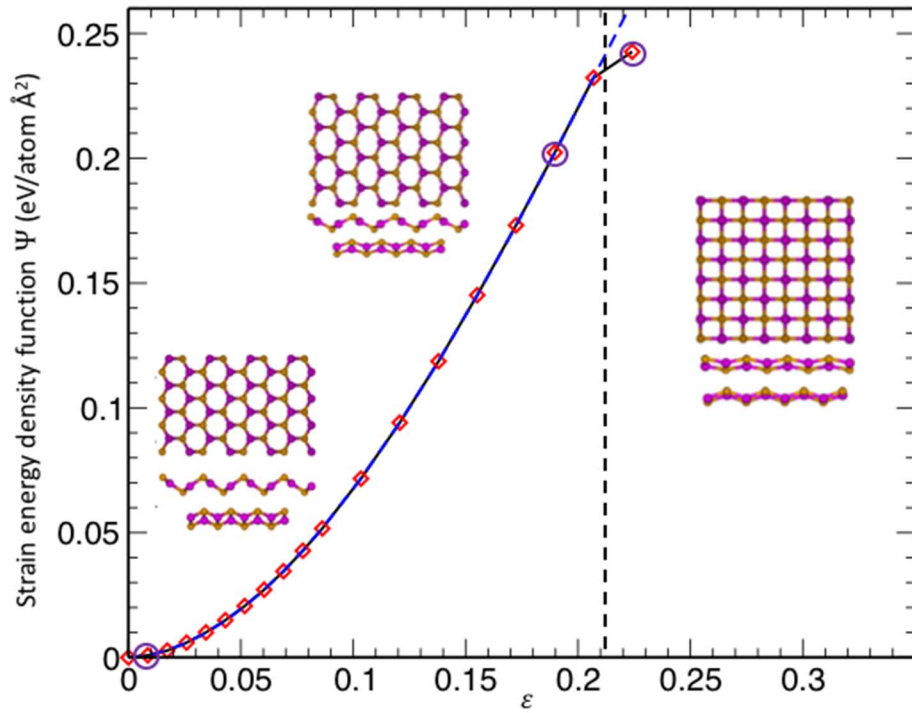
Figure 3.15 The strain energy density function Ψ as a function of the strain ε for the high

puckered orthorhombic GaP along the zigzag direction.
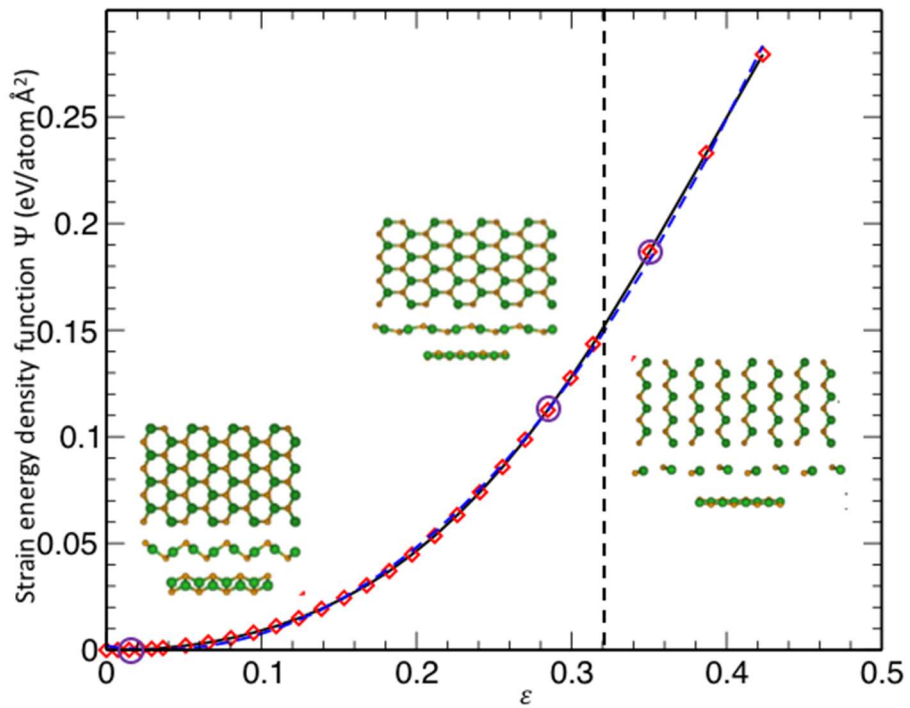
Figure 3.16 The strain energy density function Ψ as a function of the strain ε for the high

puckered orthorhombic InP along the armchair direction.
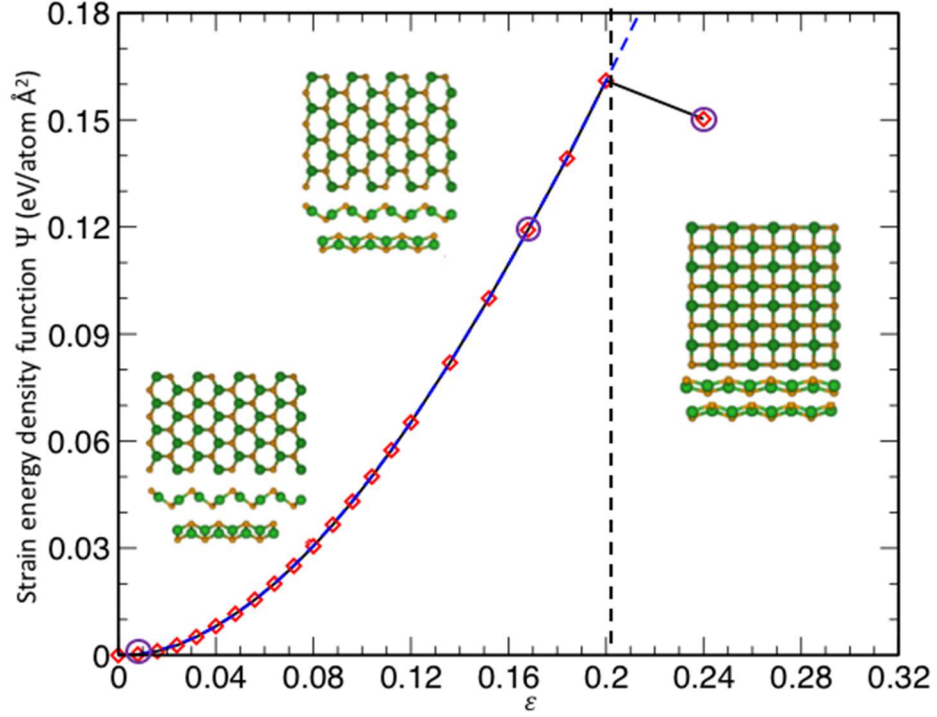
Figure 3.17 The strain energy density function Ψ as a function of the strain ε for the high

puckered orthorhombic InP along the zigzag direction.

As mentioned in chapter 01, the directional dependence of the 2D membrane (tensile)

stress along armchair/zigzag direction S_{11} (analogous to the second Piola-Kirchhoff Stress

in 3D [122]) was calculated from the derivative of the strain energy density function Ψ with

respect to the strain ε. It can be furtherly expressed by Taylor series in terms of a uniaxial

stretch in the given direction E_{11} is one of the Green-Lagrange strain tensor elements [122]

describing the physical and geometrical nonlinearity feature or large deformation). Namely,

$S_{11} \approx Y^{2D}E_{11} + D^{2D}E_{11}^2 + F^{2D}E_{11}^3$, where Y^{2D}, D^{2D}, and F^{2D} are the linear elastic constants

(*i.e.*, Young's modulus) and the high order effective nonlinear elastic moduli for 2D systems, respectively.

The corresponding stress S_{11} as the functions of stretch E_{11} along the armchair and the zigzag direction of GaP layer are plotted in Figure 3.18, and those of InP layer is plotted in Figure 3.19, respectively. The red dash lines indicate the first order terms, the green dash lines indicate the second order terms and the blue dash lines indicate the third order terms. It was found that the elastic behavior holds in the very small range of the strain (*i.e.*, < 0.05 for the armchair and < 0.025 for the zigzag directions, respectively). The second order nonlinear elastic behavior dominates in a large range of the strain (*i.e.*, $0.05 < \varepsilon < 0.18$ for the armchair direction and $0.025 < \varepsilon < 0.1$ for the zigzag direction). Estimated Young's moduli and high order effective nonlinear elastic moduli are listed in Table 4. They all show a strong directional dependent nature. Especially, those constants along the zigzag direction are about one order in magnitude stronger than those along the armchair direction, indicating the strong unique anisotropic mechanical behavior in the high puckered orthorhombic GaP and InP monolayers. Compared to graphene (*e.g.*, the experimental value of graphene [123] is 340 Nm^{-1} for Y^{2D}), they seem softer, even along the zigzag direction. The poison ratios, on the other hand, were found to be close to zero in the linear elastic range (*i.e.*, $\varepsilon < 0.025$), almost independent of the direction of the strain exerted, mainly because of the lifting of high buckling during the strain.
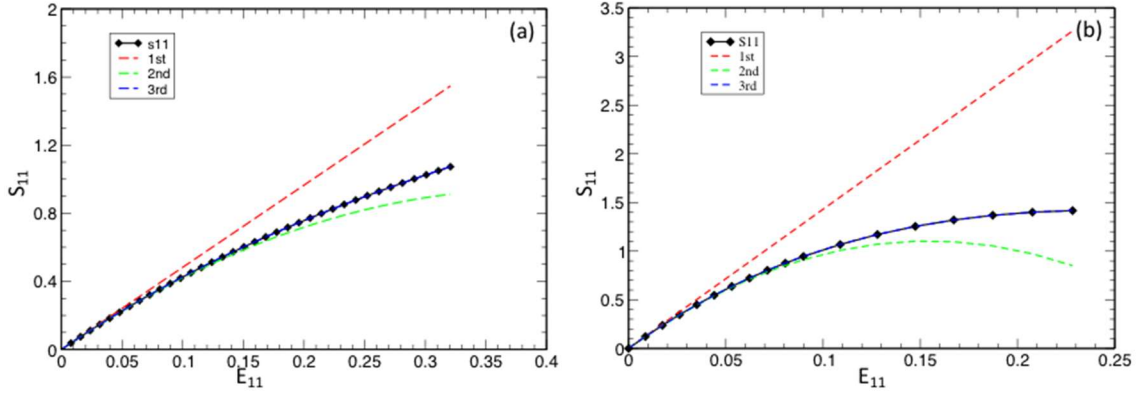
Figure 3.18 Stress S_{11} as the function of stretch E_{11} of GaP along the (a) armchair direction and (b) the zigzag direction.
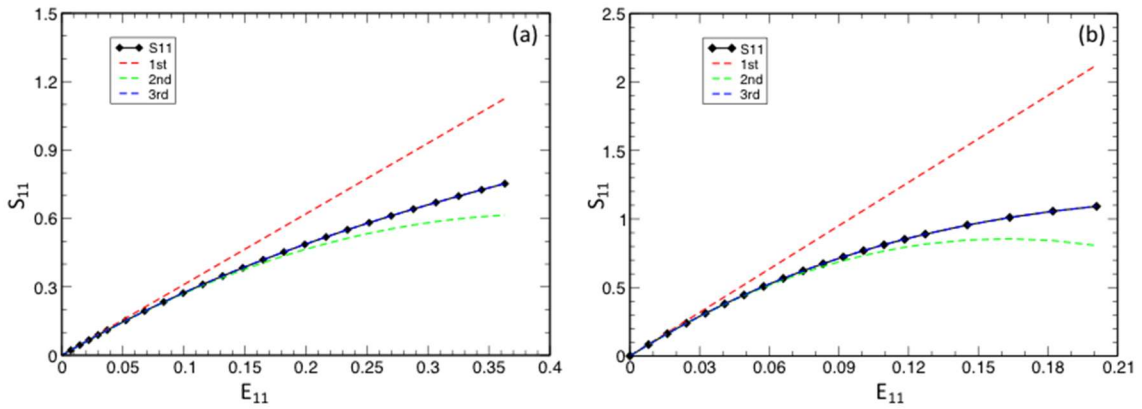
Figure 3.19 Stress S_{11} as the function of stretch E_{11} of InP along the (a) armchair direction and (b) the zigzag direction.

Table 4. Directional dependence of Young's moduli (3rd column) and the effective nonlinear elastic moduli (4th and 5th columns) of the high puckered orthorhombic GaP and InP monolayers.

Binary compounds	direction	Y^{2D} (Nm^{-1})	D^{2D} (Nm^{-1})	F^{2D} (Nm^{-1})
GaP	armchair	71.81	-98.97	78.69
	zigzag	228.82	-741.340	763.39
InP	armchair	49.67	-62.11	46.40

	zigzag	169.21	-522.541	566.84

3.7   Conclusion

The new allotropes of 2D GaP and InP monolayer structures with high puckered orthorhombic symmetry were predicted from the first-principle studies. Their stabilities are rigorously examined through structural optimization and lattice vibration mode calculations. They are energetically more stable than the previously predicted 2D GaP/InP sheets with low buckled honeycomb structures. They possess strong anisotropic and nonlinear mechanical properties. They are both semiconductor materials with the HSE06 functional band gaps of 2.89 eV and 2.59 eV, which are either direct at the Γ point in the case of the InP monolayer, or indirect between Γ and Y points in the case of the GaP monolayer. Most importantly, due to their anisotropic natures, their band gaps can be tuned by introducing strains either along the zigzag and armchair directions or biaxial. Especially, a transition between the indirect and direct band gaps can occur within a small strain range (less than $\pm$ 4%) either along the zigzag direction or under biaxial strain, providing intrigued hints for bandgap engineering.

CHAPTER IV

PROSPECTS OF PHOSPHORENE AS AN ANODE MATERIAL FOR HIGH-

PERFORMANCE LITHIUM ION BATTERY

4.1 INTRODUCTION

4.1.1 Lithium-ion battery

Lithium-ion batteries (LIB) are composed of three parts: anode, cathode, and electrolyte. A rough schematic of a lithium-ion cell is shown in Figure 4.1, in which the anode, commercially composed of graphitic carbon, acts as the negative terminal, and the cathode, typically a lithium metal oxide, acts as the positive terminal of the battery (during discharge). The cathode reacts according to the following half reaction:

$$LiMO_2 \leftrightarrow Li_{1-x}MO_2 + xLi^+ + xe^- \tag{4-1}$$
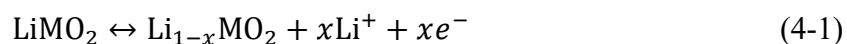
similarly, the anode reacts according to the following half reaction (for graphitic carbon as the anode materials):

$$xLi^+ + xe^- + 6C \leftrightarrow Li_xC_6 \tag{4-2}$$
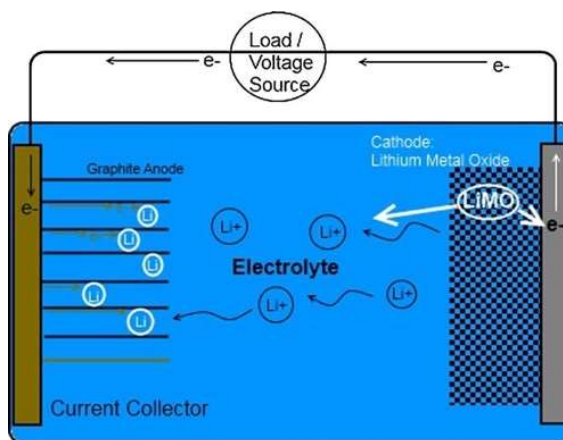
Figure 4.1 Schematic of lithium ion cell

Li$^+$ ions move between the anode and cathode via the electrolyte to finish the charging. When charging, a voltage is applied across the anode and cathode, Lithium ions are formed from the lithium metal oxide in the cathode, diffuse across the electrolyte, and are finally inserted into the anode. When discharging, electrons move from the anode to the cathode, positive current originates from the cathode, and so the cathode acts as the positive terminal.

4.1.2   Current development of the anode material for Li-ion battery

As the anode material for high performance LIB, one should have high Li capacity with high capacity, high rate charging/discharging, large open circuit voltage, and good reversibility in cycling performance. Lots of efforts have made for searching the good quality of anode materials for Li-ion battery. Graphite has conventionally been chosen as the anode in LIB for commercial use because of its high energy stability, low cost, and good cycling performance [136-140]. But its low specific capacity of 372 *mAh/g* (*i.e.*, its lithium richest compound of LiC_6 with one Li atom per 6 carbon atoms under ambient condition [141, 142]) limited its application as a promising anode for high performance LIB. Silicon was found to be a very attractive anode with an extremely high capacity of

4200 mAh/g [143-148]. However, the large volume expansion, due to the formation of the Li$_{22}$Si$_5$ alloy during lithium intercalation, leads to an irreversibility of Li insertion/extraction[149], and therefore its stability in cycling performance is problematic. Intensive studies on nanostructured Si anode materials to enhance the cycling life have been performed [150-152]. Recently, black phosphorus has aroused much interest as promising anode material in LIB because of its weak van der Waals interlayer space and relatively high capacity of 2596 mAh/g [153-158]. Unfortunately, the cycling efficiency is limited due to the large volume expansion ($\sim 300\%$ expansion[154]) when Li atoms insert into the black phosphorus causing the combined system to form the Li$_3$P alloy.

2D materials are considered as a candidate of anode materials of LIB because of their unique properties. Two typical promising 2D anode materials in LIB are graphene [159-177] and TMDs, such as MoS$_2$ [178-187]. The theoretical capacity of graphene was predicted to be 744 mAh/g with the hypothesis that Li atoms could be adsorbed on the double-side of the graphene with the LiC$_3$ configuration, and the separation of Li atoms could still keep about 4.35 Å to avoid Li clustering, as found in the graphite[172-174]. However, the experimental reports showed that at ambient temperature and pressure, Li metal invariably co-exist with the parallel layers of graphene [172], and only the crumpled or curved singe layered graphene nanosheet [174, 175] or carbonaceous such as a group of single layered graphene arranged in 'house card' [173] could accommodate up to two Li atoms per six carbon atoms on both sides of the graphene as well as on the edges. The reversible capacity of such curved graphene was found strongly depending on the nanoporosity of the graphene [172-175]. Similar results were also found in graphene-like MoS$_2$ [187]. Furthermore, it was pointed out that the weak interactions between Li and

graphene (*e.g.*, the binding energy is about 1.04 eV [176]) might result in the low open circuit voltage and weaken the electrochemical performance[140, 159-161, 188] in LIB. Recently, another family of 2D materials[189], such as the 2D Ti_3C_2 materials, was reported as promised host materials for LIB. Calculated theoretical capacity for Li is 447.8*mAh/g*, higher than that of graphite, but the calculated open circuit voltage was low. Searching for anode materials with strong interaction with Li atoms and large open circuit voltage is motivated[189].

Analogous to graphene and MoS_2, phosphorene can be synthesized by mechanical exfoliation of the black phosphorus[41, 66]. This new discovered 2D material has quite unique properties. It exhibits a puckered honeycomb structure and possesses semiconductor behavior with direct band gap and the anisotropic electronic properties. In addition to those properties, the anisotropic mechanical, thermal, and optical properties, as well as the related potential applications have been reported [190-197]. Based on the unique properties, numbers of theoretical calculations about the diffusion and the capacity of phosphorene in Li-ion and Na-ion batteries have been carried out [198-206]. Two theoretical groups found that the diffusion energy barrier of Li in phosphorene is anisotropic [198, 199], and the diffusion mobility of Li atom along the zigzag direction on phosphorene is about 10^{10} times faster than that along the armchair direction. The similar ultrafast diffusion mobility was also reported in Na-ion battery [204, 205]. Noted that these calculations on the diffusion were carried out using the climbing image nudged elastic band method [207, 208] along with some specific orientations, and a comprehensive study on the diffusivity along various possible diffusion paths is desired so as to have an entire picture about the diffusivity on phosphorene surface. The theoretical capacity of Li on the

phosphorene monolayer was predicted to be about 433 *mAh/g* by Zhao *et al*. using DFT calculations[203]. While Kulish *et al*. [205] predicted that the capacity for Na can be as high as 865 *mAh/g* using DFT calculations including the van der Waals interaction[209]. Therefore, a complete understanding of the capacity of Li in phosphorene is indeed necessary, and experimental investigation along this orientation is indispensable.

4.2 Methodology

Our first principles calculations were performed using the DFT framework, as implemented in the VASP. The electron-ion interactions were described by the PAW, while electron exchange-correlation interactions were described by the GGA in the scheme of PBE. The effect of van der Waals interaction on the Li adsorption was also considered by employing the semi-empirical correction scheme of Grimme, implemented in the VASP package (*i.e.,* referred as DFT-D2). An energy cutoff was set to be 500 eV for the plane wave basis in all calculations, and the criteria for the convergence of energy and force in relaxation processes were set to be 10^{-4} eV and 10^{-4} eV/Å, respectively.

For the benchmark, we calculated the structural and electronic properties of phosphorene. The optimized lattice constants for phosphorene are a = 3.306 Å, and b = 4.619 Å, which are consistent with the previous DFT results [66, 199, 203, 204]. The band structure for the optimized phosphorene shows the directed bandgap behaver with the band gap of 0.82 eV, inconsistent with other DFT results[66, 203, 205], but underestimated compared with the experimental results[210]. The underestimate in band gap in the LDA or GGA-PBE types of calculations will not affect the calculations on the Li adsorption, intercalation, and diffusion, as pointed out in the calculations for the Na adsorption. The Brillouin zone is set using a Monkhorst-Pack grid of 16×12×1 in all calculations related to

the 2×2 phosphorene supercell and 5×3×1 in all calculations related to the 5×5 phosphorene supercell.

4.3 Adsorption of single Li on phosphorene monolayer

As shown in Figure 4.2, we employed the 2×2 (top) supercell and 5×5 (bottom) supercell to study the adsorption of Li on phosphorene monolayer, where (see the top structure on Figure 4.2) the larger balls with light purple color denote phosphorus on the ridge; the dark purple color, in the valley. The smaller balls with different color indicate positions of Li atoms. 40 possible Li adsorption sites on the top of phosphorene unit cell were taken into consideration. Li atom was placed either on the top of P atoms (referred as TA sites and are represented by red dots in Figure 4.2), or on the top of the middle of P-P bonds (referred as TB and VB sites and are represented by blue dots in Figure 4.2), or at the center of the triangular region formed by P-P-P atoms (referred as TH and VH sites and are represented by green dots in Figure 4.2), or at other sites spread among these sites (represented by black dots in Figure 4.2). The characters 'V' and 'T' in the notations represent the positions of Li atom in the valley and on the top of the ridge, respectively.
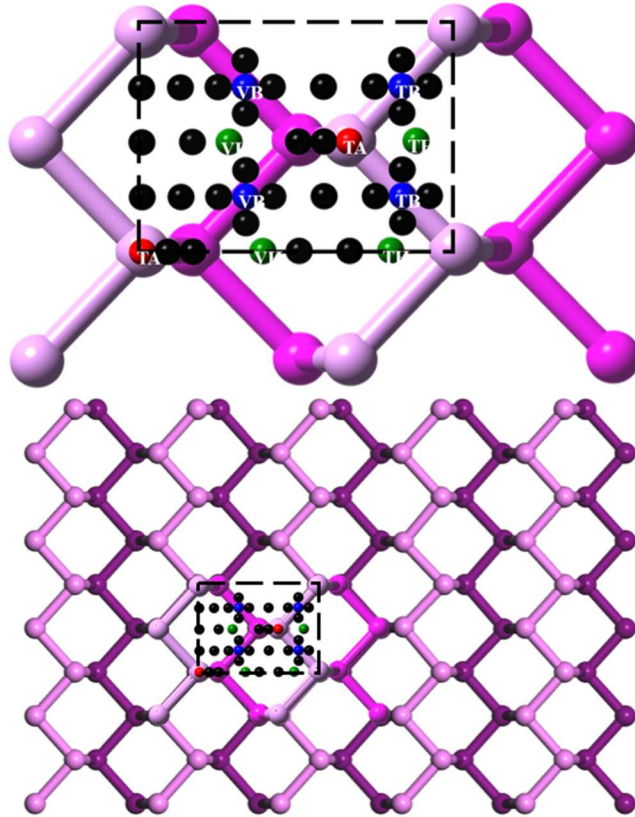
Figure 4.2 Top view of 2×2 (top) and 5×5 (bottom) phosphorene with 40 single Li adsorption sites in the 1x1 unit cell (i.e., the black dashed boxes).

To give a suitable interlayer distance (*b*) of phosphorene, we calculated the total energies of the Li-phosphorene system with different interlayer distance. In the Li-phosphorene system, Li was fixed on the top of the certain site with different vertical distance (*d*), in which *d* is defined from the Li atom (black ball) to the middle of puckered phosphorene indicated by the dot-dash line (as shown in Figure 4.3 (a)). Figure 4.3 (b) and (c) shows the total energies as function of vertical distances with Li atom fixed on the top of two arbitrary sites of the 5×5 phosphorene, the interlayer distance ranges from 8 Å to 20 Å. In Figure 4.3 (b) and (c), the black curves donate total energy as a function of vertical distance *d* with interlayer distance *b* equals to 20 Å; red curves, *b* equals to 15 Å; green

curves, b equals to 13 Å; blue curves, b equals to 11 Å; brown curves, b equals to 10 Å; purple curves, b equals to 9 Å; and cyan curves, b equals to 8 Å, respectively.

When the interlayer distance b equals to 8 Å, the total energy curves and energy minima are obviously different with other curves, which indicate the exist of strong interlayer interactions. When the interlayer distance b ranges from 9 Å to 11 Å, the energy curves look similar but the energies with Li at different vertical positions are still different, which means the interlayer interactions are still strong enough to influence the system. When the interlayer distance b ranges from 13 Å to 20 Å, the energy curves are about the same, which means the layer interactions are very small and can be ignored. Thus, the interlayer distance should be set longer than 13 Å. In this thesis, we set the interlayer distance is 15 Å.
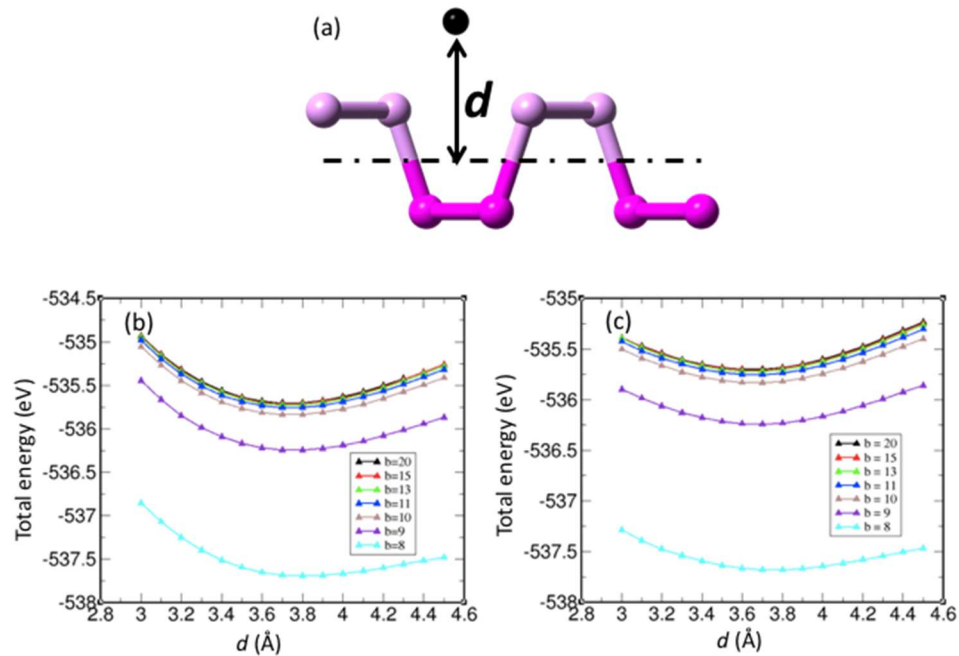
Figure 4.3 (a) The vertical distance (d); (b) and (c) the total energies as a function of vertical distance with different interlayer distance for a Li atom loaded on two different sites.

72

The vertical relaxation was carried out by allowing the motion of Li and P atoms along the direction perpendicular to the phosphorene surface. The 2×2 and 5×5 phosphorene were both used to optimize at each site. By processing the simulation, we found that the preferential vertical distances of Li are the same for each site in both cases. As an example, we found that in the case of a Li atom loaded at the VH site of either 2×2 phosphorene or 5×5 phosphorene, an equilibrium vertical distance was found at 3.75 Å, and the corresponding energy is -5.35 eV/atom on 2×2 and -5.357 eV/atom on 5×5 phosphorene. The small difference in energy shows that the size of phosphorene supercell does not influence the adsorption of Li. Thus, the 2×2 phosphorene was chosen as the supercell for the rest of the simulations.

4.3.1   Adsorption energy landscape

The adsorption energy per Li atom on monolayer phosphorene (E_a) is defined as

$$E_a = (E_{Li_nP_m} - E_{P_m} - nE_{Li}^a)/n \tag{4-3}$$

where $E_{Li_nP_m}$, E_{P_m}, and E_{Li}^a are the total energy of the Li$_n$P$_m$ system, phosphorene (m atoms), and the isolated Li atom, respectively, and n is the number of adsorbed Li atoms in phosphorene. From the energy adsorption defined in Eq. (3), we can calculate the adsorption energy landscape for a single Li atom loaded on phosphorene surface and find the preferential positions for Li adsorbed on phosphorene.

Based on the calculated adsorption energy on each site, the adsorption energy landscape was obtained. As shown in Figure 4.4, the colors in the right column represent the adsorption energy (E_a) at an adsorption site relative to that at the VH site. The darker the color is, the lower the relative adsorption energy. A schematic structure of the 2×2

phosphorene supercell is attached on the landscape to illustrate the Li adsorption positions. Figure 4.4 (b) and (c) zoom in the energy landscape in the white box and blue box in (a), respectively. Figure 4.4 clearly shows that the adsorption energy landscape possesses an anisotropic behavior. Positions of the Li atom with relatively low adsorption energy are located in the valley along the zigzag direction with minimum energy at VH sites, while positions of the Li atom with relatively high energy are located on the top of the ridge along the zigzag direction with the maximum relative energy at TA sites. The adsorption energy difference between these two sites is about 0.78 eV/Li. The saddle points were found at the VB site and the TB site, as indicated by the white and blue boxes in Figure 4.4 (a). Their corresponding adsorption energies are lower than those of neighbors along the bond direction but higher than those of the neighbors along a direction perpendicular to the bond, as shown in detail in Figure 4.4 (b) and (c), respectively. The adsorption energy landscape reveals that Li prefers to stay at the most stable VH site, also possibly stay at the metastable VB and TB sites when the most stable VH sites are occupied. Furthermore, the energy difference along the zigzag direction in the valley is much smaller than that along the armchair direction, which indicates that the preferential diffusion path for a single Li atom will be along the zigzag direction in the valley.
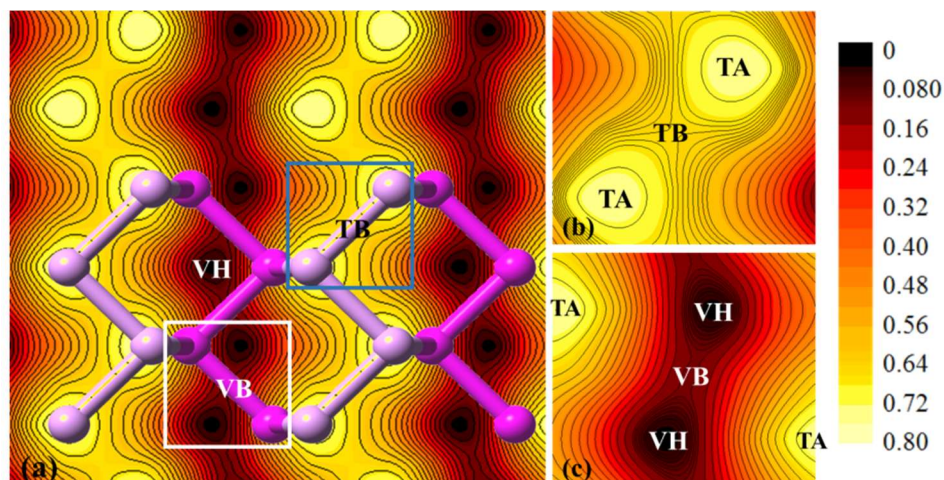
Figure 4.4 (a) Adsorption energy landscape of a Li atom on phosphorene. (b) and (c) zoom in the energy landscape in the white box (around the saddle points at VB site) and blue box (around the saddle points at TB site) in (a), respectively.

4.3.2   Diffusion

Rate charging and discharging in the LIB relates to the mobility of Li ions in the anode/cathode. The faster the Li atom moves, the higher the charging/discharging rate, and therefore the rated capacity in the LIB. To study how fast the Li atom moves/diffuses on the phosphorene, we calculated the diffusion energy barrier E_b along various diffusion paths between the preferential adsorption sites VH, VB, and TB. The energy barrier E_b is defined by the relative adsorption energy at the site along the diffusion pathway with respect to that at the corresponding initial site. Figure 4.5 presented the most four possible diffusion paths: in path 1, the Li atom migrates along the zigzag direction, starting at a VH site, going through VB sites, and then ending to another VH site (referred as VH→VB→VH, see the black dots in Figure 4.5 (a)); in path 2, Li atom migrates along the direction perpendicular to the zigzag direction, starting at a VB site, crossing over the ridge

through the TB site, and then ending to another VB site (referred as VB→TB→VB, see the green dots in Figure 4.5 (a)); in path 3, Li atom migrates along the direction that starts at a VH site, crosses over the ridge through the TB site, and then ends to another VH site (referred as VH→TB→VH, see the blue dots in Figure 4.5 (a)); and in path 4, Li atom migrates along the armchair direction, starting at a VH site, crossing over the ridge through the highest adsorption energy site TA, and then ending to another VH site (referred as VH→TA→VH, see the red dots in Figure 4.5 (a)). The two different side views of these four paths were also shown in Figure 4.5 (b) and (c). As shown in Figure 4.5 (b), Li atom migrates in the same valley along path 1, but it migrates from one valley over the ridge and to another valley along paths 2-4.
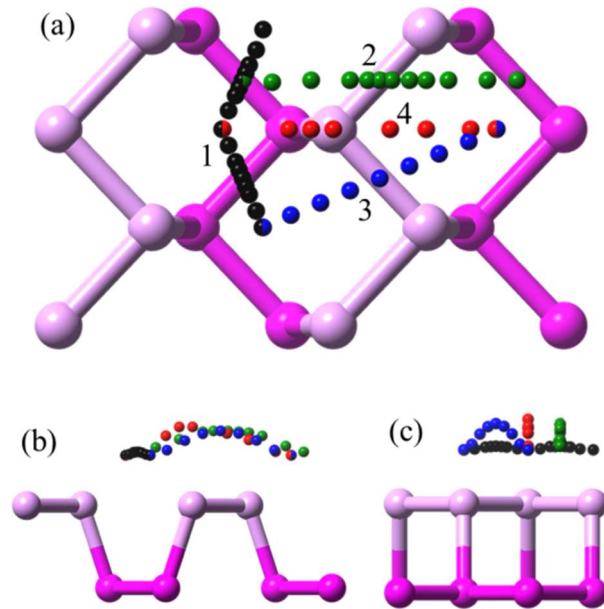
Figure 4.5 (a) Top view of the diffusion pathways on monolayer phosphorene, (b) and (c) side views of the diffusion pathways on monolayer phosphorene.

The corresponding energy barriers (E_b) with respect to the initial position energy for each path as a function of the relative distance are summarized in Figure 4.6 (a). The

relative distance of the Li atom is defined by the ratio of the horizontal distance of Li with respect to the starting point to the horizontal distance of the ending point with respect to the starting point. It was found that the adsorption energy at the VB site is relatively higher than that at other sites along the path 1, and the calculated corresponding diffusion energy barrier to the VH site is 0.10 eV. In path 2, the corresponding diffusion energy barrier is about 0.58 eV, which is about 0.48 eV higher than that in the path 1. It is found that there is a very shallow valley in the diffusion energy barrier around the TB site in path 2, which is attributed to the local minimum along the direction of the P-P bond at the TB site (see Figure 4.4 (b)). Similarly, Li moving along the path 3 also crosses the TB site with the initial point at the VH site, but since the path 3 is along the direction perpendicular to the P-P band at the site TB, there is no local minimum around the TB site. The calculated corresponding diffusion energy barrier in path 3 is about 0.69 eV, which is about 0.11 eV higher than that in the path 2 and about 0.59 eV higher than that in the path 1. In path 4, Li atom migrates from the most preferential adsorption site VH along the armchair direction, and crosses over the most unstable site TA; the calculated diffusion energy barrier is 0.78 eV which is the highest one among these diffusion paths.
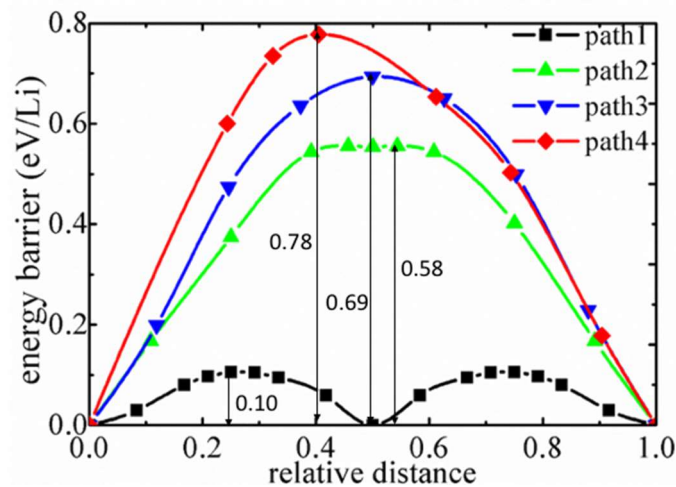
Figure 4.6 The energy barrier as a function of the relative distance along the four paths.

Based on the adsorption energy landscape, the energy barrier along different diffusion paths was determined. Following the Arrhenius equation[211] for the temperature dependence of reaction rates, and currently can be used to model the temperature variation of diffusion coefficients, the diffusion constant (D) of Li can be estimated as

$$D \propto \exp\left(-\frac{E_b}{k_B T}\right) \, ,$$ (4-4)

where E_b is the activation energy (or diffusion barrier), k is the Boltzmann constant, and T is the environmental temperature (300 K was chosen in the calculation). Following Eq. (4), the diffusion constant of Li on phosphorene can be qualitatively evaluated, and the most preferential diffusion path for single Li atoms on phosphorene can be determined. Table 5 gives the diffusion constant of each path and the ratio of the diffusion constant to that of path 1.

Table 5. The diffusion constant of each path and the ratio of the diffusion constant to that of path 1.

Paths	Energy barrier (eV)	Estimated diffusion constant	Compare to path 1
1	0.105	~0.017	1
2	0.556	~4.75×10^{-10}	3.58×10^7
3	0.694	~2.31×10^{-12}	7.36×10^9
4	0.778	~9.00×10^{-14}	1.89×10^{11}

As shown in table 5, the evaluated value along the path 1 is about 3.58×10^7 times faster than that along the path 2, about 7.36×10^9 times faster than that along the path 3, and about 1.89×10^{11} times faster than that along the path 4, respectively, indicating that the Li

diffusion on phosphorene is ultrafast and anisotropic. In addition, the comparison of diffusion constants among these paths reveals that even though paths 2-4 are all cross over the ridge, the mobility of Li is quite different. It is also noted that the diffusion energy barrier of Li on phosphorene (0.10 eV) is much lower than that on graphene (0.327 eV) and MoS_2 (0.25 eV). The evaluated corresponding mobility of Li on phosphorene is then about 4 and 2 orders of magnitude faster than that on graphene and MoS_2, respectively, indicating that the rate charging/discharging is much higher in phosphorene than in graphene and MoS_2. Such high Li diffusivity is important to satisfy the current-density requirements and is essential for the performance of the anode materials in LIB.

The ultrafast and anisotropic diffusion nature for a Li migrates on phosphorene comes from the unique puckered structure of phosphorene, which is crucially important for the Li diffusion. Figure 4.7 shows the optimized vertical distances d as a function of the relative distance along each path. It was found that the maximum vertical difference along the path 1 is 0.09 Å, and such a small height difference allows Li to migrate through the channel very easily. On the other hand, in paths 2-4, a Li atom has to climb from the valley up to the ridge by about 0.58-0.79 Å, hence much more energy is needed for Li to conquer the ridge. A comparison between the diffusion energy barrier (Figure 4.6) and the vertical distance (Figure 4.7) reveals that the lower the vertical distance d, the lower the diffusion energy barrier and the easier for Li to diffuse.
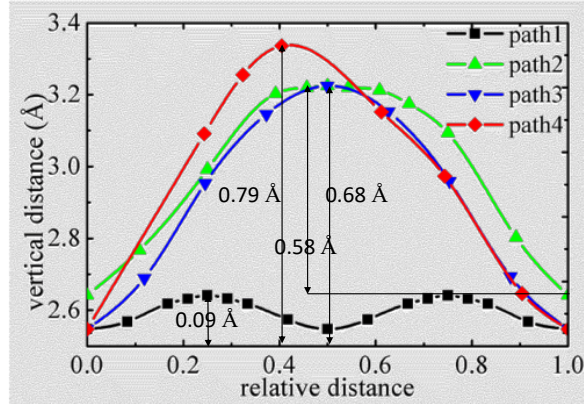
Figure 4.7 The vertical distance d as a function of the relative distance.

4.4 Lithium Intercalation

To study how much phosphorene can accommodate Li atoms and, therefore, to evaluate the capacity of Li on phosphorene monolayer, several Li_nP_{16} systems including LiP_{16}, Li_2P_{16}, Li_4P_{16}, Li_6P_{16}, Li_8P_{16}, and $Li_{16}P_{16}$ were studied. For each Li_nP_{16} system, several configurations including Li atoms loaded on a single side and double sides of phosphorene were taken into consideration. In all configurations, Li atoms are initially placed in VH, VB or TB sites and the corresponding systems were fully relaxed to obtain the stable configurations with different Li concentration. The results are discussed as follows.

4.4.1 LiP_{16} System

The top and side views of the stable LiP_{16} structures with a single Li atom adsorbed at VH, VB, and TB sites are shown in Figure 4.8. The corresponding adsorption energy E_a and the geometric properties are summarized in Table 6. In Figure 4.8, the dark gray ball represents the Li atom, and the balls with light and dark purple colors denote phosphorus atoms on the ridge and in the valley, respectively. The same demonstrations are also shown

80

in the Li_nP_{16} structures in the following figures. The black dash-lines in the top views represent the Li-P distance (d_{Li-P}), and the black arrows in the side views denote the vertical distance (d), respectively. The Li-P distance d_{Li-P} and vertical distance d are shown in the 4th and 5th columns in Table 6. It is obviously seen from the 3rd column in Table 6 that the VH site is the most energetically stable adsorption site with the adsorption energy of -2.086 eV/Li. The next stable adsorption site is the VB site (-1.995 eV/Li), following by the TB site (-1.427 eV/Li).
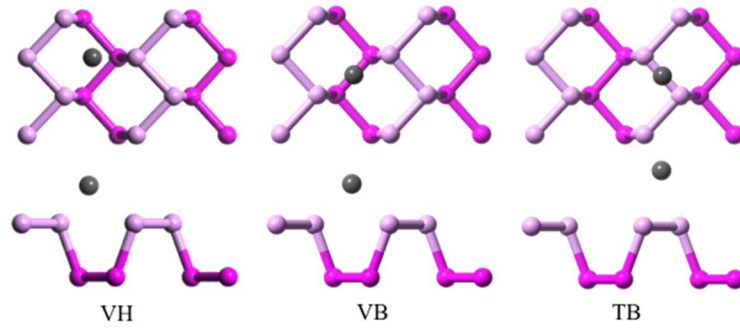
Figure 4.8 Top (up) and side (down) views of the stable LiP_{16} configurations with the Li atom adsorbed at the VH site (left), the VB site (middle), and the TB site (right), respectively.

From the 4th and 5th columns in Table 6, we found that Li atom located at the VH site with a vertical distance (d) of 2.53 Å has three nearest P neighbors; the corresponding Li-P distances (d_{Li-P}) are 2.45, 2.54 and 2.54 Å respectively. Li atom at the VB site has two nearest P neighbors with Li-P distance (d_{Li-P}) of 2.41 Å, and the vertical distance (d) is about 0.07 Å higher than that at the VH site. While at the TB site, the vertical distance (d) is about 0.7 Å higher than that at the VH site, and the two nearest Li-P distances (d_{Li-P}) are equal with the value of 2.58 Å. Since the Li-P distances in these configurations are within the Li-P bond length of 2.68 Å, it indicates that Li atom is chemically bonded with P atoms.

Such chemical bonding nature and low adsorption energy demonstrate that the interaction between Li and phosphorene is strong, compared to the graphene, and therefore could prevent Li clustering during Li insertion, which is desired in the electrochemical performance.

Table 6. Calculated adsorption energy (E_a), the distances between Li and the nearest neighbor P atoms on phosphorene (d_{Li-P}), and the vertical distance (d) of LiP$_{16}$ system with Li atom at the preferential adsorption positions (VH, VB, and TB sites).

system	Configuration	E_a (eV/Li)	d_{Li-P} (Å)	d (Å)
LiP$_{16}$	VH	-2.086	2.45, 2.54	2.53
	VB	-1.995	2.41	2.61
	TB	-1.427	2.58	3.23

4.4.2   Li$_2$P$_{16}$ System

We considered about 45 initial configurations for 2 Li atoms loaded on the single-side of phosphorene. These single-side configurations can be classified by 6 groups denoted as S-VH-VH, S-VH-VB, S-VH-TB, S-VB-VB, S-TB-TB, and S-VB-TB, respectively, where the first notation 'S' means the single-side adsorption, and the second/third notations indicate the locations of two Li atoms, respectively. We found that only 12 stable structures corresponding to groups of S-VH-VH, S-VH-VB, S-VB-VB, and S-TB-TB were obtained after full relaxation. In particular, initial configurations belong to groups S-VH-TB and S-VB-TB were not stable and transferred to the configurations belong to the group S-VH-VH after the full relaxation, mostly due to the migration of the Li atom at the VB or TB site to the more stable VH site. Figure 4.9 presents the top and side views of the four most

stable single-side configurations corresponding to each of the four groups (*i.e.*, S-VH-VH, S-VH-VB, S-VB-VB, and S-TB-TB, respectively).
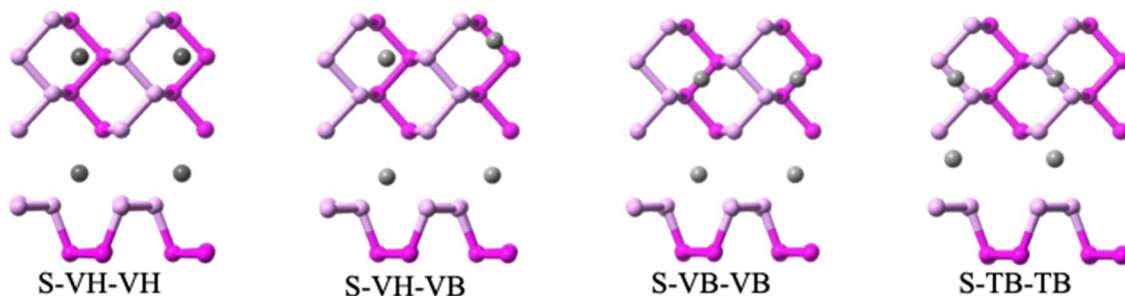
Figure 4.9 Top and side views of the stable Li_2P_{16} system with single-side configurations.

The corresponding adsorption energies and geometric properties for these four configurations are listed in Table 7. In case there are different types of d_{Li-P} and d values for a given configuration, notations corresponding to the sites are indicated in the parentheses in columns 4 and 5 in Table 7. For example, in the configuration D-VH/VB, the d_{Li-P} and d values at VH and VB sites are indicated by VH and VB in the corresponding parentheses. Note that the large Li-Li distances (beyond 6.5 Å) in the double-side configurations in the Li_2P_{16} system are not counted here.

From the adsorption energy E_a (the 3rd column in Table 7), we found that the configuration in the group S-VH-VH is the most stable configuration compared with other single-side configurations. There is no significate change in the vertical distance d at sites VH, VB, and TB, comparing with LiP_{16} system when two Li atoms stay on single-side (see the 5th column in Tables 6 and 7). But some of the Li-P distances (d_{Li-P}) decrease in the Li_2P_{16} system, for instance, from 2.45 Å to 2.35 Å at VH sites, from 2.41 Å to 2.30 Å at VB sites, and from 2.58 Å to 2.45 Å at TB sites, respectively (see the 4th column in Tables 6 and 7). The decrease of Li-P distance d_{Li-P} indicates that the more the Li atoms adsorbed,

the strong the Li-P attractive interactions, and the shorter the Li-P bonds. In addition, since the Li concentration is still low, the nearest Li-Li distance is larger (4.62-4.99 Å, see the 6th column in Table 7) than the Li-Li bond length (2.68 Å in our DFT calculation), indicating that the interaction between Li atoms is very weak.

Table 7. Calculated adsorption energy (E_a), distances between Li and the nearest neighbor P atoms on phosphorene (d_{Li-P}), the vertical distance (d), and the nearest Li-Li distance (d_{Li-Li}) for the stable single-side (up panel) and double-side (bottom panel) configurations of the Li_2P_{16} system.

system	Configuration	E_a (eV/Li)	d_{Li-P} (Å)	d (Å)	d_{Li-Li} (Å)
Li_2P_{16} Single side adsorption	S-VH-VH	-2.045	2.35, 2.56	2.54	4.62
	S-VH-VB	-2.000	2.38, 2.53(VH) 2.32(VB)	2.54(VH) 2.63 (VB)	4.99
	S-VB-VB	-1.957	2.31	2.63	4.62
	S-TB-TB	-1.347	2.45	3.28	4.62
Li_2P_{16} Double side adsorption	D-VH/VH	-2.113	2.43, 2.53	2.51	--
	D-VH/VB	-2.064	2.43, 2.53(VH) 2.41 (TB)	2.50(VH) 2.58 (TB)	--
	D-VB/VB	-2.018	2.41	2.60	--
	D-VH/TB	-1.755	2.34, 2.55 (VH) 2.50 (VB)	2.53(VH) 3.23(VB)	--
	D-VB/TB	-1.718	2.40(up), 2.47(down)	2.59 (up) 3.23 (down)	--

By adding one more Li atom on the other side of the three stable configurations obtained in LiP_{16} system, we constructed double-side configurations for Li_2P_{16} system. It should be noted that, on the other side of phosphorene, the corresponding stable adsorption sites (*i.e.*, the VH, VB or TB site) are those located below TH, TB, and VB sites, if we see them from the top view of phosphorene. 48 initial double-side configurations were constructed following this consideration. They are classified into 6 groups, denoted as D-

VH/VH, D-VH/VB, D-VH/TB, D-VB/VB, D-VB/TB, and D-TB/TB, respectively. The notation 'D' indicates the double-side adsorption; the notation before/after the slant indicates the Li atoms at the sites above/below phosphorene monolayer. After fully relax, only 15 stable double-side configurations corresponding to the first five groups were obtained, and the five most stable double-side configurations among them corresponding to each of the five groups are shown in Figure 4.10. The corresponding adsorption energies and geometric properties are listed in Table 7.

D-VH/VH   D-VH/VB   D-VB/VB

D-VH/TB   D-VB/TB
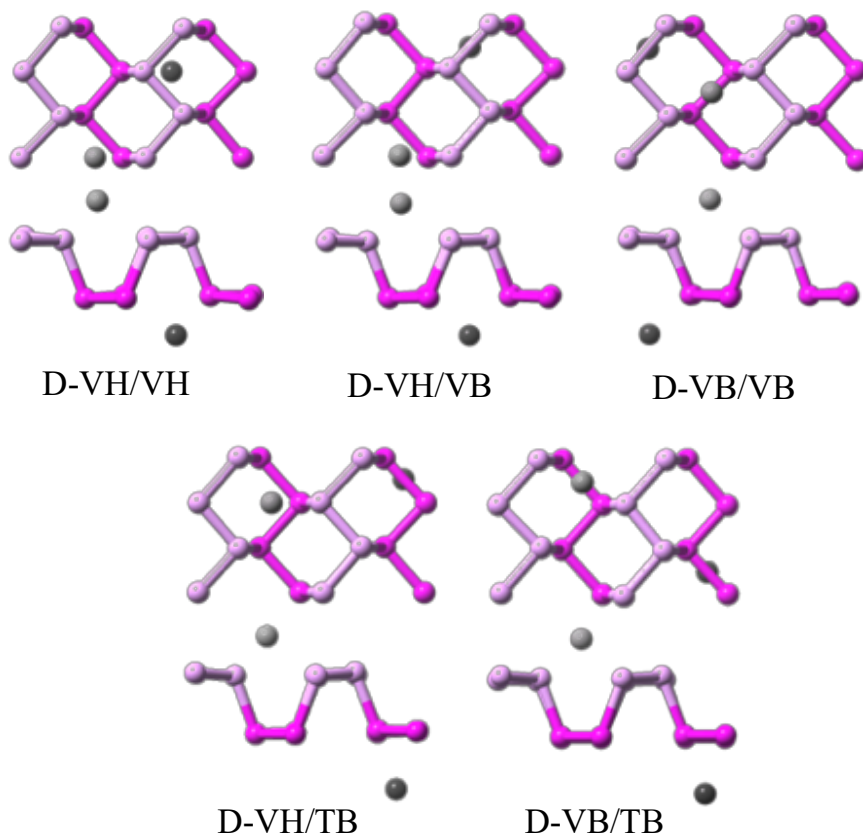
Figure 4.10 Top and side views of the stable Li_2P_{16} system with double-side configurations.

Comparing the adsorption energies E_a among those stable single/double-side configurations (see the 3rd column in Table 7) we found that the configuration D-VH/VH (-2.113 eV/Li) is the most stable structure in the Li_2P_{16} system, followed by configuration

D-VH/VB (-2.064 eV/Li), and then the single-side configuration S-VH-VH which is about 0.02 eV higher than the configuration D-VH/VB. It was also found that, by adding one more Li on the other side of the stable LiP_{16} system, the nearest Li-P distance (d_{Li-P}) (the 4th column in Table 7) and the vertical distance d (the 5th column in Table 7) at sites VH, VB, and TB are similar to those in the stable LiP_{16} system (the 4th and 5th columns in Table 6), since the separation of Li atoms on both sides are still the same as those in the stable LiP_{16} system.

4.4.3 Li$_4$P$_{16}$ System

In searching the stable configurations for Li$_4$P$_{16}$ system with single-side adsorption, we mainly focused on the configurations in which four Li atoms were loaded at each of the four 1x1 unit cells above phosphorene monolayer. The initial single-side configurations were classified into three groups, denoted as S-4VH, S-4VB, and S-4TB, respectively, where the number in the notations indicates the total number of Li atoms on the corresponding sites. These single-side configurations were fully relaxed and only five of them were stabilized to the structures named as S-4VH$_a$, S-4VH$_b$, S-2(VH-TH), S-4VB, and S-4TB, respectively (see Figure 4.11), in which the configurations S-4VH$_a$ and S-4VH$_b$ are distinguished by the distribution of the four Li atoms at the four VH sites on the 2×2 supercell with different symmetry. While, the configuration S-2(VH-TH) was obtained from the initial configuration in the group S-4VH by distributing the four Li atoms at the VH sites with Li-Li distance shorter than the Li-Li bond length. During the relaxation, these Li atoms push each other away, and two of them move to the TH sites, and the system was finally relaxed to a stable structure with S-2(VH-TH) configuration with Li-Li distances of 3.0 Å.
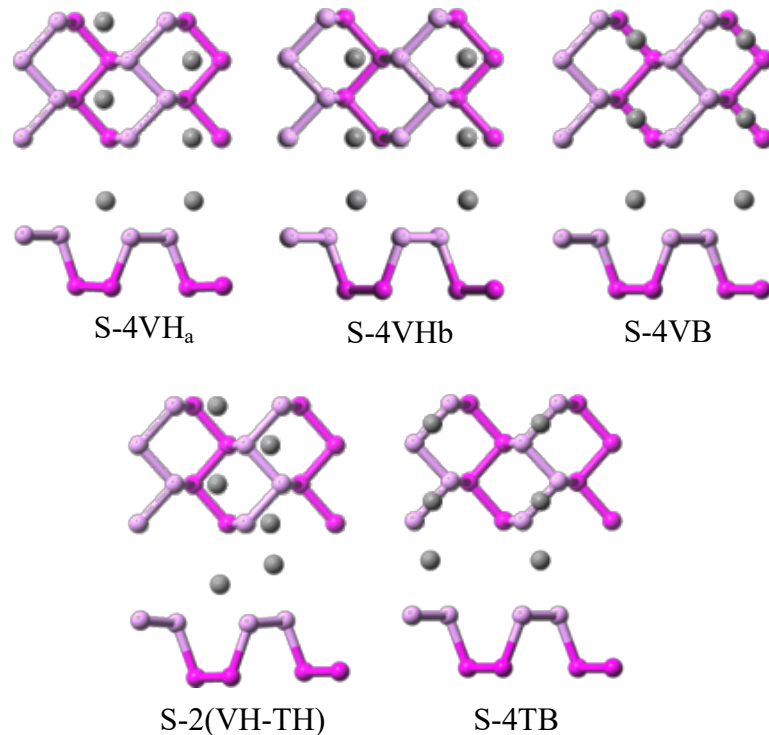
Figure 4.11 Top and side views of the stable Li_4P_{16} system with single-side configurations.

The corresponding adsorption energies and geometric properties are listed in Table 8. It can be seen from the adsorption energy E_a (the 3rd column) that configurations S-4VH$_a$ and S-4VH$_b$ are two relatively stable structures, as compared to the other three stable single-side configurations. Comparing the values in the 4th and 5th columns in Tables 6 and 8, we found that the nearest Li-P distances keep almost the same values in both LiP_{16} and Li_4P_{16} systems, while the vertical distances d of the Li atom at VH, VB and TB sites in Li_4P_{16} are about 0.1-0.3 Å higher than those in LiP_{16}, indicating a vertical increase of phosphorene layer when more Li atoms attracted by P atoms, and therefore, a slightly expansion in volume. This phenomenon is also found when more Li atoms adsorbed to phosphorene (see the results and discussions for Li_6P_{16}, Li_8P_{16}, and $Li_{16}P_{16}$ systems in the following sections).

Table 8. Calculated adsorption energy (E_a), distances between Li and the nearest neighbor P atoms on phosphorene (d_{Li-P}), the vertical distance (d), and the nearest Li-Li distance (d_{Li-Li}) for the stable single-side (up panel) and double-side (bottom panel) configurations of the Li_4P_{16} system.

system	Configuration	E_a (eV/Li)	d_{Li-P} (Å)	d (Å)	d_{Li-Li} (Å)
Li_4P_{16} Single side adsorption	S-4VH$_a$	-1.968	2.46, 2.53	2.59	3.31
	S-4VH$_b$	-1.949	2.42, 2.56	2.60	3.31
	S-4VB	-1.885	2.41	2.72	3.31
	S-2(VH-BH)	-1.769	2.44, 2.63(VH) 2.69 (TH)	2.55(VH) 3.38(TH)	3.00
	S-4TB	-1.404	2.58	3.38	3.31
Li_4P_{16} Double side adsorption	D-2(VH/VH)$_a$	-2.090	2.41, 2.51	2.52	4.62
	D-2(VB/VB)	-2.073	2.31	2.64	4.62
	D-(VH-VB)/(VH-VB)	-2.048	2.41, 2.51(VH) 2.40 (VB)	2.51(VH) 2.60 (VB)	4.40
	D-2(VH/VH)$_b$	-1.978	2.41, 2.54	2.48	3.31

D-2(VH/VH)$_a$ D-2(VB/VB)   D-(VH-VB)/(VH-VB)   D-2(VH/VH)$_b$
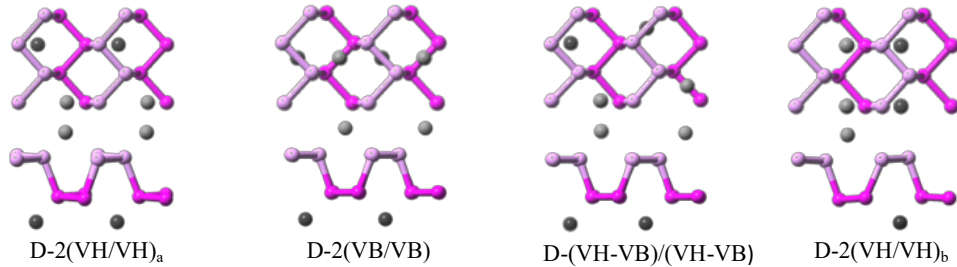
Figure 4.12 Top and side views of the stable Li_4P_{16} system with double-side configurations.

Similar to our consideration in searching stable double-side configurations for Li_2P_{16} structures, we added two more Li atoms on the other side of the four-stable single-side configurations in Li_2P_{16} system (*i.e.*, the four structures shown in Figure 4.9), and constructed 36 initial double-side configurations. Among them, only four stable structures are obtained after fully relax. They are denoted by D-2(VH/VH)$_{a/b}$, D-2(VB/VB), and D-

(VH-VB/VH-VB), respectively, where the subscripts a and b indicate the distribution of the four Li atoms in the same configuration with different symmetry. The top and side views of these stable structures are shown in Figure 4.12 and the corresponding energetic and geometric properties are also listed in Table 8. Comparing the adsorption energy E_a (the 3rd column in Table 8) for all the obtained stable configurations in Li_4P_{16} system, we found that all the double-side configurations have lower in energy than those of single-side configurations, and the relatively more stable configurations are the double-side configurations D-2(VH/VH)$_a$ and D-2(VB/VB), followed by the double-side configuration D-(VH-VB/VH-VB). Furthermore, as shown in the last column in Table 8, the Li-Li distance in these relatively stable structures are 4.62 Å in configurations D-2(VH/VH)$_a$ and D-2(VB/VB) and 4.40 Å in the configuration D-(VH-VB/VH-VB), therefore, the repulsive interactions between them are still weak.

4.4.4 Li_6P_{16} System

We added two more Li atoms on the same side of stable configurations S-4VH$_a$ and S-4VH$_b$ obtained in Li_4P_{16} system (*i.e.*, the structures are shown in Figure 4.13) to search the stable configurations for Li_6P_{16} system with single side adsorption. The additional two Li atoms were loaded at the other two VH sites in two of the four 1x1 unit cells, forming VH-VH pairs. Since some of the initial Li-Li distances (*e.g.*, 1.72 Å) were shorter than the Li-Li bond length (2.68 Å), those Li atoms push each other away during the relaxation, leading to two Li atoms moved up to TH sites, similarly as found in the single-side adsorption of Li_4P_{16} system. Two stable configurations S-4VH-2TH$_{a/b}$ was then obtained, where the subscripts a and b indicate the distribution of the six Li atoms in the same configuration with different symmetry. The top and side views of these stable

89

configurations are shown in Figure 4.13 and the corresponding energetic and geometric properties are also listed in Table 9. It was found that the Li-P bond lengths at VH and TH sites are same in both configurations (see the 4th column in Table 9), while the vertical and the Li-Li distances (see the 5th and 6th columns in Table 9) are slightly different. The increase in the vertical distance implies the slight volume expansion, and the shortness in the Li-Li distance will increase more repulsive interaction, therefore the adsorption energy in the configuration S-4VH-2TH$_b$ is about 0.044 eV higher than that in configuration S-4VH-2TH$_a$ (see the 3rd column in Table 9).

S-4VH-2TH$_a$ S-2VH-4TH$_b$
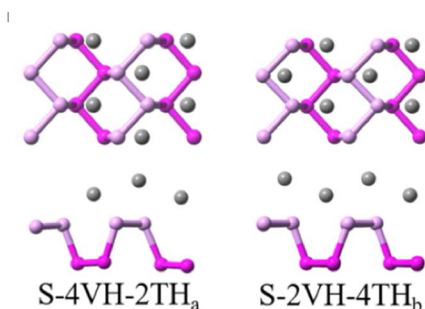
Figure 4.13 Top and side views of the stable Li$_6$P$_{16}$ system with single-side configurations.

D-4VH/2VH   D-4VB/2VB   D-4TB/2VB
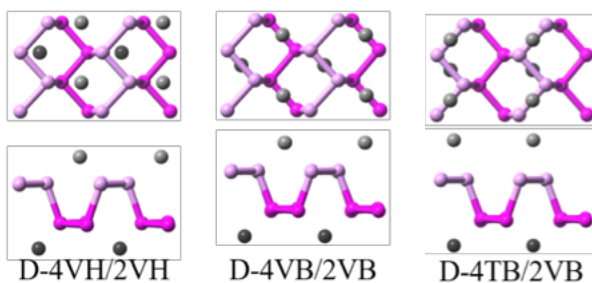
Figure 4.14 Top and side views of the stable Li$_6$P$_{16}$ system with double-side configurations.

When the two more Li atoms were added on the other side of the stable single-side configurations of the Li$_4$P$_{16}$ system (*i.e.*, the configurations shown in Figure 4.11), 12 initial

double-side configurations were constructed. It should be noticed that the Li distribution in the Li_6P_{16} system is asymmetric because the number of Li atoms on both sides is different, leading to difficulties in stabilizing the Li_6P_{16} system. As the results, only three stable configurations are obtained after fully relax. They are denoted by D-4VH/2VH, D-4VB/2VB, and D-4TB/2VB, respectively. The top and side views of these stable configurations are shown in Figure 4.14 and the corresponding energetic and geometric properties are also listed in Table 9. Similar to Li_2P_{16} and Li_4P_{16} systems, the double-side configurations have lower adsorption energy (the 3rd column in Table 9) than those of the single-side configurations, and the relatively more stable configurations are the double-side configurations D-4VH/2VH, followed by the double-side configuration D-4VB/2VB and D-4TB/2VB.

Table 9. Calculated adsorption energy (E_a), distances between Li and the nearest neighbor P atoms on phosphorene (d_{Li-P}), the vertical distance (d), and the nearest Li-Li distance (d_{Li-Li}) for the stable single-side (up panel) and double-side (bottom panel) configurations of the Li_6P_{16} system.

system	Configuration	E_a (eV/Li)	d_{Li-P} (Å)	d (Å)	d_{Li-Li} (Å)
Li_6P_{16} Single side adsorption	S-4VH-2THa	-1.862	2.43, 2.58 (VH) 2.78 (TH)	2.54 (VH) 3.49 (TH)	3.11
	S-2VH-4THb	-1.818	2.43, 2.58 (VH) 2.78 (TH)	2.65 (VH) 3.57(TH)	2.96
Li_6P_{16} Double side adsorption	D-4VH/2VH	-2.034	2.41, 2.52	2.58	3.36
	D-4VB/2VB	-1.954	2.40	2.67	3.36
	D-4TB/2VB	-1.657	2.40 (VB) 2.57 (TB)	2.68 (VB) 3.41 (TB)	3.36

4.4.5   Li$_8$P$_{16}$ System

When two Li atoms were intercalated to each 1x1 unit cell at VH, VB and TB sites, they form VH-VH, VH-VB, VH-TB, VB-VB, VB-TB, and TB-TB pairs. The corresponding initial single-side configurations were constructed and denoted by S-4(VH-VH), S-4(VH-VB)$_{a/b}$, S-4(VH-TB)$_{a/b}$, S-4(VB-VB), S-4(VB-TB)$_{a/b}$, and S-4(TB-TB), respectively, where the subscripts a and b indicate the distribution of the eight Li atoms in the same configuration with different symmetry. These structures were fully relaxed and only five of them were found stable. Figure 4.15 shows the top and side views of the five stable Li$_8$P$_{16}$ structures with Li atoms located at the single-side adsorption. The corresponding adsorption energies and geometric properties are listed in Table 10. Due to the high Li concentration, the Li-Li repulsive interactions play the role and compete with the Li-P attractive interactions in stabilizing the systems. For example, in the initial configuration of S-4(VH-VH), S-4(VH-VB)$_{a/b}$, S-4(VH-TB)$_{a/b}$, the distances of Li-Li pairs were 0.86 Å, 1.71 Å, and 2.36 Å, respectively, which are much shorter than the Li-Li bond length of 2.68 Å. During the relaxation, Li atoms at the VH sites will push Li atoms at other sites in the same unit cell to the positions at TH sites. As the results, these initial configurations were finally stabilized to the structures with S-4(VH-TH) configuration (see the first panel in Figure 4.15 with the Li-Li distances increased to 3.0 Å (about 0.3 Å larger than the Li-Li bond length of 2.68 Å, see the 6th column in Table 10). Such a system has the lowest adsorption energy (-1.826 eV/Li) among other single-side configurations. Another example is found in the initial configurations S-4(VB-TB)$_{a/b}$, in which the initial Li-Li distance is either 2.90 Å (for type a) or 2.39 Å (for type b). During the relaxation, Li atoms at TB sites were pushed to a different vertical level with the Li-Li distances increased

to 2.92-3.02 Å. Similar results are also found in the initial configurations S-4(VB-VB) and S-4(TB-TB), in which the initial Li-Li distances were set around 1.65 Å. During the relaxation, we found that two Li atoms in each unit cell push each other vertically to reduce the Li-Li repulsive interactions, resulting one of the Li atoms moved up away from phosphorene layer with the vertical distance of 5.42/6.02 Å and the Li-Li distance of 3.03/3.06 Å. While these Li atoms were still on the top of the VB or TB site with the same type of configurations as S-4(VB-VB) and S-4(TB-TB).

S-4(VH-TH)   S-4(VB-TB)$_a$ S-4(VB-TB)$_b$

S-4(VB-VB)   S-4(TB-TB)
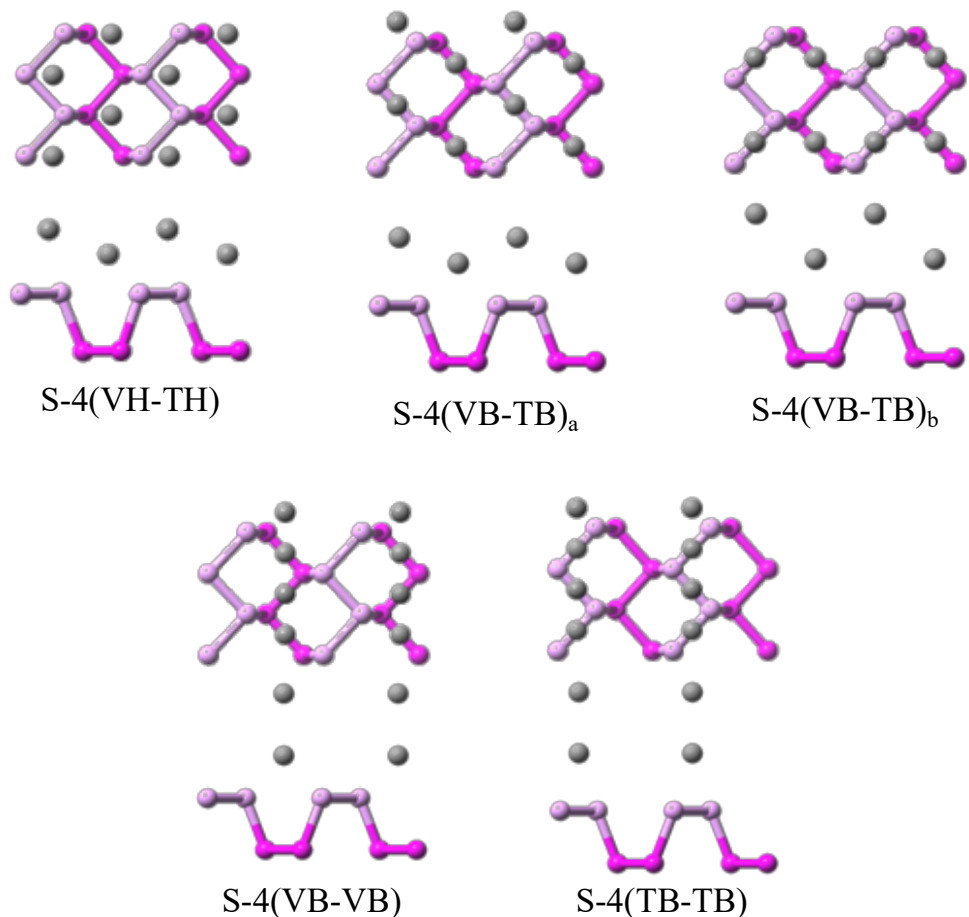
Figure 4.15 Top and side views of the stable Li_8P_{16} system with single-side configurations.

The double-side configurations for Li_8P_{16} system were constructed by adding another 4 more Li atoms on the other side of the stable single-side configurations of Li_4P_{16} system. Thus, in each 1x1 unit cell, one Li atom is located at the VH, or the VB or TB site above phosphorene layer and the other is located at the VH, or VB or TB site below phosphorene layer. Obtained the stable double-side configurations of Li_8P_{16} system are shown in Figure 4.16, named as D-4(VH/VH), D-4(VH/VB), D-4(VB/VB)$_{a/b}$, D-4(VB/TB)$_{a/b}$, and D-4(TB/TB)$_{a/b}$, respectively, where subscriptions a and b distinguish the different symmetry in the same configuration. The corresponding adsorption energies and geometric properties are also listed in Table 10. As can be seen from Table 10, the most stable structure among the stable single/double-side configurations in Li_8P_{16} system is the one with D-4(VH/VH) configuration (E_a=-2.007 eV/Li). Another three double-side configurations (*i.e.*, D-4(VH/VB) and D-4(VB/VB)$_{a/b}$) are about 0.042-0.085 eV higher than the configuration of D-4(VH/VH), but about 0.096-0.16 eV lower than the two single-side configurations (*i.e.*, S-4(VH-TH) and S-4(VB-TB)$_a$). Furthermore, the single-side configuration (*i.e.*, S-4(VB-TB)$_b$) with four Li atoms pulled up away from the phosphorene layer is still competitive with the double-side configurations of D-4(VB/TB)$_a$ and D-4(VB/TB)$_b$. More interesting is found that the single-side configuration S-4(VB/VB) is even relatively stable than the double-side configuration D-4(TB/TB)$_{a/b}$, indicating that when more Li atoms load on the phosphorene, some Li atoms prefer to stay at single-side at VB sites with higher vertical distance instead of staying at double sides at TB sites with lower vertical distances. Comparing the nearest Li-P distance and vertical distance *d* with the corresponding double-side Li_4P_{16} configurations, we found that the Li-P distances did not change too much (see the 4th column in Table 10), but the vertical distances *d* became higher (see the 5th column

in Table 10), indicating a small vertical elongation of phosphorene layer due to the more Li-P attractions when more Li atoms were added on the phosphorene. Again, in all stabilized structures of the Li_8P_{16} system, the repulsive force between Li atoms drove Li atoms to occupy different sites with Li-Li distance around 3.0 Å (see the 6th column in Table 10), and no Li-clustering was found.
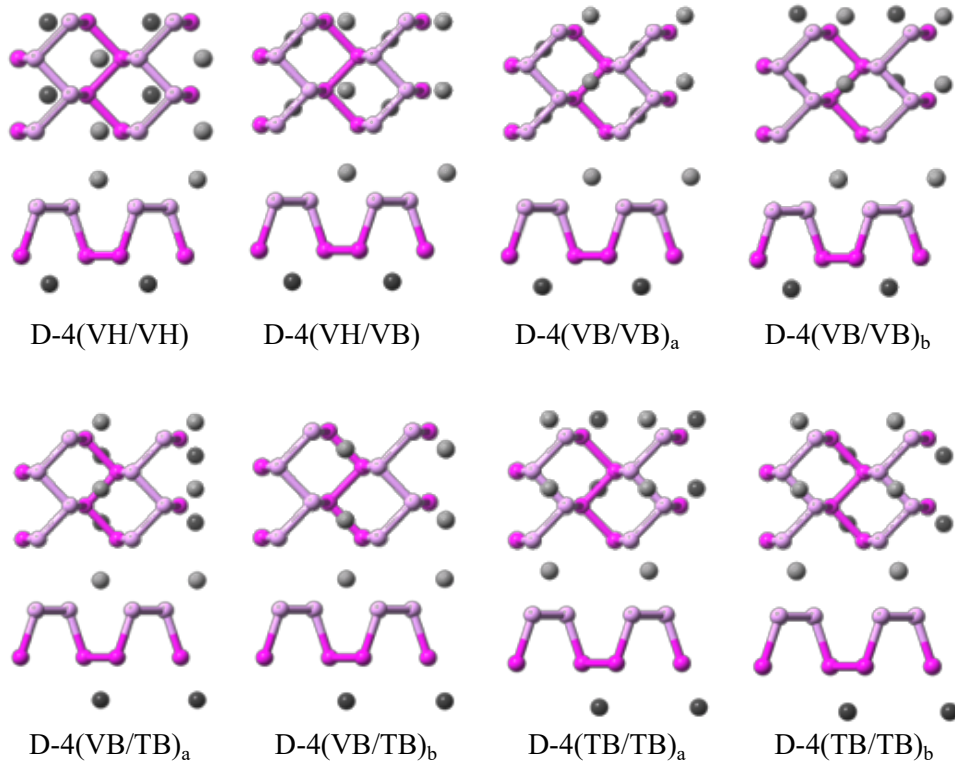
Figure 4.16 Top and side views of the stable Li_8P_{16} system with double-side configurations.

Table 10. Calculated adsorption energy (E_a), distances between Li and the nearest neighbor P atoms on phosphorene ($d_{Li\text{-}P}$), the vertical distance (d), and the nearest Li-Li distance ($d_{Li\text{-}Li}$) for the stable single-side (up panel) and double-side (bottom panel) configurations of the Li_8P_{16} system.

system	Configuration	E_a (eV/Li)	$d_{Li\text{-}P}$ (Å)	d (Å)	$d_{Li\text{-}Li}$ (Å)

Li_8P_{16} Single side adsorption	S-4(VH-TH)	-1.826	2.43, 2.59(VH) 2.78 (TH)	3.47	3.00
	S-4(VB-TB)$_a$	-1.805	2.44(VB), 2.94 (TB)	2.66 (VB), 3.68 (TB)	3.02
	S-4(VB-TB)$_b$	-1.712	2.46 (VB), 3.70 (TB)	2.55 (VB), 4.34 (TB)	2.92
	S-4(VB-VB)	-1.658	2.49	2.66	3.06
	S-4(TB-TB)	-1.481	2.65	3.35	3.03
Li_8P_{16} Double side adsorption	D-4(VH/VH)	-2.007	2.40, 2.53	2.62	3.31
	D-4(VH/VB)	-1.965	2.41, 2.54(VH) 2.40(TB)	2.63(VH) 2.74 (TB)	3.31
	D-4(VB/VB)$_a$	-1.928	2.40	2.74	3.31
	D-4(VB/VB)$_b$	-1.922	2.40	2.75	3.31
	D-4(VB/TB)$_a$	-1.719	2.40(up) 2.53(down)	2.78(up) 3.44(down)	3.31
	D-4(VB/TB)$_b$	-1.716	2.40 (up) 2.53 (down)	2.78(up) 3.44(down)	3.31
	D-4(TB/TB)$_a$	-1.520	2.53	3.43	3.31
	D-4(TB/TB)$_b$	-1.517	2.53	3.43	3.31

4.4.6 $Li_{16}P_{16}$ System

When more than 8 Li atoms were intercalated in the 2×2 phosphorene, we found that there is no more stable configures for the single-side adsorption. Furthermore, as we found in the case of Li_6P_{16}, when the Li distribution is asymmetric on both sides, it is hard to find the stable configurations for Li_nP_{16} (8 < n <16) systems with P-P bonds unbroken. Therefore, at such high Li concentration, we focused on finding, for instance, the possible existence of double-side configurations in $Li_{16}P_{16}$ system with symmetric Li distribution on both sides and no Li clustering. Following the same scheme that we used in constructing double-side configurations for Li_nP_{16} (n=2, 4, 8) systems, we added 8 Li atoms on the other side of the five stable single-side configurations obtained in Li_8P_{16} system to construct the double-side configurations for $Li_{16}P_{16}$, and 5 stable structures are obtained after full relaxation. They are named by D-4(VH-VH/VH-VH), D-4(VB-TB/VB-TB)$_{a/b}$, D-4(VB-

VB/VB-VB), and D-4(TB-TB/TB-TB), respectively. Figure 4.17 shows the top and side views of these stable structures, and Table 11 lists the corresponding adsorption energies and geometric properties.

D-4(VH-TH/VH-TH)   D-4(VB-TB/VB-TB)$_a$ D-4(VB-TB/VB-TB)$_b$

D-4(VB-VB/VB-VB)   D-4(TB-TB/TB-TB)
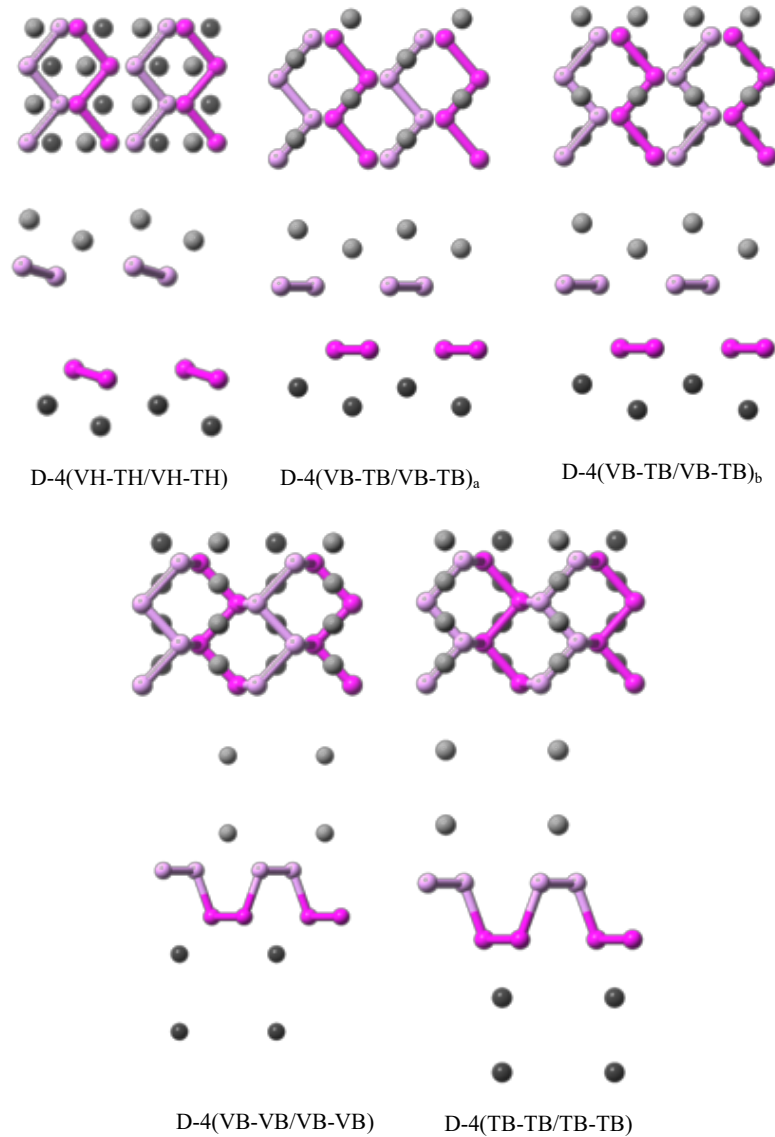
Figure 4.17 Top and side views of the stable $Li_{16}P_{16}$ system with double-side configurations.

At this high Li concentration, we found two cases of Li atoms adsorbed on phosphorene layer. In the first case, due to the strong Li-P attractive interaction between

Li and P atoms on both sides, the puckered phosphorene layer was separated during the relaxation, forming buckled up and down zigzag chains (see the configurations D-4(VH-VH/VH-VH), D-4(VB-TB/VB-TB)$_a$ and D-4(VB-TB/VB-TB)$_b$ in Figure 4.17). In the second case, half of the Li atoms located at the zigzag valley move up/down from phosphorene layer (see the configurations D-4(VB-VB/VB-VB), and D-4(TB-TB/TB-TB) in Figure 4.17). Interesting is found that the structures in the first case are relatively stable than these in the second case (see the 3rd column in Table 11), in particular, the structure with all Li atoms in the zigzag valley (*i.e.*, the D-4(VH-VH/VH-VH) configuration) is the most stable (*i.e.*, E_b=-2.046 eV/Li) in the Li$_{16}$P$_{16}$ system, and even more stable than the most stable structure in Li$_8$P$_{16}$ system (*i.e.*, the D-4(VH/VH) configuration), indicating the ability of phosphorene to accommodate four Li atom per 1×1 unit cell. But the cost is the volume expansion/bond broken between the P atoms.

Table 11. Calculated adsorption energy (E_a), distances between Li and the nearest neighbor P atoms on phosphorene (d_{Li-P}), the vertical distance (d), and the nearest Li-Li distance (d_{Li-Li}) for double-side configurations of the Li$_{16}$P$_{16}$ system.

system	Configuration	E_a (eV/Li)	d_{Li-P} (Å)	d (Å)	d_{Li-Li} (Å)
Li$_{16}$P$_{16}$	D-4(VH-VH/VH-VH)	-2.046	2.38, 2.50(VH) 2.58(TH)	3.30(VH) 4.17(TH)	2.91
	D-4(VB-TB/VB-TB)$_a$	-1.896	2.40(VB) 2.64(TB)	2.82 (VB) 3.88 (TB)	2.95
	D-4(VB-TB/VB-TB)$_b$	-1.757	2.34(VB) 2.79(TB)	2.93(VB) 3.74(TB)	2.55
	D-4(VB-VB/VB-VB)	-1.752	2.50	2.84, 5.43	3.306
	D-4(TB-TB/TB-TB)	-1.648	2.65	3.48, 6.03	3.306

Figure 4.18 shows the relative energy as function of molecular dynamics (MD) steps for the relaxation procedure of 16 Li atoms inserted to both sides of phosphorene layer with the initial configuration D-4(VH-VH/VH-VH), and the relaxation procedure of the 'fractured' phosphorene layer which was obtained by removing the 16 Li atom from the fully relaxed $Li_{16}P_{16}$ system with the configuration D-4(VH-VH/VH-VH). The relative energy is defined as the total energy difference between the initial and final stage of the system. The time step was set to 0.5 fs in the MD simulation. The top (up) and side (down) views of several intermediate configurations are illustrated in the insets with the starts representing the relative energy at corresponding MD steps. The light and dark gray balls represent Li atoms above and below the phosphorene monolayer, respectively; while, the balls with light and dark purple color denote phosphorus on the ridge and in the valley, respectively.

We found that, during the relaxation process, 8 Li atoms on each side of phosphorene, for example in D-4(VH-VH/VH-VH) configuration (see Figure 4.18 (a)), strongly attract P atoms on both sides of phosphorene layer, leading to the opposite motion of P atoms. As the result, the P-P bonds between P atoms at the valley and the ridge were broken, and the puckered phosphorene layer was separated to two buckled above/below zigzag chains with the separation of about 3.61 Å, similar as a volume expansion of ~56% during the charging process in LIB. Such kind of structures was also found in $Li_{10}P_{16}$, $Li_{12}P_{16}$, and $Li_{14}P_{16}$ systems. So, the question is whether such broken bonds could be self-reformed after Li atoms removed from phosphorene? To unravel this puzzle, we examined the $Li_{16}P_{16}$ structures in the first case by relaxing the systems after removing Li atoms.
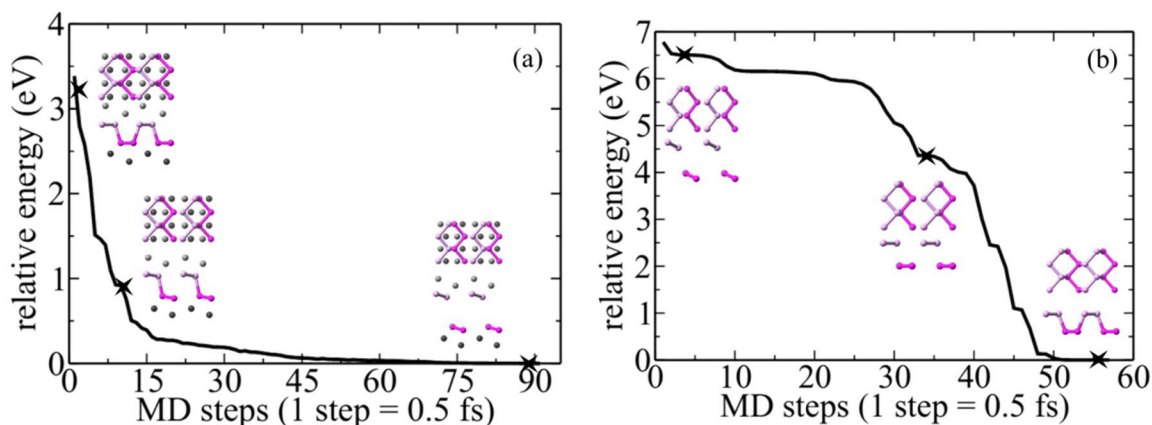
Figure 4.18 The relative energy as function of molecular dynamics (MD) steps for (a) the lithiation process with the initial configuration D-4(VH-VH/VH-VH) and (b) the delithiation process by removing the 16 Li atom from the fully relaxed $Li_{16}P_{16}$ system with the configuration D-4(VH-VH/VH-VH).

Figure 4.18 (b) shows, for example, the relaxation process of the stable $Li_{16}P_{16}$ system with the configuration D-4(VH-VH/VH-VH) after removing the 16 Li atoms (mimic the delithiation process). Since all Li atoms are removed, there is no Li-P attractive force to pull phosphorus away from each other, and the buckled zigzag chains became flat (in about 17 fs) and then moved close each other reforming the P-P bonds, and finally, the puckered phosphorene structure was recovered (in about 10 fs). The volume expansion of the phosphorene during Li insertion/discharging disappeared after the Li extraction, showing the reversibility of phosphorene during Li insertion/extraction process as an anode material. Such kind of reversibility has been observed in very recent multi-cycle *in situ* TEM electrochemical lithiation/delithiation experiment which showed that few-layer-thick phosphorene nanoflakes (less than 10 layers), after delithiation, can completely restore its original morphology and size without any visible structural decomposition even after several cycles. Furthermore, we should point out that even though the Li atoms are close

to each other at this high Li concentration, and the Li-Li distance is about 0.05-0.1 Å shorter than that in the other Li_nP_{16} systems (n=2, 4, 8) (see the last column in Table 11), there is still no Li cluster formed, which is confirmed by the negative formation energy.

Among all the obtained stable structures with the Li adsorption either at the single-side or at the double-side, the most stable configurations for each Li_nP_{16} system are those in which Li atoms always prefer to stay at VH sites along the zigzag direction in the valley. This makes sense because these VH sites are the most preferential sites as predicted by the adsorption energy landscape (as shown in Figure 4.4 (a)). On the other hand, in the Li_nP_{16} systems with higher adsorption energies, more Li atoms have to stay at VB and TB sites. It is also found that the adsorption energy in the most stable double-side configurations, for given n in Li_nP_{16} systems, is always lower than that in the most stable single-side configurations, as the repulsive Li-Li interaction is weaker in the former than in the later.

4.5   Electronic Properties

The electronic properties of phosphorene with various Li_nP_{16} configurations were studied from the total and projected density of states (*i.e.*, DOS and PDOS). The DOS/PDOS for the four most stable single-side configurations in each Li_nP_{16} system (n=1, 2, 4, 8) and the four stable double-side configurations in each Li_nP_{16} system (n=2, 4, 8, 16) were presented in Figure 4.19 (a) and (b), respectively. The Total DOS are plotted with black solid curves, the partial DOS for P atoms are plotted with red dot-dash curves, and the partial DOS for Li atoms are plotted with blue dash curves, respectively. The Fermi level is represented by the black dash line. The DOS for the pristine phosphorene with the DFT band gap of 0.82 eV is also shown on the top of Figure 4.19 (a) and (b).
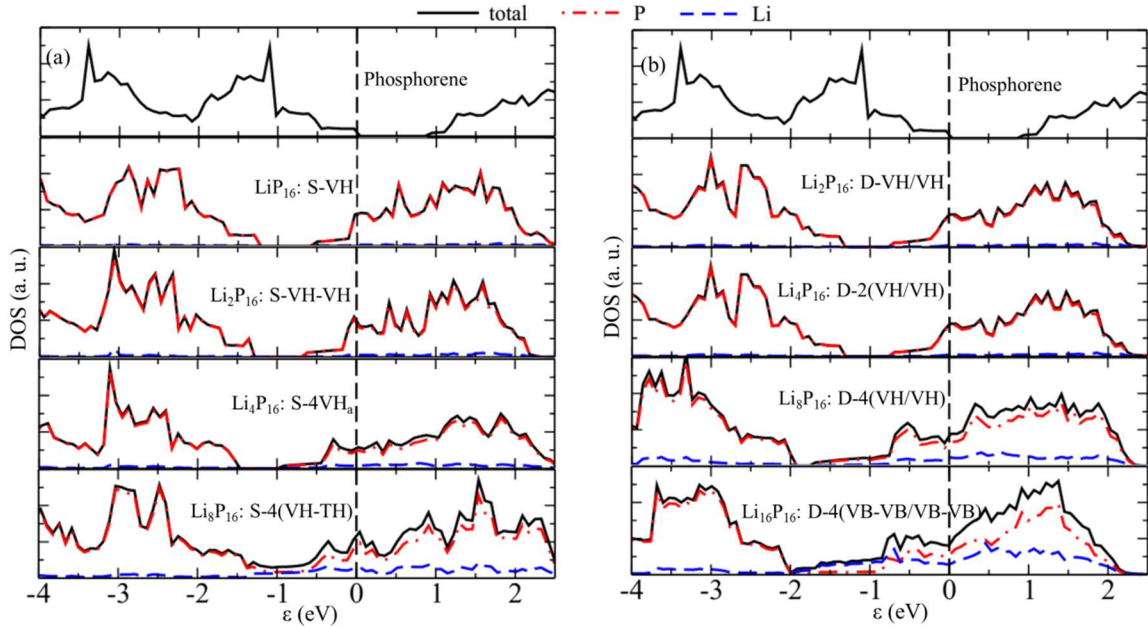
Figure 4.19 The total (DOS) and partial (PDOS) densities of states of some stable single-side (a) and double-side (b) configurations of Li_nP_{16} system with n=1, 2, 4, 8, and 16, respectively.

It can be seen from Figure 4.19 (a) and (b) that during the Li insertion, the tail at the bottom of the conduction band (CB) extends towards to the top of the valence band (VB) due to the orbital hybridization between Li 2s and P 2p orbitals. On the other hand, the Fermi level upshifts to the CB, due to the charge transfer from the Li atoms to phosphorene, indicating the ionic bonding between Li and P atoms. The PDOS of Li is mainly appearing in the CB near the Fermi energy, indicating that the 2s electron of Li contributes to the DOS near the Fermi level. With more Li atoms adsorbed, more active charge transfer from the Li atoms to phosphorene leading to the Fermi level shift even further, more Li PDOS appear close to the bottom of CB, and the energy band gap gradually diminishes and eventually disappears. In particular, the semiconductor-metal transition was observed in

both single-side and double-side adsorption which is expected for the electron transport to be sufficiently fast in the phosphorene anode.

4.6   Specific capacity

The theoretical capacity of LIB was estimated by Faraday's law through studying the formation energy involved in the intercalation process, which is defined by

$$E_f\left(Li_xP\right) = E_{Li_xP} - E_P - xE_{Li},$$ (4-5)

where E_{Li_xP} is the total energy per formula unit of the Li$_x$P system, E_P, the energy of the P atom in phosphorene, E_{Li}, the energy of the Li atom in the BCC phase, and x, the Li:P ratio.

To study the stability in forming the Li$_x$P system and therefore, to predict the Li special capacity, we calculated the formation energy of the Li$_x$P system using Eq. (5) and illustrated it, as the function of x, in Figure 4.20. The black open/red solid circles in the range of $0 \leq x \leq 0.5$ represent the stable configurations of the Li$_x$P systems with the single-side adsorption (without/with the van der Waals correction), and the black open/red solid triangles in the range of $0.125 < x \leq 1.0$ represent the stable configurations of the Li$_x$P system with the double-side adsorption (without/with the van der Waals correction), respectively. Apparently, the van der Waals interactions lower the formation energy by about 0.2 - 0.4 eV. In contrast to the Li intercalation in graphene where the formation energy is always positive, all the formation energies of the Li$_x$P system are negative after van der Waals correction (see the solid circles and triangles in Figure 4.20), showing the

stability of forming Li$_x$P system during the Li intercalation and no Li clustering or dendrite occurring.
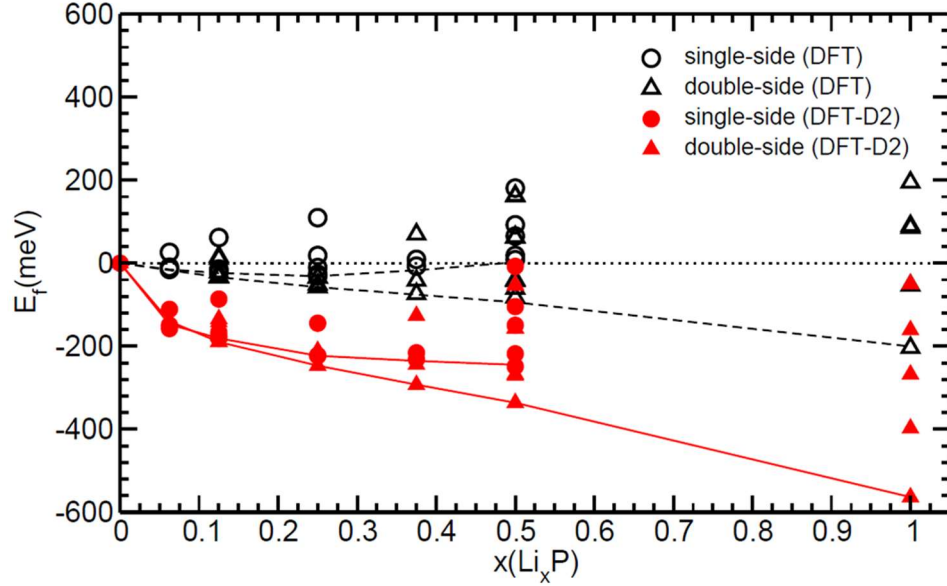
Figure 4.20 The formation energy of the Li$_x$P system with the single-side adsorption (black open/red solid circles) and the double-side adsorption (black open/red solid triangles) with respect to the Li:P ratio x.

The lowest formation energies for the single- and double-site adsorptions, guided by the black dashed-curves for the DFT calculations and red curves for DFT-D2 calculations, decrease monotonically with increasing x (except the single-side adsorption without van der Waals correction). As we have pointed out in the discussion of Li intercalation, no more stable Li$_x$P systems with negative formation energy were found when $x > 0.5$ for the single-side adsorption and $x > 1.0$ for the double-side adsorption, respectively.

The capacity is then defined based on the formation energy of E_{Li_xP} system,

$$C = \frac{x_{max} F}{M_P}, \tag{4-6}$$

104

where x_{max} is the highest atomic ratio of Li to P atoms in the combined Li$_x$P system with negative formation energy or before the possible formation of Li metal phase, F is the Faraday constant (26.8 *Ah/mol*), and M_P is the atomic mass of P atom (31 *g/mol*), respectively.

The achievable capacity limit is determined theoretically by the highest Li:P ratio x_{max} that can be achieved in the most stable configurations of the Li$_x$P system before Li clustering or the formation of Li dendrites. As can be seen from the formation energy (Figure 4.20), in the case of the single-side adsorption, there are no more stable configurations with negative formation energy found for $x \geq 0.5$, and in the case of the double-side adsorption, it was found that the fractured structure of phosphorene cannot restore when more than 16 Li atoms (*i.e.*, $x > 1.0$) were inserted. Therefore, the highest Li to P ratios (x_{max}) is around 0.5 for the single-ide adsorption, and 1.0 for the double-side adsorption. The corresponding specific capacity is then predicted (from Eq. (6)) as ~433 *mAh/g* for the single-side adsorption and is expected as ~865 *mAh/g* for the double-side adsorption, respectively. The theoretically predicted values of special Li capacity on monolayer phosphorene provided a fundamental guide for designing phosphorene as anode material for LIB. Namely, for a parallel layered phosphorene, the Li capacity could reach ~ 433 *mAh/g* without Li dendrite (corresponding to the single-side adsorption case), while, it is a big challenge for synthesis to reach the theoretically predicted value of 865 *mAh/g* (corresponding to the double-side adsorption case) without Li dendrite.
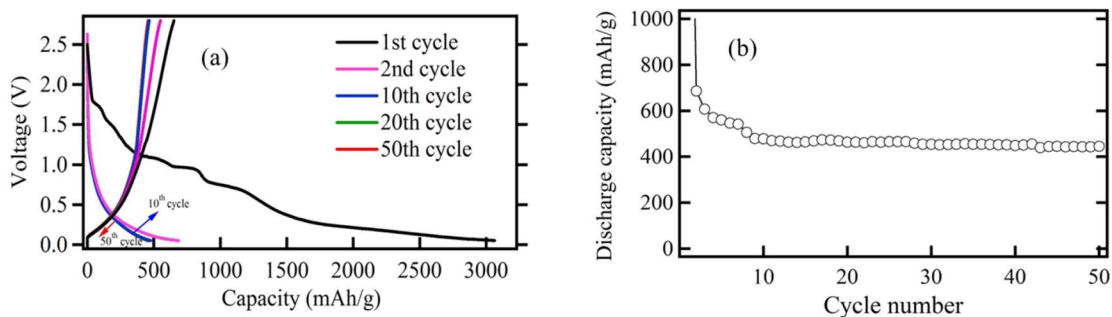
Figure 4.21 Electrochemical characterization of Phosphorene-based coin cells. (a) Charge-discharge Voltage versus capacity curves tested at C/10 rate plotted after the 1st (black), 2nd (pink), 10th (blue), 20th (green), and 50th (red) cycles. (b) Specific discharge capacity cycling at C/10 rate.

Currently, our experimental group performed the very first experimental measurement of lithium storage capacity of few parallel layer phosphorene networks. Figure 4.21 shows the galvanostatic charge-discharge curves of phosphorene/TAB-2 electrode for rechargeable Li-ion battery at the voltage range of 0.05-2.8 V at C/10 rate. It has an initial irreversible discharge capacity of 3065 *mAh*/g during the first cycle. The discharge potential plateau curve was large and flat at ~1 V and 0.4 V vs. Li/Li+. Furthermore, charge-discharge measurement of the phosphorene/TAB-2 (90/10) electrode shows the discharge capacities of 685, 477, and 453 *mAh*/g during the 2nd, 10th, and 30th cycles, respectively. After 30 cycles, it retains very stable discharge capacity of 453 *mAh/g*. The first discharge capacity (Li-insertion) gains a capacity of ~3065 *mAh/g* due to the reaction of the electrolyte at the surface of phosphorene with transferred lithium atoms to form a passivating film, known as solid electrolyte interface (SEI). Once, SEI is formed, it prevents the further electrolyte reaction on the phosphorene surface. Thus, the first discharge profile is always different from the profiles of subsequent cycles. Nevertheless,

the capacity is stabilized to 453 *mAh/g* after 30th cycle and remained highly reversible over 50 cycles. Such value for a few layered phosphorene networks is close to the theoretically predicted value (433 *mAh/g*) for the single-side adsorption of a monolayer phosphorene. As already reported in the experimental results for the Li adsorption on parallel layers graphene, the Li capacity could reach ~ 372 *mAh/g* of graphite (corresponding to the single-side adsorption case), and Li metal might co-exist at high Li concentration (corresponding to the double-side adsorption case). To reach the theoretically predicted value of 744 *mAh/g* (corresponding to the double-side adsorption case), effort must be made to enhance the space between graphene layers, such as the crumpled or curved singe layered graphene nanosheet. It is highly expected that the reversible Li capacity for phosphorene could increase and reach the theoretically expected value of ~865 *mAh/g* for the double-side adsorption, if, for instance, the single layered phosphorene can be arranged as 'house card', as found in the case of graphene, or capped with other 2D materials.

4.7   Conclusion

The novel features of phosphorene as anode materials for LIB have been characterized based on the first principle calculations. When adsorbed on phosphorene, Li atoms prefer to reside at the most stable VH sites at the valley. The other two metastable sites (*i.e.*, the VB and TB sites) could be occupied when there more Li atoms loaded on phosphorene. The adsorption energy at the most stable VH site is -2.086 eV/Li, indicating strong Coulomb interactions between Li and phosphorene, which are essential in the electrochemical performance for high performance LIB. The diffusion energy barrier of Li on phosphorene shows high anisotropic behavior and is extremely low when Li atom migrates along the zigzag channel at the valley. Estimated diffusion constant also shows

that Li atoms will diffuse ultrafast and directionally along the zigzag direction in the valley (*e.g.*, about 10^{11} times faster than the diffusion across the ridge along the armchair direction). In particular, it was found that the Li diffusion on phosphorene is extremely faster than on graphene and MoS$_2$, which implies that phosphorene may exhibit outstanding high rate capacity.

The most stable structures for Li atoms adsorbed on single/double-side of the phosphorene layer are those in which Li atoms occupy at the VH sites along the zigzag direction in the valley. Importantly, the ability for phosphorene to accommodate Li atoms was found up to about 1:1 (*i.e.*, the ratio of Li:P), demonstrating that the monolayer phosphorene could reach the predicted capacity with 865 *mAh/g*. Experimental measured specific capacity for a few layered phosphorene networks showed the very stable value of 453 after 30th cycle and good cycling performance. A uniform single layered phosphorene with nanoporosity is expected to increase the reversible capacity to the theoretically predicted value. More interesting was found that phosphorene monolayer could self-recover when it was 'distorted/fractured' during Li intercalation at the high Li:P ratio, indicating its reversibility during lithiation/dilithiation (charging/discharging) process. Overall, our theoretical and experimental results show the beneficial properties of Li adsorbed phosphorene including the high specific capacity, the ultrafast and anisotropic diffusivity, the reversibility in charging/discharging, stable cycling performance, and then the good electrochemical performance, which make it an excellent candidate as anode material for high performance Li-ion batteries.

CHAPTER V

DEVELOPMENT OF SCED-LCAO HAMILTONIAN FOR PHOSPHORUS AND

LITHIUM ELEMENTS

5.1 Development of SCED-LCAO Hamiltonian for Phosphorus

5.1.1 The initial database of phosphorus and the preliminary results

The initial database for phosphorus includes small clusters with various symmetries

and the relative energy curve of black phosphorous with respect to the atomic volume [212].

There are many detailed articles about small phosphorus clusters[213] that can be utilized

as an initial guide. Clusters used in our fitting database are listed in Figure 5.1, which are

obtained from DFT calculations with the hybrid B3LYP functional and the aug-cc-pvTZ

basis set. After geometry optimization, the nuclear cores were fixed and coupled cluster

calculations were performed using the CCSD(T) method with the cc-pvDZ and cc-pvTZ

when possible.

There are several allotropes of bulk phosphorus including black, white and red

phosphorus, in which black phosphorous possesses A17 symmetry with space group of

cmca, white phosphorus exists as molecules made up of four atoms in a tetrahedral

structure, and red exists as an amorphous network with 84 P atoms in a unit cell,

respectively. We selected the most stable black phosphorus phase in ambient condition.

The relative energy per atom with respect to the minimal value as a function of volume per

atom obtained by employing the DFT-GGA-US method, is illumined by the black dashed curve in the right side of Figure 5.1.
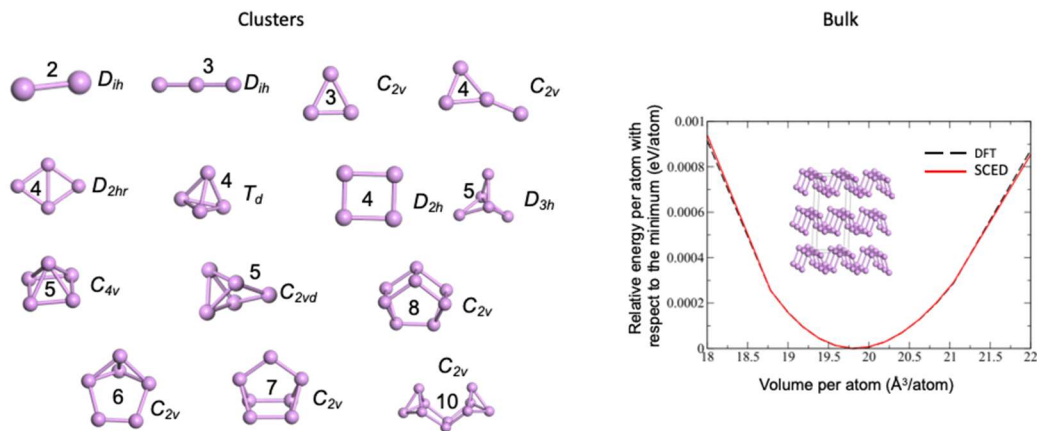
Figure 5.1 The small clusters (left) and bulk phase of the black phosphorus (right) in the database, in which the number of P atoms and the symmetry corresponding to the clusters are indicated [212]. The inset in the phase diagram is the structure of the black phosphorus, the dashed-black curve is the DFT result, and the red curve is the SCED-LCAO fitting result.

Our preliminary fitting results performed by Dr. Paul Tandy (referred as the first candidate set of parameters) fitted very well to the energy curve of black phosphorus phase (see the red curve in Figure 5.1). However, we found that during our robust test, the black phosphorus bulk is unstable after undergoing ~ 1ps. Figure 5.2 exhibits the total energy per atom of black phosphorus as a function of MD steps. The structures at the initial and 3000th step are shown in the inserts. The energy curve was stable at the first 500 steps, then decreased rapidly until about 1500 steps. In the meantime, the bulk structure started to distort at about 500th MD step and then the layered structural properties gradually disappeared.

110
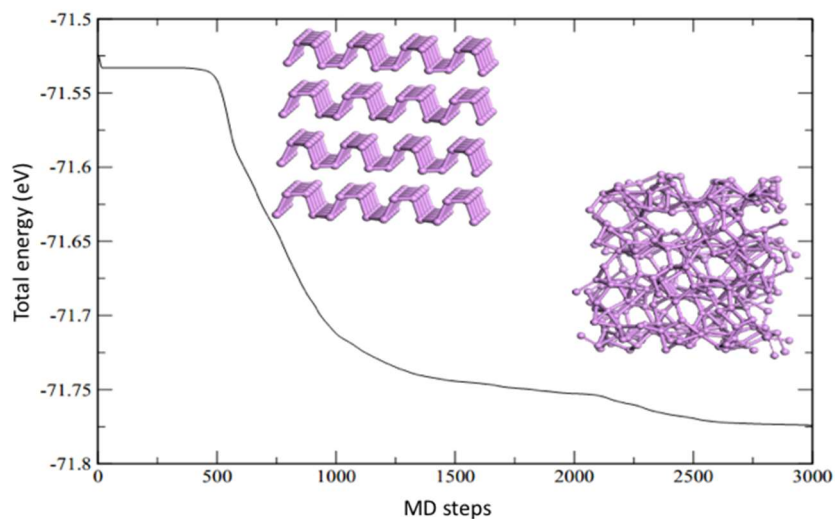
Figure 5.2 Relaxation process of black phosphorus by using the first set of parameters.

Similarly, the structural distortion was also found in the case of the monolayer phosphorene, as shown in Figure 5.3. It shows that the stable structure only lasts about 400 steps. Both robust tests indicated that the first set of parameters could not well characterize the layered feature of black phosphorus and phosphorene and need to be improved to grantee the transferability.
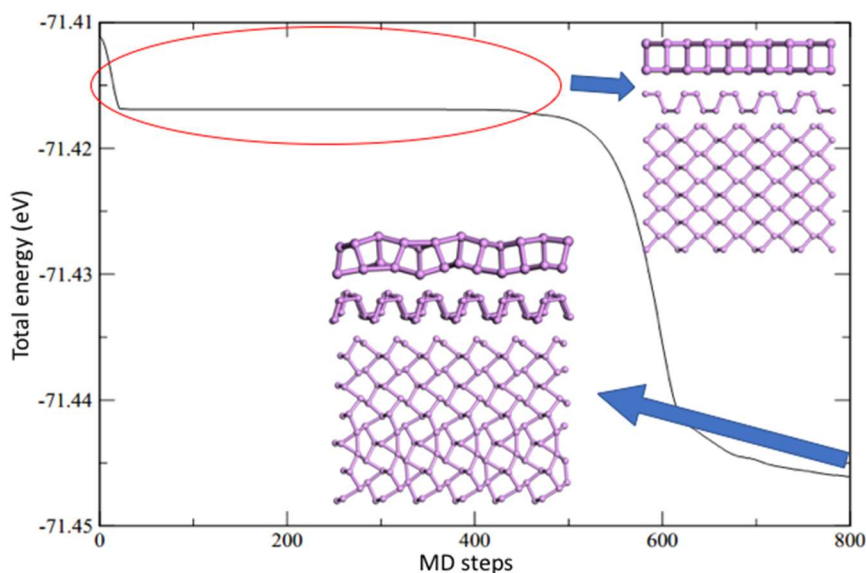
Figure 5.3 Relaxation process of phosphorene by using the first set of parameters. The insets are the side and top views for the initial and final structures of phosphorene, respectively.

5.1.2   Improving database and reconstructing parameters

Two potential solutions appeared in mind while we double checked the parameters and database. First, the parameter B_N in the first set, which is in the parametric functions of $V_N(R_{ik})$ and $\Delta V_N(R_{ik})$, is a large negative number ($\sim$ -13 Å^{-1}), which may be overestimate the interactions distance between electrons and ions $V_N(R_{ik})$. Second, as we mentioned above, the first set of parameters failed in describing the layered structures, probably due to the small unit cell selected in the initial database. It contains four atoms, two of them belong to the lower layer and the other two belong to the upper layer (see the black dashed box in Figure 5.4). While one puckered structure in the single phosphorus layer contains 4 atoms, which indicates that the original unit cell in the initial database may not be enough to include necessary information to describe the puckered structural properties. On the other hand, a cubic unit cell of black phosphorus (see the red dashed box in Figure 5.4) contains 8 atoms, each layer in the unit cell contains 4 atoms and forms the puckered structure which definitely can contain sufficient information about the layer feature in the black phosphorus, and therefore was taken into consideration to improve the database.

Figure 5.4 shows the updated phase diagram of black phosphorus. The black curve represents the energy curve of 4-atom unit cell, calculated using the GGA-US method; and the red curve represents the energy curve of the 8-atom-unit cell, calculated by the GGA-PAW-PBE method. The relative energy with respect to the minimum for the two cases are

different, due to the different potentials used in the calculation. The phase diagram of black phosphorus with 8 atoms in the unit cell is deeper than that with 4 atoms in the unit cell, and more localized.
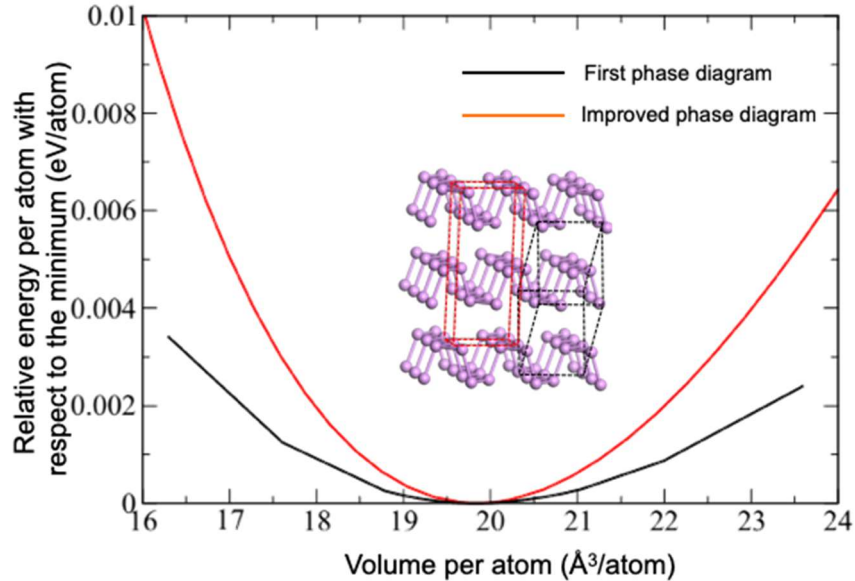
Figure 5.4 Comparison between the original (black curve) and improved (red curve) phase diagram of black phosphorus. The corresponding unit cell are shown on the inserted structure.

Based on the improved database and reconstructing the parameter B_N, we obtained the second set of optimized parameters and preformed a robust test for both the black phosphorus and phosphorene. Figure 5.5 gives the total energies of both structures as a function of MD steps. The red curve indicates the total energy per atom of phosphorene and the black curve indicates that of black phosphorus. The inserted structures on the top of the energy curves are the top view and side view of phosphorene at about 4000th step. The inserted structure below the energy curves is the relaxed black phosphorus at about 4000th step. Even though the slight distortion was found after the 4000th step, the second

set of parameters indeed improved significantly by comparing the energy curve and the relaxed structure with those of the first set.

However, the stable structure is only one important factor to check the transferability and reliability of the Phosphorus Hamiltonian. To make the Hamiltonian more reliable, other important factors such as the electronic properties should also be taken into consideration. In this case, we calculated the band gaps of black phosphorus and phosphorene by using the second set of parameters and found that both band gaps are zero, which are totally different from experimental results and other theoretical calculations (*i.e.* 0.3 eV for black phosphorus and 1.5~2 eV for phosphorene).
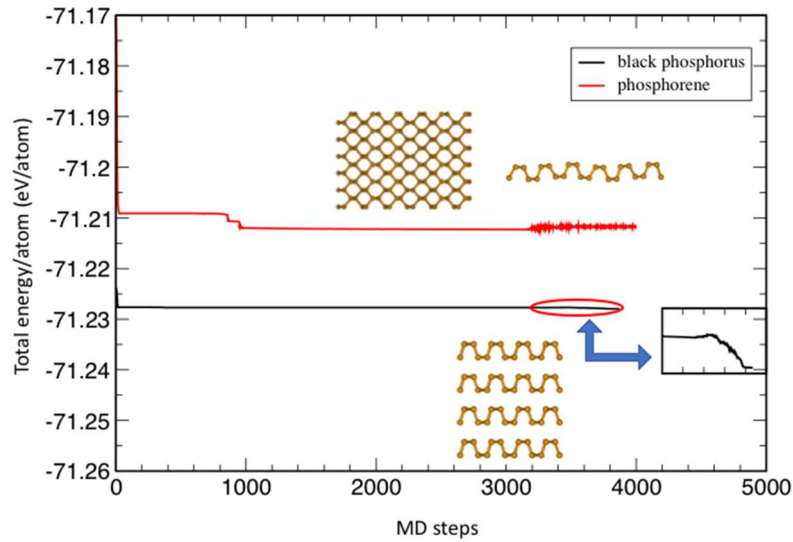
Figure 5.5 The total energies per atom of black phosphorus and phosphorene as functions of MD steps (based on the 2nd set of parameters).

Similar to what we did before, we double checked this set of parameters and found that the parameter d_N in $V_N(R_{ik})$, characterizing the interaction separation, is negative. After reconstructing such parameter, we obtained the third group of parameters.

The robust tests of the third set of parameters on black phosphorus and phosphorene are shown in Figure 5.6. The black curve is the energy of black phosphorus and the red curve is that of phosphorene. The related relaxed structures and the bandgaps after 6000th steps are inserted behind each curve. Both structures are very stable for more than 6000th steps and no distortion was found. The energy gap of black phosphorus is 0.54 eV and the energy gap of phosphorene is 1.84 eV, which are close to the experimental measurements. All these indicate that the third set of parameters are more reliable than the second one.

Quit recently, a new allotrope in the phosphorus family, the blue phosphorene with low buckled honeycomb structure has been predicted. It is a challenge testimony for the third set of parameters since no references for the blue phosphorene in our database. A robust test for the newly predicted blue phosphorene is therefore, highly desired to check the transferability of our parameters. However, we found that the blue phosphorene (green curve in Figure 5.6) is stable within the first 6000 MD steps and undergoes a distortion after 6500th MD step, indicating that a further improvement is indeed required.
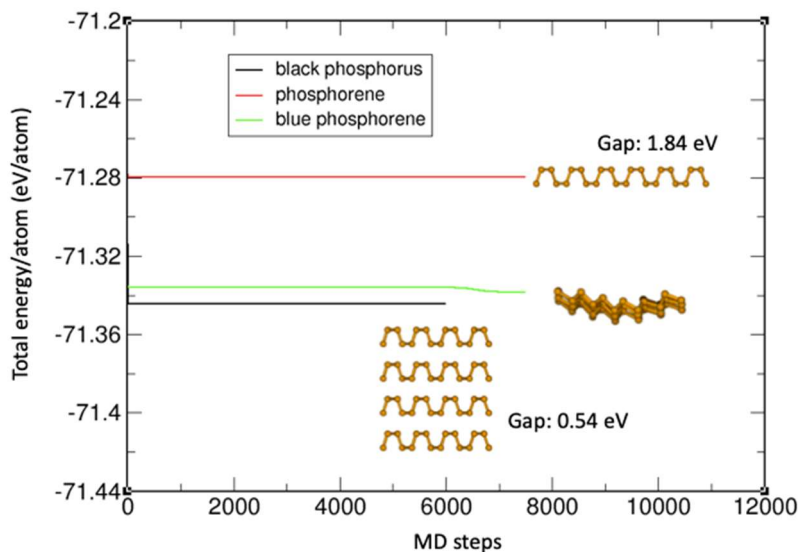
Figure 5.6 Relaxation process of black phosphorus (blue curve), black phosphorene (red curve), and blue phosphorene (green curve) (based on the 3rd set of parameters). The corresponding relaxed structures and band gaps are shown in the insets.

In addition to the check energetics and the stability of black phosphorus, black phosphorene, their electronic band structures are also very important for us to examine our SCED-LCAO Hamiltonian. Figure 5.7 shows the band structure of black phosphorus calculated by GGA-PAW-PBE method (Figure 5.7(a)) and SCED method with the third set of parameters (Figure 5.7(b)). The blue dash lines represent the Fermi level and red dash lines represent the high K points. The GGA method demonstrates a direct band gap while the SCED methods demonstrate an indirect band gap. The curvatures of valance bands are similar, but the bandwidth of SCED band structure is narrower than that of GGA band structure. Even worse, the conduction bands of these two methods are totally different. All the differences between these two band structures indicate that we need to improve the third set of parameters by improving our database with the band structures of the black phosphorus.
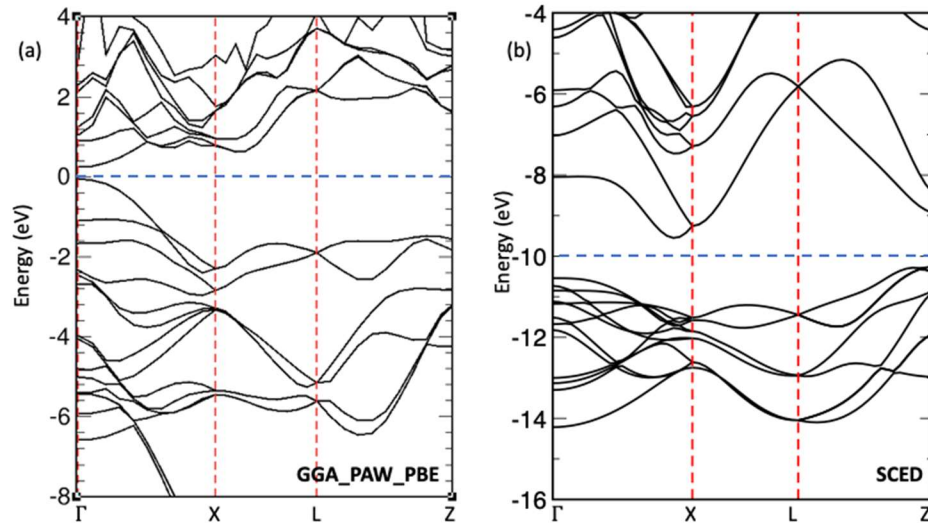
Figure 5.7 Band structure of the black phosphorus calculated with DFT (left) and SCED-LCAO (right) with the 3rd set of parameters.

5.1.3 The final optimized parameters for phosphorus

The final set of parameters was obtained by adding the band structure of the black phosphorus in the databased and preforming both the parameters fitting process and the robust test. They are listed in Table 12.

Table 12. The final set of parameters for SCED-LCAO Hamiltonian of phosphorus

Hamiltonian parameters	values	Hamiltonian parameters	Values
$\varepsilon_s(eV)$	-19.2200000	$U(eV)$	9.86939758
$\varepsilon_p(eV)$	-9.5400000	$\alpha_K(\text{Å}^{-1})$	0.18161236
$\varepsilon_s'(eV)$	-19.44538285	$A_N(eV)$	-1.18400816
$\varepsilon_p'(eV)$	-10.29538460	$B_N(\text{Å}^{-1})$	-4.20914678
$W_p^0(eV)$	-0.48300691	$\alpha_N(\text{Å}^{-1})$	3.04942353
$W_s^0(eV)$	0.70545085	$d_N(\text{Å})$	0.45860964
$\alpha_{p,w}(\text{Å}^{-1})$	1.04837474	$B_z(\text{Å}^{-1})$	2.62768969
$\alpha_{s,w}(\text{Å}^{-1})$	1.05624107		
$\alpha_{pp\pi}(\text{Å}^{-1})$	1.49628600	$B_{sp\sigma}(\text{Å}^{-1})$	1.00684141
$\alpha_{pp\sigma}(\text{Å}^{-1})$	2.11826830	$B_{ss\sigma}(\text{Å}^{-1})$	-0.12084528
$\alpha_{sp\sigma}(\text{Å}^{-1})$	1.81747580	$d_{pp\pi}(\text{Å})$	0.23030581
$\alpha_{ss\sigma}(\text{Å}^{-1})$	2.56687223	$d_{pp\sigma}(\text{Å})$	1.73721339
$B_{pp\pi}(\text{Å}^{-1})$	0.06920524	$d_{sp\sigma}(\text{Å})$	0.95552040
$B_{pp\sigma}(\text{Å}^{-1})$	-0.91705549	$d_{ss\sigma}(\text{Å})$	1.36569455

The phase diagram of SCED-LCAO results of black phosphorus fits the VASP results very well (Figure 5.8 (a)). Fitted overlap matrix elements as a function of the atomic distance are shown in Figure 5.8 (b). The black curve represents the overlap curves of $ss\sigma$; red curve, $sp\sigma$; green, $ps\sigma$; blue curve, $pp\sigma$; and yellow curve, $pp\pi$, respectively. The five orbitals are all normalized, so they cannot exceed unity. On the other hand, the overlap

curve decay to nearly zero within a cutoff of 7 Å. Figure 5.8 (c) shows the fitted Hamiltonian matrix elements. All curves also converged to zero around the cutoff point of 7 Å. Both fitted overlap matrix and Hamiltonian matrix are in good shape characterizing the feature of overlap and Hamiltonian.
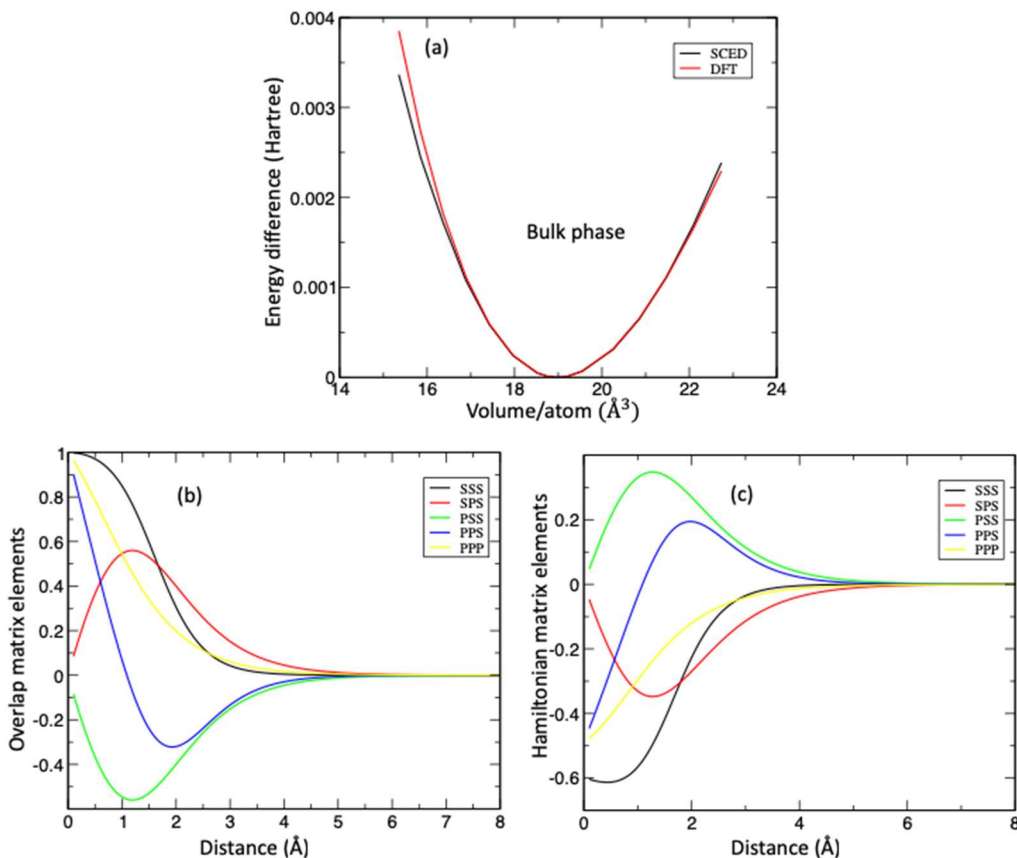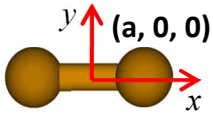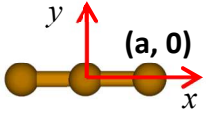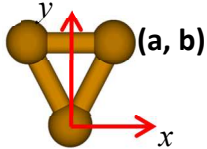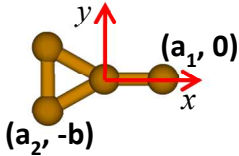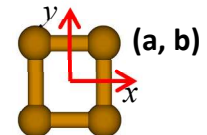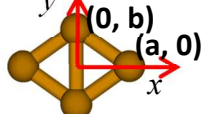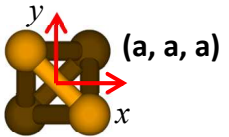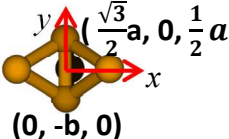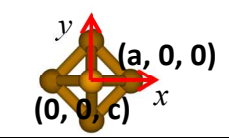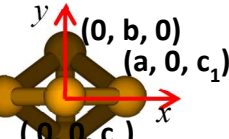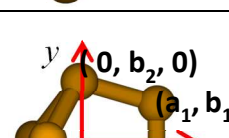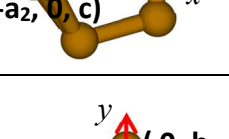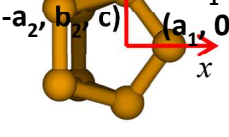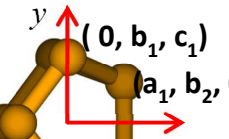
Figure 5.8 (a) The phase diagram of the black phosphorus calculated with DTF (red) and SCED-LCAO with the final set of parameters (black); (b) Overlap matrix elements; and (c) Hamiltonian matrix elements for Phosphorus.

The fitted structural properties and the energies of small P clusters are listed in Table 13, in which the 1st column shows the number of atoms; the 2nd column shows the structure; and the 3rd column gives the symmetry. The coordination of P elements in each cluster are

also inserted in the 2nd column, and the corresponding DFT and SCED data for both the geometric parameters and cohesive energies are listed in the 4th and 5th columns, respectively. All the properties obtained from the SCED-LCAO Hamiltonian are consistent with those from the DFT.

Table 13. Structural properties and cohesive energies of small P clusters calculated by the developed SCED-LCAO Hamiltonian for phosphorus and compared to those from DFT results.

#	Cluster	Symmetry	B3LYP/aug-cc-pvtz	SCED-LCAO
2		D_{ih}	a = 0.974 Å -0.141655 eV	a = 0.942 Å -0.085362 eV
3		D_{ih}	a = 1.964 Å -0.122633 eV	a = 2.001 Å -0.089223 eV
3		C_{2v}	a =1.017 Å b =1.955 Å -0.139649 eV	a =1.080 Å b =1.871 Å -0.098683 eV
4		C_{2v}	a_1 =1.944 Å b = 1.904 Å a_2 =1.050 Å -0.131093 eV	a_1 =1.944 Å b = 1.840 Å a_2 =1.060 Å -0.101913 eV
4		D_{2h}	b = 1.162 Å a = 1.026 Å -0.138010 eV	b = 1.157 Å a = 1.069 Å -0.102101 eV
4		D_{2hr}	a = 1.729 Å b = 1.224 Å -0.128496 eV	a = 1.793 Å b = 1.092 Å -0.101925 eV

4	(a, a, a)	T_d	a = 0.783 Å -0.16108 eV	a = 0.751 Å -0.123721 eV
5	$(\frac{\sqrt{3}}{2}a, 0, \frac{1}{2}a)$ (0, -b, 0)	D_{3h}	b = 1.079 Å a = 1.929 Å -0.135335	b = 1.039 Å a = 1.861 Å -0.110757 eV
5	(a, 0, 0) (0, 0, c)	C_{4v}	c = 1.660 Å a = 1.599 Å -0.145682 eV	c = 1.546 Å a = 1.542 Å -0.118619 eV
5	(0, b, 0) (a, 0, c_1) (0, 0, c_2)	C_{2vd}	a = 1.095 Å b = 1.482 Å c_1 = 1.325 Å c_2 = 1.672 Å -0.151333 eV	a = 1.063 Å b = 1.089 Å c_1 = 1.472 Å c_2 = 1.875 Å -0.118414 eV
6	(0, b_2, 0) (a_1, b_1, 0) (-a_2, 0, c)	C_{2v}	b_1 = 1.010 Å b_2 = 1.620 Å a_1 = 2.182 Å a_2 = 1.080 Å c = 1.111 Å -0.152801eV	b_1 = 1.072 Å b_2 = 1.564 Å a_1 = 2.207 Å a_2 = 1.122 Å c = 1.056 Å -0.120519 eV
7	(0, b_1, 0) (-a_2, b_2, c) (a_1, 0, 0)	C_{2v}	b_1 = 1.727Å b_2 = 1.165 Å a_1 = 1.340Å a_2 = 1.821 Å c = 1.128 Å -0.153358 eV	b_1 = 1.724Å b_2 = 1.135 Å a_1 = 1.426Å a_2 = 1.796 Å c = 1.087 Å -0.124780 eV
8	(0, b_1, c_1) (a_1, b_2, 0) (-a_2, 0, c_2)	C_{2v}	b_1 = 1.162 Å b_2 = 1.115 Å c_2 =1.120 Å c_1 = 1.802 Å a_1 = 1.760 Å a_2 = 1.383 Å -0.156756 eV	b_1 = 1.090 Å b_2 = 1.127 Å c_2 =1.126 Å c_1 = 1.806 Å a_1 = 1.769 Å a_2 = 1.347 Å -0.130258 eV
10	(a_2, b_2, 0) (a_1, 0, (-a_3, 0, c_3) (0, -b_1, -c_2)	C_{2v}	b_2 = 1.629 Å b_1 = 1.114 Å a_3 = 1.994 Å a_2 = 1.721 Å a_1 = 3.215 Å c_3 = 1.513 Å c_1 = 0.357 Å c_2 = 1.334 Å -0.158980 eV	b_2 = 1.580 Å b_1 = 1.122 Å a_3 = 2.106 Å a_2 = 1.757 Å a_1 = 3.239 Å c_3 = 1.482 Å c_1 = 0.299 Å c_2 = 1.310 Å -0.129272 eV

Robust tests for the intermediate P clusters are shown in Figure 5.9. They are all stable. Among them, the cluster P_{16} is the most stable one, followed by P_{24} and P_{12}. The energy order is consistent with the DFT results indicating the good transferability of the final set parameters.
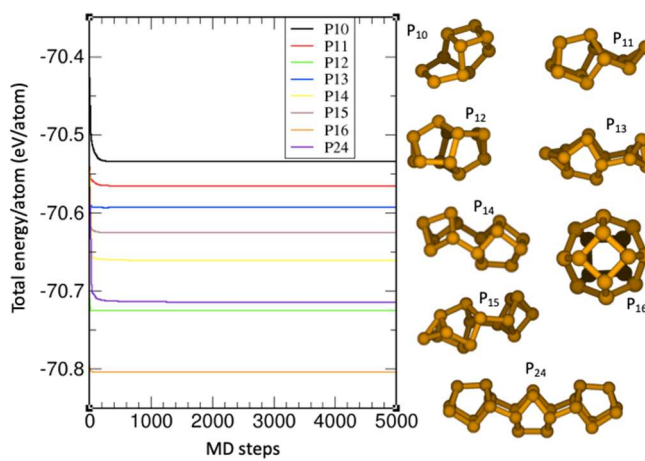
Figure 5.9 The total energy per atom as the function of MD step (left) for clusters with number of P atoms range from 10 to 24 (right).

The robust test of the black phosphorus, black phosphorene, and blue phosphorene are shown in Figure 5.10. The final structures are inserted at the end of each energy curve, clearly shown their structural stabilities. The energy order, namely, the energetics is consistent with DFT results (i.e., the black phosphorus is the most stable one and both black and blue phosphorene are energetically very close with energy difference less than 2 meV). The energy band gap of the black phosphorus is 0.32 eV; the black phosphorene is 1.32 eV; and the blue phosphorene is 2.16 eV, which are all consistent with the experimental or theoretical results [64-66] [154].
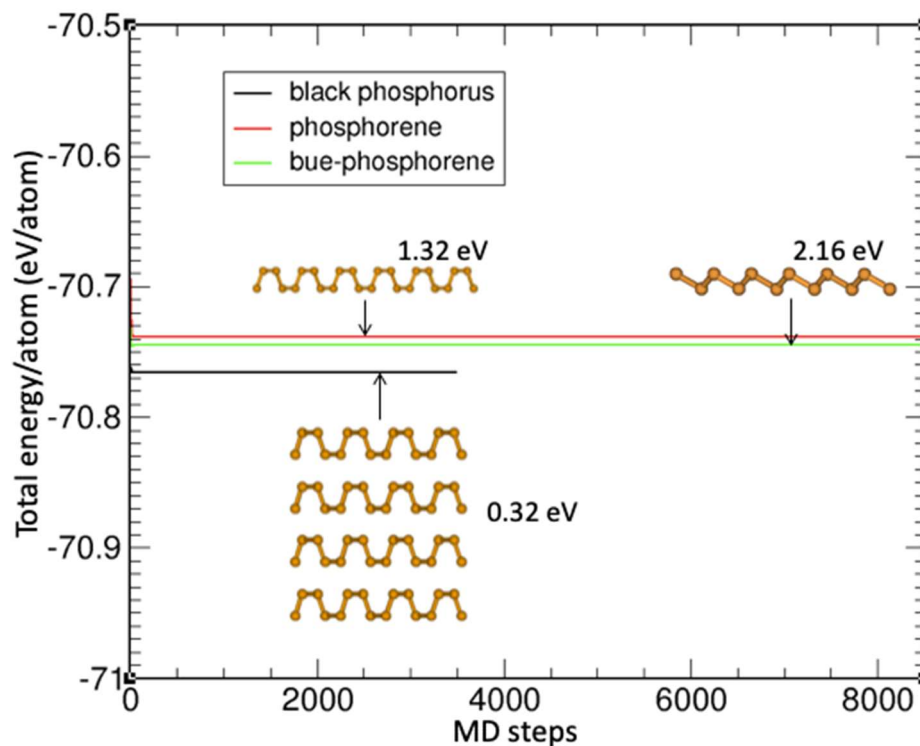
Figure 5.10 The total energies of the black phosphorus, black phosphorene, and blue phosphorene as functions of MD steps (based on the final set of parameters). The insets are corresponding final stabilized structures associated with their band gaps.

The fitted band structure of black phosphorus is shown in Figure 5.11 together with the band structure calculated by the GGA-PAW-PBE method. The energy gap gained by the SCED (Figure 5.11 (b)) with the final set of parameters is about 0.012 hartree, which is about 0.32 eV, very close to that of the VASP result. In particular, the indirect band gap nature calculated using the previous set of the parameters disappeared, and instead, the direct band gap feature is represented by the final set of parameters at the Γ point. Such features maintain during the relaxation process (see Figure 5.9) even after 3500 MD steps. All the robust tests demonstrated that the developed SCED-LCAO Hamiltonian for phosphorus is reliable, transferable. Interesting, the blue phosphorene has been predicted

to be energetically stable even after 8000 MD step, and predicted band gap is 2.0 eV, in agreement with the DFT results. Note that no any properties about the blue phosphorene incorporated in our database, that reveals the predict power of the SCED-LCAO Hamiltonian.
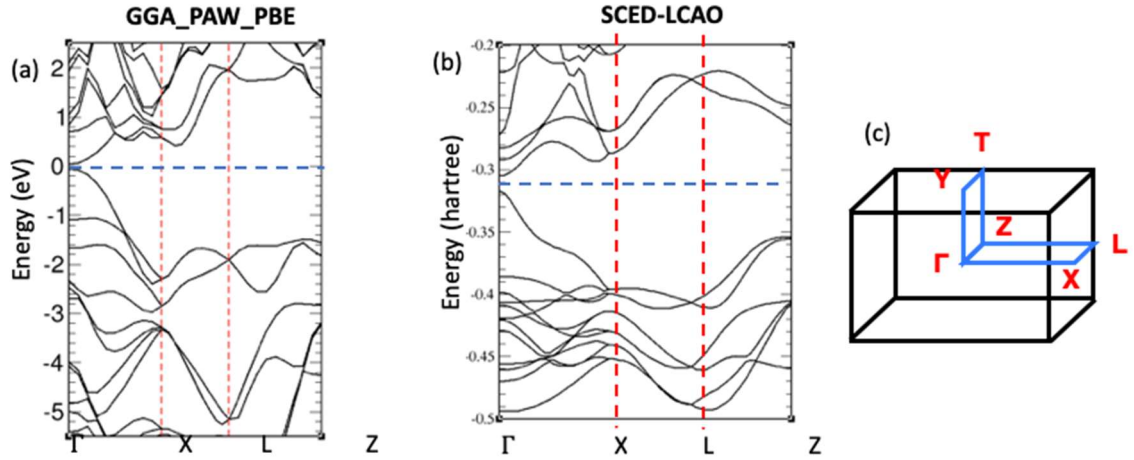
Figure 5.11 (a) Band structure of the black phosphorus calculated with DFT, (b) SCED-LCAO with the final set of parameters, (c) the first Brillouin zone with special k points.

5.2   Development of Lithium SCED-LCAO parameters

5.2.1   The initial database of lithium and the preliminary results

The database of Lithium was built by the former visitor doctoral study (Dr. Qi Dong) [214] using the *ab*-initial calculations. The phase diagram of the body-center-cubic (BCC) Li bulk calculated using the DFT method and Li clusters with the number of Li atoms up to 7 calculated by B3LYP/aug-cc-pvtz were included in the database (as shown in the left of Figure 5.12). The phase diagram of BCC Lithium is demonstrated in the right of Figure 5.12, where the back-dash curve represents the DFT (LDA-US) results for the relative energy with respect to the minimal value and the red solid curve is the SCED results using

the original database. The inset is the structure of BCC Li bulk with the lattice constant a = 3.50 Å.

It is found that during the robust check, we cannot find any stable clusters with the intermediate size and the stable structure of the BCC Li bulk with the SCED-LCAO Hamiltonian for Li suing the initial set of parameters. By carefully checking the database, we found that the geometric properties of some Li clusters need to be corrected (e.g., Li_4 with D_{ih} symmetry), and additional Li clusters with different symmetry (e.g., Li_6 with D_{4h} symmetry) which can capture the chemical bonding nature for larger Li clusters must be included in the database. On the other hand, the phase diagram also needed to be improved by expanding the range of volume per atom and making the curve from asymmetric (from 18.5 Å³/atom to 21.2 Å³/atom) to symmetric so as to cover bulk structure information as possible as we can.
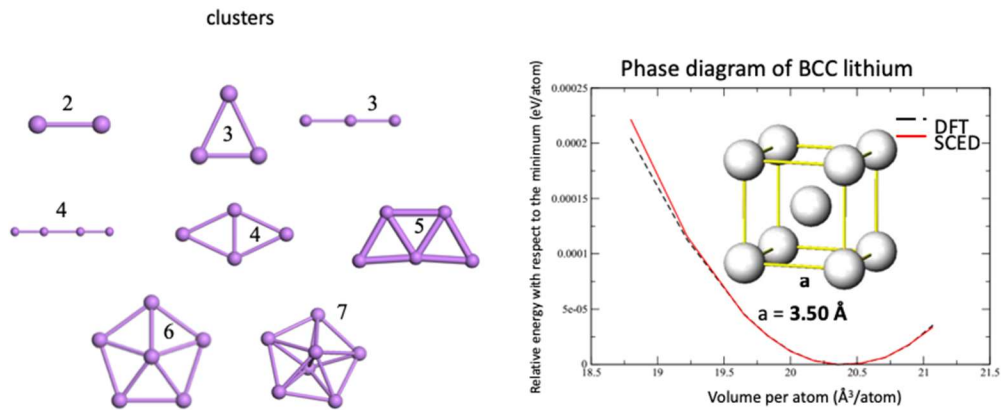
Figure 5.12 The Li clusters and bulk phase of BCC in the initial database. The number of Li atoms of each cluster and the structure of BCC are inserted. The black dashed curve is the DFT results and the red curve is the SCED-LCAO results using the initial set of parameters.

5.2.1 Improving database and reconstructing SCED-LCAO Hamiltonian parameters for Li

Based on the improved database, we obtained a new set of optimized parameters, as listed in Table 14. The updated bulk phase diagrams of BCC Lithium is shown in Figure 5.13, where the red curve is the VASP results which were obtained by GGA-PAW-PBE method, and the black curve is the SCED-LCAO results obtained during the fitting process. By comparing with the phase diagram of BCC Li bulk in Figure 5.12, the fitting range is extended from 18.5 Å³/atom to 22.1 Å³/atom, and the SCED-LCAO results agree with the DFT results very well in the whole range.

Table 14. The new set of optimized SCED-LCAO Hamiltonian parameters.

Hamiltonian parameters	values	Hamiltonian parameters	Values
$\varepsilon_s(eV)$	-5.3400000	$U(eV)$	6.94172789
$\varepsilon_p(eV)$	-2.2163000	$\alpha_K(\text{Å}^{-1})$	0.15581250
$\varepsilon_s'(eV)$	-5.61611966	$A_N(eV)$	-1.83887989
$\varepsilon_p'(eV)$	-2.55093076	$B_N(\text{Å}^{-1})$	0.36862439
$W_p^0(eV)$	-0.60538501	$\alpha_N(\text{Å}^{-1})$	1.79092745
$W_s^0(eV)$	-0.10567223	$d_N(\text{Å})$	4.10274521
$\alpha_{p,w}(\text{Å}^{-1})$	0.68922883	$B_z(\text{Å}^{-1})$	0.39618191
$\alpha_{s,w}(\text{Å}^{-1})$	2.72418593		
$\alpha_{pp\pi}(\text{Å}^{-1})$	3.39842371	$B_{sp\sigma}(\text{Å}^{-1})$	0.51206904
$\alpha_{pp\sigma}(\text{Å}^{-1})$	1.20244907	$B_{ss\sigma}(\text{Å}^{-1})$	-0.29070798
$\alpha_{sp\sigma}(\text{Å}^{-1})$	1.47657116	$d_{pp\pi}(\text{Å})$	0.64482077
$\alpha_{ss\sigma}(\text{Å}^{-1})$	1.18006153	$d_{pp\sigma}(\text{Å})$	0.42285255
$B_{pp\pi}(\text{Å}^{-1})$	0.48273810	$d_{sp\sigma}(\text{Å})$	1.31856917
$B_{pp\sigma}(\text{Å}^{-1})$	0.51028689	$d_{ss\sigma}(\text{Å})$	2.02666329
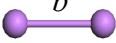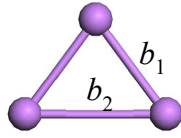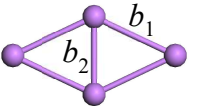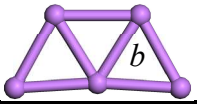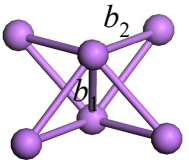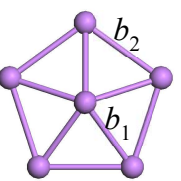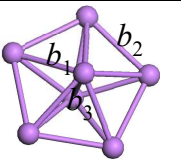
Figure 5.13 The updated phase diagram of BCC Lithium. The black curve is the DFT results and the red one, the SCED-LCAO results.

The fitted structural properties and the cohesive energies of small P clusters are listed in Table 15, where the 1st column shows the structure with the different type of bonds; the 2nd column gives the symmetry of each cluster; the 3rd indicates the properties, 4th column lists energies and the bond lengths obtained from the SCED-LCAO calculations; and the 5th columns lists the energies and bond lengths calculated by B3LYP/aug-cc-pvtz method.

Table 15. Geometric properties and cohesive energies of Lithium clusters calculated with DFT and SCED-LCAO Hamiltonian using the new set of parameters.

Li clusters			SCED-LCAO	B3LYP/aug-cc-pvtz
Structure	Symmetry	properties		
b	D_{ih}	$E_{relative}$ (eV/atom)	-0.01731262	-0.01665195
		Bond length (Å)	$b = 2.66$	$b = 2.70$
b_1 b_2	C_{2v}	$E_{relative}$ (eV/atom)	-0.01899015	-0.01773523
		Bond length (Å)	$b_1 = 2.826$ $b_2 = 3.312$	$b_1 = 2.751$ $b_2 = 3.288$
	D_{2h}	$E_{relative}$ (eV/atom)	-0.02469745	-0.0234315

126

		Bond length (Å)	$b_1 = 2.945$ $b_2 = 2.816$	$b_1 = 3.006$ $b_2 = 2.574$
	C_{2v}	$E_{relative}$ (eV/atom)	-0.02738217	-0.0246655
		Bond length (Å)	$b = 2.997$	$b = 2.972$
	D_{4h}	$E_{relative}$ (eV/atom)	-0.02776673	-0.02827007
		Bond length (Å)	$b_1 = 2.945$ $b_2 = 2.567$	$b_1 = 2.7945$ $b_2 = 2.5264$
	C_{5v}	$E_{relative}$ (eV/atom)	-0.0281046	-0.0273865
		Bond length (Å)	$b_1 = 2.873$ $b_2 = 3.026$	$b_1 = 2.788$ $b_2 = 3.148$
	D_{5h}	$E_{relative}$ (eV/atom)	-0.03192699	-0.0305371
		Bond length (Å)	$b_1 = 2.655$ $b_2 = 3.001$ $b_3 = 2.984$	$b_1 = 2.905$ $b_2 = 3.018$ $b_3 = 2.718$

The Hamiltonian and Overlap matrix elements as a function of the atomic distance obtained using the new set of are demonstrated in Figure 5.14. The black curves in both overlap and Hamiltonian matrix correspond to the orbital of $ss\sigma$; red curves correspond to the orbital of $sp\sigma$; green curves correspond to the orbital of $ps\sigma$; blue curves correspond to the orbital of $pp\sigma$; and yellow curves correspond to the orbital of $pp\pi$, respectively. The five orbitals are all normalized, so they cannot exceed unity. On the other hand, both the overlap curves and Hamiltonian curves decay to zero within a cutoff of 7 Å.
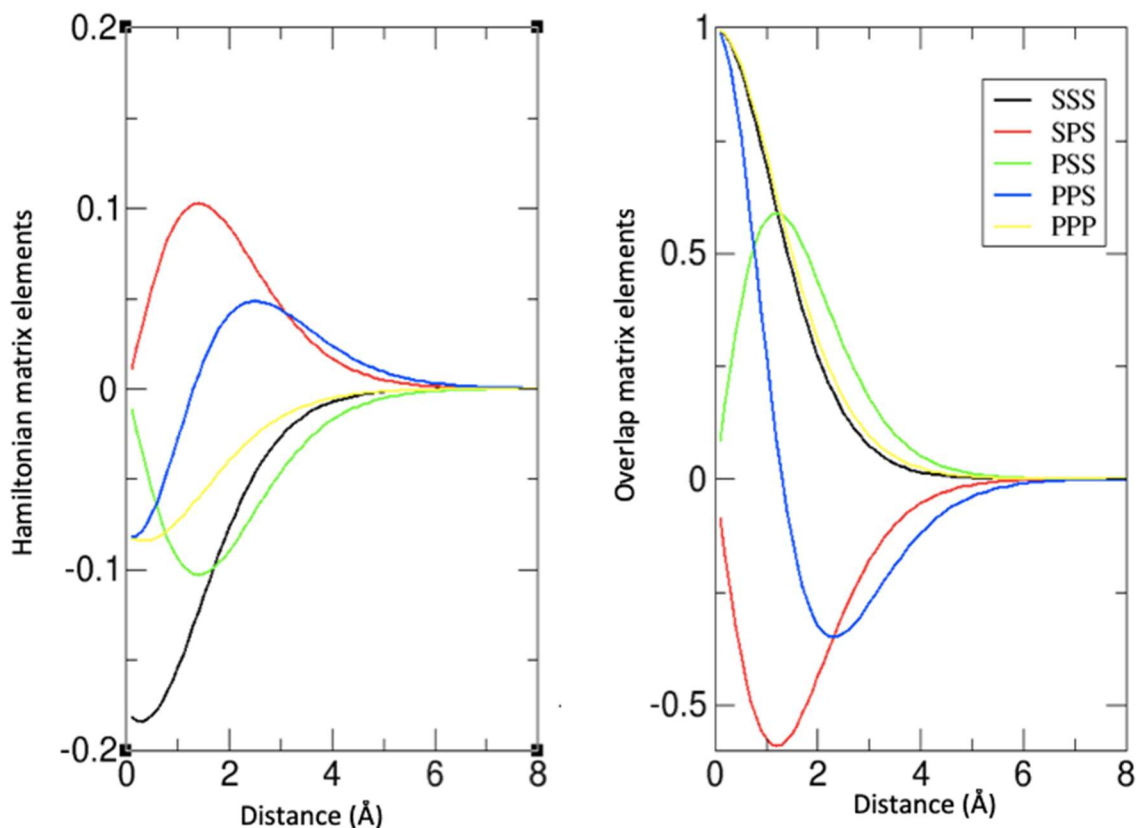
Figure 5.14 Hamiltonian (in Hartree unit) and overlap matrix elements as a function of the atomic distance based on the new set of parameters. Here the notation SSS indicates $ss\sigma$; SPS indicates $sp\sigma$; PSS indicates $ps\sigma$; PPS indicates $pp\sigma$; and PPP indicates $pp\pi$, respectively.

A robust test with the new set of SCED-LCAO Hamiltonian for Li was performed for the BCC Li bulk. The total energy per atom as the function of MD step is shown in Figure 5.15. A stabilized BCC bulk was found during the MD relaxation process even after at 3000th step, demonstrating the significant improvement in the SCED-LCAO Hamiltonian parameters for Li and the importance of the choice of the database. To further develop the SCED-LCAO Hamiltonian for Li, we will carry out additional robust tests focusing on the large Li clusters, the electronic properties of Li BCC bulk, and the Li-P compounds. The

goal is to apply the developed SCED-LCAO Hamiltonian for phosphorus and lithium to study the Li capacity in the phosphorene-graphene layered heterostructure as the anode material.
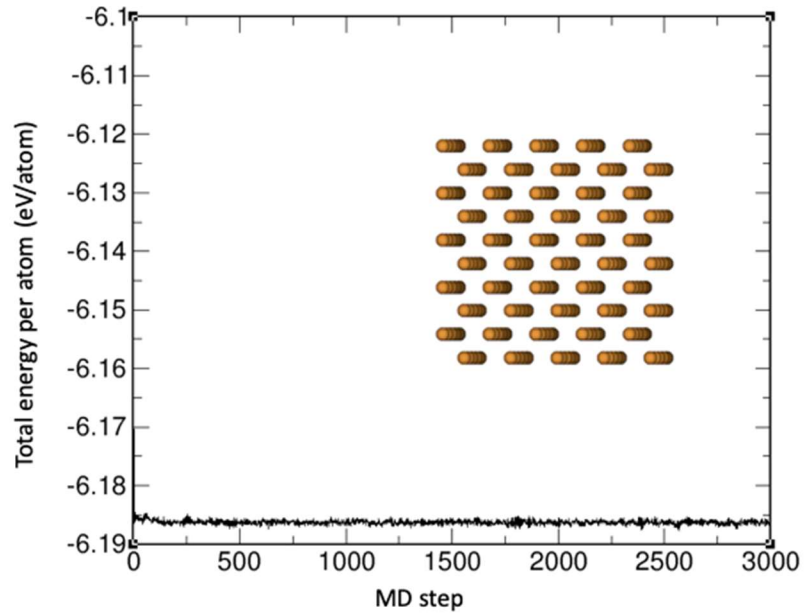
Figure 5.15 The total energy of BCC Li as the function of MD steps (based on the new set of parameters. The stabilized structure is shown inset.

CHAPTER VI

FUTURE WORK

6.1 Li intercalation mediated phase transition from the black phosphorene to blue phosphorene

As we mentioned in this thesis, the newly discovered phosphorene has gained extensive attention, particularly for electronic and optoelectronic applications. Soon after, new 2D material, referred to as blue phosphorene, has been predicted to have even a wide fundamental band gap (>2 eV) compared to black phosphorene [15], tunable gap depending on the number of layers, semiconducting-semimetal transition under strain, possible high carrier mobility, and higher in-plane rigidity, which would become a worthy contender in the emerging field of post-graphene 2D electronics [15]. However, mechanically exfoliate blue phosphorene from its bulk counterpart is a big challenge since blue phosphorus can only exist at high pressure (>5GPa). It is, therefore, extremely desired if we can develop a new pathway to synthesize blue phosphorus at low pressures, or even under ambient conditions so that mechanical exfoliation become technically feasible.

It was suggested that a transition from black phosphorene to blue phosphorene could happen under specific dislocations by flipping specific P atoms from a 'down' to an 'up' position (illustrated in Figure 6.1 (c)) [215]. Such atomistic mechanism provides us a hint

to find alternative pathways in synthesizing blue phosphorus. For instance, instead of using pressure, one might consider using foreign elements, such as Li, to induce the structural phase transition from black to blue phosphorus.
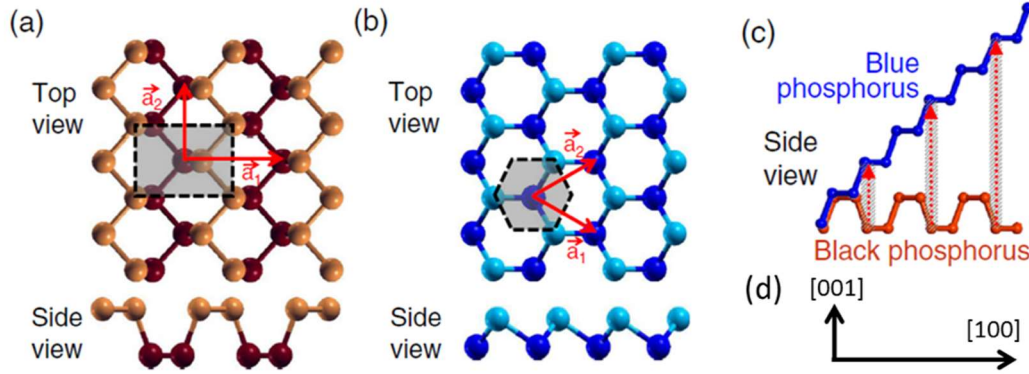
Figure 6.1 Top and side views of black (a) and blue (b) phosphorus monolayer. Atoms at the top and bottom of nonplanar layers are distinguished by color and shading, the Wigner-Seitz cells are shown by the shaded region, and lattice vectors are denoted by arrows. (c) Schematic of the conversion of black to blue phosphorus by dislocations. (d) Orientations along [001] and [100] directions.

As discussed in chapter 4, we performed a throughout investigation on the Li intercalation on black phosphorene in studying the prospects of phosphorene as an anode material for high performance Li-ion battery [216]. On the other hand, when a certain Li atoms (e.g., x ~ 0.625) were inserted unsymmetrically in the layered black phosphorene (see Figure 6.2 (a) and (b)), during the relaxation process, the bonds connecting P atoms at the valley and the ridge on the same layer broke and subsequently, new P-P bonds between adjacent layers formed (see Figure 6.2 (c)). As the results, the puckered orthorhombic structure was automatically transformed to a buckled rhombohedral structure. After Li removal, the system was automatically stabilized to the layered blue phosphorene (see

Figure 6.2 (d)), indicating that the inserted Li atoms could act as 'catalysts' to drive the specific P atoms moving along specific directions, resulting bond breaking and forming, and subsequently, transforming layered black to layered blue phosphorus. This preliminary study opened us a new pathway that, at a certain high rate Li intercalation, a feasible transition path from layered black phosphorus to layered blue phosphorus without pressure is possible.
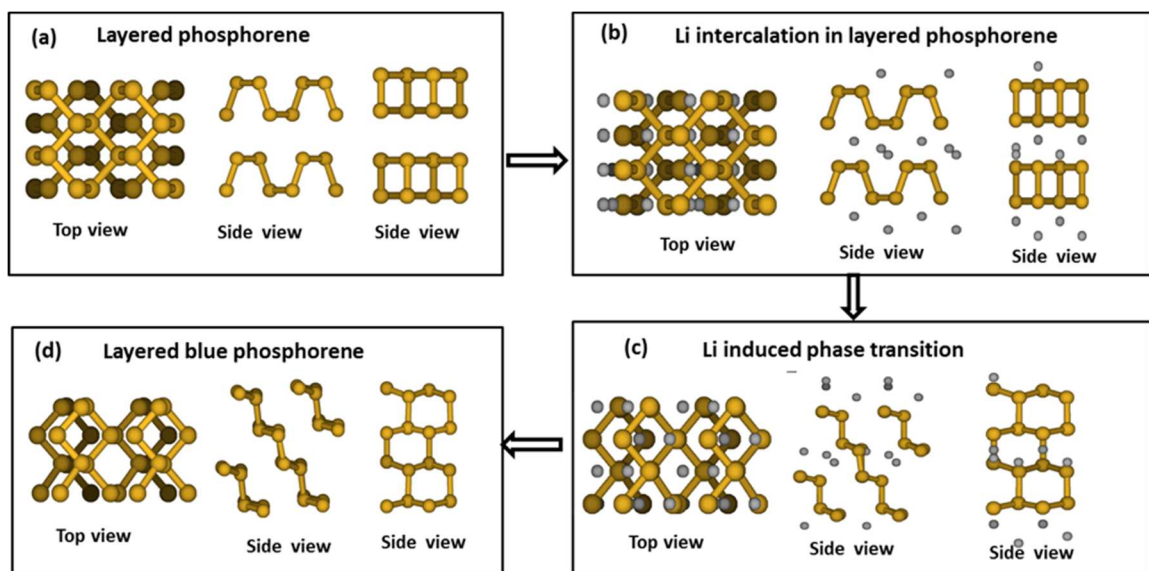
Figure 6.2 Top and side views of (a) layered black phosphorene; (b) Li intercalation in the layered black phosphorene; (c) Li induced structural phase transition during the relaxation; and (d) layered blue phosphorene after Li removal, respectively. The arrows show the direction of the flow of the transition induced by the Li intercalation.

Prompted by our preliminary study, we propose to develop a new pathway to synthesize blue phosphorus from black phosphorus by means of Li interaction under ambient condition, and subsequently, providing a new guideline for producing blue phosphorene using mechanical exfoliation. To accomplish this initiated research and then,

to provide a fundamental guideline for accelerating the discovery of this new material, we plan to perform a systematic investigation through computational modeling to address the role played by the Li intercalation during the structural transition, in particular, the atomistic mechanism of whether the specific dislocations of P atoms in black phosphorus can be mediated by the attractions between Li and P atoms.

6.2   Vibration frequencies of phosphorus under high pressure

As shown in Figure 6.3, the Raman spectra of few layer phosphorus shift under high pressure. It is found that the A_{1g} mode showed a linear increase, while the B_{2g} mode initially increases linearly and then saturates above 2 GPa. The A_{2g} mode, on the other hand, does not show any significant pressure dependence. To shed light into it and figure out the reason of Raman shift under high pressure, we carried out theoretical simulation by using the GGA-PAW-PBE method.
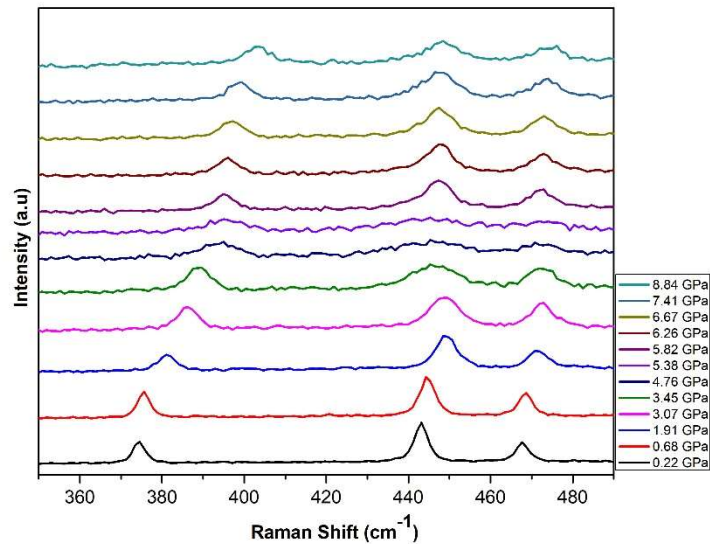
Figure 6.3 Raman spectra of a few-layer black phosphorus under pressure range of 0 GPa (bottom spectrum) to 12.56 GPa (top spectrum) with vertical displacements for clarity [217]

In the processes of investigating the vibration modes of black phosphorus under pressure, a uniform compression was introduced and a fully relaxation under each given compression was performed. The pressure is estimated by $P \approx \frac{\Delta E}{A \Delta b}$. The vibration modes at Γ point were calculated from Hessian matrix implemented in VASP code. There are nine vibration modes (B_{2u}, A_{2g}, B_{2g}, A_u, $B_{3g(2)}$, A_{1g}, $B_{3g(1)}$, B_{1g}, B_{1u}) and only six are Raman-active modes (A_{2g}, B_{2g}, $B_{3g(2)}$, A_{1g}, $B_{3g(1)}$, B_{1g}). Typical measured Raman spectrum of an exfoliated black phosorus are A_{2g}, B_{2g}, and A_{1g}, respectively.
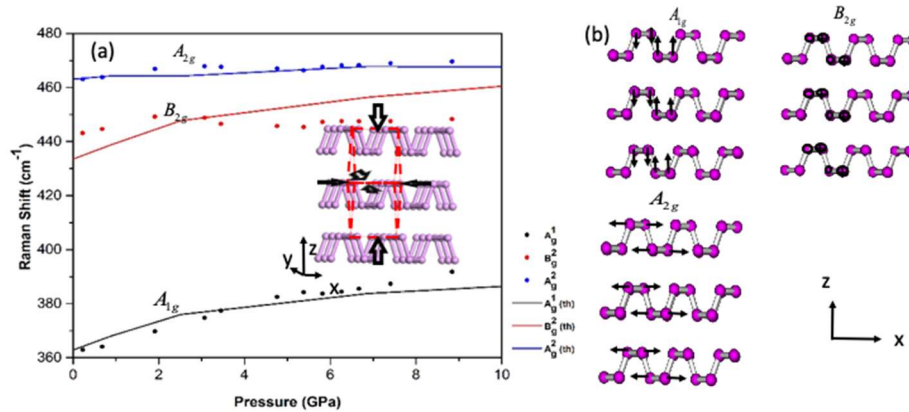
Figure 6.4 (a) The calculated (solid lines) and experimental measurement (dots) of vibration frequencies as the function of the estimated pressure, the compression of black phosphorus is inserted. (b) The schematic illustration of the three atomic motions of lattice vibrational modes.

Calculated vibration frequencies at Γ point for the vibration modes A_{2g}, B_{2g}, and A_{1g} under high pressure are shown in Figure 6.4 (a). The corresponding atomic motions of the

vibrational modes are demonstrated in Figure 6.4 (b). Very interesting finding is that both the out-plane vibration mode A_{1g} and the in-plane vibration mode B_{2g} along the zigzag direction increases linearly, while the in-plane vibration mode A_{2g} along the armchair direction show almost unchanged under the high pressure, in consistent with our experimental observations (see Figure 6.4 (a)).

In the next step, we are going to analyze the mechanism of the Raman shifts associated with the change of structure under high pressure. We are interested in the change of bond length and bond angle under the uniform compression. There are two type of bonds in black phosphorus, the horizontal bonds and the vertical bonds, the reduce of bond length along certain direction may lead to the change of interactions in the structure and, therefore, the shift of vibration modes.

6.3   Predicting the novel 2D BAs

Quite recently, the launch on synthesizing high quality single-crystal zinc-blend BAs with ultrahigh thermal conductivity at room temperature (1300 W(m.K)$^{-1}$) [76] marks a breakthrough in thermal materials and attracts extremely interesting. It is highly desired to seek new BAs family member, which would also possess such high thermal conductivity.
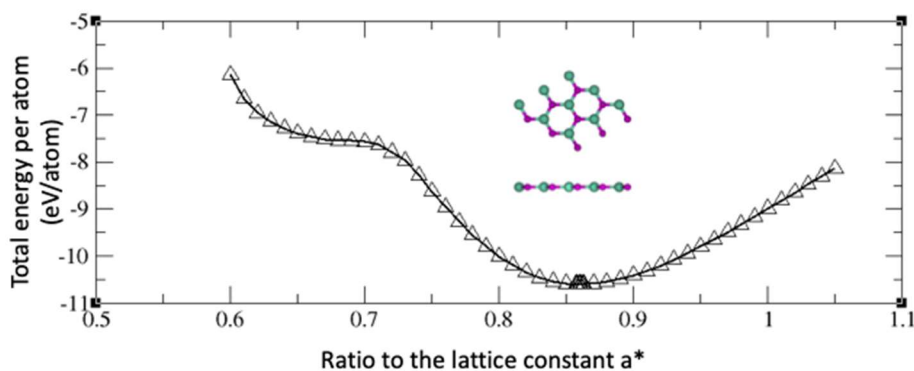
Figure 6.5 The total energy per atom of BAs monolayer as a function of the ratio to a*, where a*= 3.946 Å. The insert is the energetically stable BAs flat layer.

Similar to the way we get the initial configuration of GaP and InP in Figure 3.1, the initial configurations of BAs layer were constructed by the zigzag and the armchair truncation from the BAs zinc blende bulk. The structural optimizations were conducted for these two initial configurations. In the case of the zigzag truncation, by scaling the lattice constant and buckling parameters, we found that the low buckled honeycomb structure does not exist since there is no energy minimum (see Figure 6.5) and a minimum was found for the flat honeycomb BAs sheet with the optimized lattice constant of 3.393 Å (see Figure 6.5), indicating the existence of the flat BAs, consistence with the previous theoretical results [12]. In the case of the armchair truncation, a new sandwiched 2D BAs binary compound with anisotropic structure was found, similar as what we found for sandwiched 2D phosphide binary compounds. The optimized lattice constants for such BAs layer structure are a = 3.451 Å and c = 4.822 Å, respectively. The two stable structure are shown in Figure 6.6. More interestingly, different from the GaP and InP layers which the high puckered layer is the most stable one, the total energy per atom of the flat layer is -10.600 eV/atom, which is about 0.3 eV lower than that of the high puckered layer.

High puckered layer   Flat layer
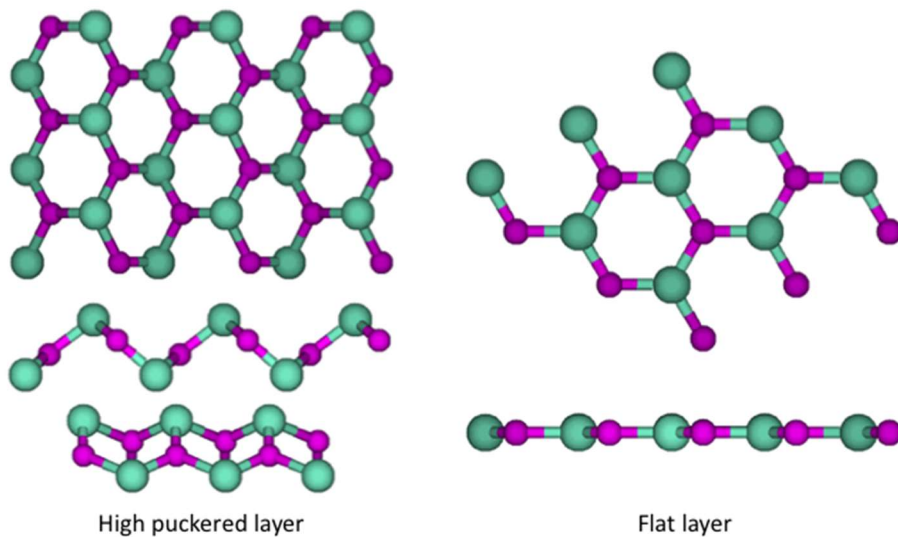
Figure 6.6 Newly discovered 2D BAs structures: flat layer (right) and high puckered layer (left).

In the next step, we would analysis the electronic properties of the stable BAs layers, and then study the mechanical properties by extend the structure along certain direction. Furthermore, more stable binary compound from group III-V need to be studied to catch the rule of forming stable 2D layers from group III-V.

REFERENCES

1. Peierls, R., *Quelques propriétés typiques des corps solides.* Annales de l'institut Henri Poincaré, 1935. **5**(3): p. 177-222.

2. Landau, L.D., *Zur Theorie der phasenumwandlungen II.* Phys. Z. Sowjetunion, 1937. **11**(545): p. 26-35.

3. Geim, A.K. and K.S. Novoselov, *The rise of graphene.* Nature Materials, 2007. **6**: p. 183.

4. Mermin, N.D., *Crystalline Order in Two Dimensions.* Physical Review, 1968. **176**(1): p. 250-254.

5. Venables, J.A., G.D.T. Spiller, and M. Hanbucken, *Nucleation and growth of thin films.* Reports on Progress in Physics, 1984. **47**(4): p. 399.

6. Novoselov, K.S., et al., *Electric Field Effect in Atomically Thin Carbon Films.* Science, 2004. **306**(5696): p. 666.

7. Topsakal, M., E. Aktürk, and S. Ciraci, *First-principles study of two- and one-dimensional honeycomb structures of boron nitride.* Physical Review B, 2009. **79**(11): p. 115442.

8. Zhi, C., et al., *Large-Scale Fabrication of Boron Nitride Nanosheets and Their Utilization in Polymeric Composites with Improved Thermal and Mechanical Properties*. Vol. 21. 2009. 2889-2893.

9.   Yu, M., C.S. Jayanthi, and S.Y. Wu, *Geometric and electronic structures of graphitic-like and tubular silicon carbides: Ab-initio studies.* Physical Review B, 2010. **82**(7): p. 075407.

10.   Cahangirov, S., et al., *Two- and One-Dimensional Honeycomb Structures of Silicon and Germanium.* Physical Review Letters, 2009. **102**(23): p. 236804.

11.   Gu, X. and R. Yang, *First-principles prediction of phononic thermal conductivity of silicene: A comparison with graphene.* Journal of Applied Physics, 2015. **117**(2): p. 025102.

12.   Şahin, H., et al., *Monolayer honeycomb structures of group-IV elements and III-V binary compounds: First-principles calculations.* Physical Review B, 2009. **80**(15): p. 155453.

13.   Lalmi, B., et al., *Epitaxial growth of a silicene sheet.* Applied Physics Letters, 2010. **97**(22): p. 223109.

14.   Leandri, C., et al., *Growth of Si nanostructures on Ag(001).* Surface Science, 2007. **601**(1): p. 262-267.

15.   Aufray, B., et al., *Graphene-like silicon nanoribbons on Ag(110): A possible formation of silicene.* Applied Physics Letters, 2010. **96**(18): p. 183102.

16.   De Padova, P., et al., *sp2-like hybridization of silicon valence orbitals in silicene nanoribbons.* Applied Physics Letters, 2011. **98**(8): p. 081909.

17.   Rachid Tchalala, M., et al., *Formation of one-dimensional self-assembled silicon nanoribbons on Au(110)-(2 × 1).* Applied Physics Letters, 2013. **102**(8): p. 083107.

18.   Feng, B., et al., *Evidence of Silicene in Honeycomb Structures of Silicon on Ag(111).* Nano Letters, 2012. **12**(7): p. 3507-3511.

19. Lebègue, S. and O. Eriksson, *Electronic structure of two-dimensional crystals from ab initio theory.* Physical Review B, 2009. **79**(11): p. 115409.

20. Liu, C.-C., W. Feng, and Y. Yao, *Quantum Spin Hall Effect in Silicene and Two-Dimensional Germanium.* Physical Review Letters, 2011. **107**(7): p. 076802.

21. Roome, N.J. and J.D. Carey, *Beyond Graphene: Stable Elemental Monolayers of Silicene and Germanene.* ACS Applied Materials & Interfaces, 2014. **6**(10): p. 7743-7750.

22. Vogt, P., et al., *Silicene: Compelling Experimental Evidence for Graphenelike Two-Dimensional Silicon.* Physical Review Letters, 2012. **108**(15): p. 155501.

23. Chun-Liang, L., et al., *Structure of Silicene Grown on Ag(111).* Applied Physics Express, 2012. **5**(4): p. 045802.

24. Sheng-shi, L., et al., *Novel band structures in silicene on monolayer zinc sulfide substrate.* Journal of Physics: Condensed Matter, 2014. **26**(39): p. 395003.

25. Gao, J. and J. Zhao, *Initial geometries, interaction mechanism and high stability of silicene on Ag(111) surface.* Scientific Reports, 2012. **2**: p. 861.

26. Fleurence, A., et al., *Experimental Evidence for Epitaxial Silicene on Diboride Thin Films.* Physical Review Letters, 2012. **108**(24): p. 245501.

27. Yang, H., et al., *Structural and quantum-state phase transition in van der Waals layered materials*. Vol. 13. 2017.

28. Yamamoto, M., et al., *Strong Enhancement of Raman Scattering from a Bulk-Inactive Vibrational Mode in Few-Layer MoTe2.* ACS Nano, 2014. **8**(4): p. 3895-3903.

29. Horzum, S., et al., *Phonon softening and direct to indirect band gap crossover in strained single-layer MoSe${}_{2}$.* Physical Review B, 2013. **87**(12): p. 125415.

30. Bertolazzi, S., J. Brivio, and A. Kis, *Stretching and Breaking of Ultrathin MoS2.* ACS Nano, 2011. **5**(12): p. 9703-9709.

31. Wang, Q.H., et al., *Electronics and optoelectronics of two-dimensional transition metal dichalcogenides.* Nature Nanotechnology, 2012. **7**: p. 699.

32. Bjorkman, T., et al., *van der Waals Bonding in Layered Compounds from Advanced Density-Functional First-Principles Calculations.* Physical Review Letters, 2012. **108**(23).

33. Bernardi, M., M. Palummo, and J.C. Grossman, *Extraordinary Sunlight Absorption and One Nanometer Thick Photovoltaics Using Two-Dimensional Monolayer Materials.* Nano Letters, 2013. **13**(8): p. 3664-3670.

34. Naguib, M., et al., *Two-Dimensional Nanocrystals Produced by Exfoliation of Ti3AlC2.* Advanced Materials, 2011. **23**(37): p. 4248-4253.

35. Yang, F., et al., *Scalable synthesis of two-dimensional antimony telluride nanoplates down to a single quintuple layer.* RSC Advances, 2015. **5**(73): p. 59320-59325.

36. Ferrari, A.C., et al., *Science and technology roadmap for graphene, related two-dimensional crystals, and hybrid systems.* Nanoscale, 2015. **7**(11): p. 4598-4810.

37. Gupta, A., T. Sakthivel, and S. Seal, *Recent development in 2D materials beyond graphene.* Progress in Materials Science, 2015. **73**: p. 44-126.

38. Kim, H., et al., *All-graphene-battery: bridging the gap between supercapacitors and lithium ion batteries.* Scientific Reports, 2014. **4**: p. 5278.

39. Neumark, G.F., *Defects in wide band gap II-VI crystals.* Materials Science and Engineering: R: Reports, 1997. **21**(1): p. iii-46.

40. Björkman, T., et al., *van der Waals Bonding in Layered Compounds from Advanced Density-Functional First-Principles Calculations.* Physical Review Letters, 2012. **108**(23): p. 235502.

41. Lu, W., et al., *Plasma-assisted fabrication of monolayer phosphorene and its Raman characterization.* Nano Research, 2014. **7**(6): p. 853-859.

42. Liu, H., et al., *Phosphorene: An Unexplored 2D Semiconductor with a High Hole Mobility.* ACS Nano, 2014. **8**(4): p. 4033-4041.

43. Hohenberg, P. and W. Kohn, *Inhomogeneous Electron Gas.* Physical Review, 1964. **136**(3B): p. B864-B871.

44. Kohn, W. and L.J. Sham, *Self-Consistent Equations Including Exchange and Correlation Effects.* Physical Review, 1965. **140**(4A): p. A1133-A1138.

45. Alder, B.J. and T.E. Wainwright, *Studies in Molecular Dynamics. I. General Method.* The Journal of Chemical Physics, 1959. **31**(2): p. 459-466.

46. Rahman, A., *Correlations in the Motion of Atoms in Liquid Argon.* Physical Review, 1964. **136**(2A): p. A405-A411.

47. Binder, K., *The Monte Carlo Method in Condensed Matter Physics.* Springer, 1995. **New York, NY, USA**.

48. Chen, L.-Q., *Phase-Field Models for Microstructure Evolution.* Annual Review of Materials Research, 2002. **32**(1): p. 113-140.

49. Ingo, S., *Phase-field models in materials science.* Modelling and Simulation in Materials Science and Engineering, 2009. **17**(7): p. 073001.

50. W. J. Boettinger, et al., *Phase-Field Simulation of Solidification.* Annual Review of Materials Research, 2002. **32**(1): p. 163-194.

51. *Materials Genome Initiative for Global Competitiveness.* 2011.

52. Chen, L.-Q., et al., *Design and discovery of materials guided by theory and computation.* Npj Computational Materials, 2015. **1**: p. 15007.

53. Tang, H. and S. Ismail-Beigi, *First-principles study of boron sheets and nanotubes.* Physical Review B, 2010. **82**(11): p. 115412.

54. Tang, H. and S. Ismail-Beigi, *Novel Precursors for Boron Nanotubes: The Competition of Two-Center and Three-Center Bonding in Boron Sheets.* Physical Review Letters, 2007. **99**(11): p. 115501.

55. Wu, X., et al., *Two-Dimensional Boron Monolayer Sheets.* ACS Nano, 2012. **6**(8): p. 7443-7453.

56. Kah, C.B., et al., *Low-dimensional boron structures based on icosahedron B 12.* Nanotechnology, 2015. **26**(40): p. 405701.

57. Guzmán-Verri, G.G. and L.C. Lew Yan Voon, *Electronic structure of silicon-based nanostructures.* Physical Review B, 2007. **76**(7): p. 075131.

58. Chigo Anota, E. and G. Murrieta Hernández, *Electronic properties of germanium carbide blade of graphene type*. Vol. 57. 2011. 30-34.

59. Pan, L., et al., *First-principles study of monolayer and bilayer honeycomb structures of group-IV elements and their binary compounds*. Vol. 375. 2011. 614-619.

60. Feng, B., et al., *Experimental realization of two-dimensional boron sheets.* Nature Chemistry, 2016. **8**: p. 563.

61.   Feng, B., et al., *Direct evidence of metallic bands in a monolayer boron sheet.* Physical Review B, 2016. **94**(4): p. 041408.

62.   Feng, B., et al., *Dirac Fermions in Borophene.* Physical Review Letters, 2017. **118**(9): p. 096401.

63.   Mannix, A.J., et al., *Synthesis of borophenes: Anisotropic, two-dimensional boron polymorphs.* Science, 2015. **350**(6267): p. 1513.

64.   Lu, W.L., et al., *Plasma-assisted fabrication of monolayer phosphorene and its Raman characterization.* Nano Research, 2014. **7**(6): p. 853-859.

65.   Buscema, M., et al., *Fast and Broadband Photoresponse of Few-Layer Black Phosphorus Field-Effect Transistors.* Nano Letters, 2014. **14**(6): p. 3347-3352.

66.   Liu, H., et al., *Phosphorene: An Unexplored 2D Semiconductor with a High Hole Mobility.* ACS Nano, 2014. **8**(4): p. 4033-4041.

67.   Akhtar, M., et al., *Recent advances in synthesis, properties, and applications of phosphorene.* npj 2D Materials and Applications, 2017. **1**(1): p. 5.

68.   Fei, R. and L. Yang, *Strain-Engineering the Anisotropic Electrical Conductance of Few-Layer Black Phosphorus.* Nano Letters, 2014. **14**(5): p. 2884-2889.

69.   Wei, Q. and X. Peng, *Superior mechanical flexibility of phosphorene and few-layer black phosphorus.* Applied Physics Letters, 2014. **104**(25): p. 251915.

70.   Wang, L., et al., *Electro-mechanical anisotropy of phosphorene.* Nanoscale, 2015. **7**(21): p. 9746-9751.

71.   Ramireddy, T., et al., *Phosphorus–carbon nanocomposite anodes for lithium-ion and sodium-ion batteries.* Journal of Materials Chemistry A, 2015. **3**(10): p. 5572-5584.

72. Guo, G.-C., et al., *First-Principles Study of Phosphorene and Graphene Heterostructure as Anode Materials for Rechargeable Li Batteries.* The Journal of Physical Chemistry Letters, 2015. **6**(24): p. 5002-5008.

73. Leahy, C., et al., *Coherent treatment of the self-consistency and the environment-dependency in a semi-empirical Hamiltonian: Applications to bulk silicon, silicon surfaces, and silicon clusters*. Vol. 74. 2006.

74. Quan Tian, W., et al., *The Self-Consistent and Environment-Dependent Hamiltonian and Its Application to Carbon Nanoparticles*. Vol. 6. 2009. 390-396.

75. Yu, M., S.Y. Wu, and C.S. Jayanthi, *A self-consistent and environment-dependent Hamiltonian for large-scale simulations of complex nanostructures.* Physica E: Low-dimensional Systems and Nanostructures, 2009. **42**(1): p. 1-16.

76. Kang, J.S., et al., *Experimental observation of high thermal conductivity in boron arsenide.* Science, 2018.

77. Hehre, W.J., *Ab initio molecular orbital theory.* Accounts of Chemical Research, 1976. **9**(11): p. 399-406.

78. Møller, C. and M.S. Plesset, *Note on an Approximation Treatment for Many-Electron Systems.* Physical Review, 1934. **46**(7): p. 618-622.

79. Coester, F., *Bound states of a many-particle system.* Nuclear Physics, 1958. **7**: p. 421-424.

80. Kümmel, H., *Theory of many-body wave functions with correlations.* Nuclear Physics A, 1971. **176**(1): p. 205-218.

81.   Bakowies, D. and W. Thiel, *Hybrid Models for Combined Quantum Mechanical and Molecular Mechanical Approaches.* The Journal of Physical Chemistry, 1996. **100**(25): p. 10580-10594.

82.   Calais, J.L., *Density-functional theory of atoms and molecules. R.G. Parr and W. Yang, Oxford University Press, New York, Oxford, 1989. IX + 333 pp. Price £45.00.* International Journal of Quantum Chemistry, 2004. **47**(1): p. 101-101.

83.   Bowler, D.R., et al., *Recent progress with large-scale ab initio calculations: the CONQUEST code.* physica status solidi (b), 2006. **243**(5): p. 989-1000.

84.   Ozaki, T., *$O(N)$ Krylov-subspace method for large-scale ab initio electronic structure calculations.* Physical Review B, 2006. **74**(24): p. 245101.

85.   Majewski, J.A. and P. Vogl, *Simple model for structural properties and crystal stability of sp-bonded solids.* Physical Review B, 1987. **35**(18): p. 9666-9682.

86.   Andersson, M., M. Boman, and S. Östlund, *Density-matrix renormalization group for a gapless system of free fermions.* Physical Review B, 1999. **59**(16): p. 10493-10503.

87.   Frauenheim, T., et al., *Density-functional-based construction of transferable nonorthogonal tight-binding potentials for Si and SiH.* Physical Review B, 1995. **52**(15): p. 11492-11501.

88.   Wang, C.Z. and K.M. Ho, *Environment-Dependent Tight-Binding Potential Models*, in *Handbook of Materials Modeling: Methods*, S. Yip, Editor. 2005, Springer Netherlands: Dordrecht. p. 307-347.

89.   Cohen, R.E., M.J. Mehl, and D.A. Papaconstantopoulos, *Tight-binding total-energy method for transition and noble metals.* Physical Review B, 1994. **50**(19): p. 14694-14697.

90.   Keivan, E. and K. Yoshiyuki, *Self-consistent tight-binding formalism for charged systems.* Journal of Physics: Condensed Matter, 1998. **10**(37): p. 8257.

91.   Bernstein, N. and E. Kaxiras, *Nonorthogonal tight-binding Hamiltonians for defects and interfaces in silicon.* Physical Review B, 1997. **56**(16): p. 10488-10496.

92.   Frauenheim, T., et al., *A Self-Consistent Charge Density-Functional Based Tight-Binding Method for Predictive Materials Simulations in Physics, Chemistry and Biology.* physica status solidi (b), 2000. **217**(1): p. 41-62.

93.   Jayanthi, C.S., et al., *Order-N method for a nonorthogonal tight-binding Hamiltonian.* Physical Review B, 1998. **57**(7): p. 3799-3802.

94.   Wu, S.Y. and C.S. Jayanthi, *Order-N methodologies and their applications.* Physics Reports, 2002. **358**(1): p. 1-74.

95.   Na, J., et al., *Few-Layer Black Phosphorus Field-Effect Transistors with Reduced Current Fluctuation.* Acs Nano, 2014. **8**(11): p. 11753-11762.

96.   Yu, M., et al., *Energetics, relative stabilities, and size-dependent properties of nanosized carbon clusters of different families: Fullerenes, bucky-diamond, icosahedral, and bulk-truncated structures.* The Journal of Chemical Physics, 2009. **130**(18): p. 184708.

97.   Xin, Z.H., et al., *Shedding light on the self-assembly of stable SiC based cage nanostructures: A comprehensive molecular dynamics study.* Computational Materials Science, 2014. **84**: p. 49-62.

98.   Tandy, P., et al., *Next generation of the self-consistent and environment-dependent Hamiltonian: Applications to various boron allotropes from zero- to three-dimensional structures.* The Journal of Chemical Physics, 2015. **142**(12): p. 124106.

99.   Perdew, J.P., et al., *Atoms, molecules, solids, and surfaces: Applications of the generalized gradient approximation for exchange and correlation.* Physical Review B, 1992. **46**(11): p. 6671-6687.

100.   Kresse, G. and J. Furthmuller, *Efficient iterative schemes for ab initio total-energy calculations using a plane-wave basis set.* Physical Review B, 1996. **54**(16): p. 11169-11186.

101.   Vanderbilt, D., *Soft self-consistent pseudopotentials in a generalized eigenvalue formalism.* Physical Review B, 1990. **41**(11): p. 7892-7895.

102.   Blochl, P.E., *Projector Augmented-Wave Method.* Physical Review B, 1994. **50**(24): p. 17953-17979.

103.   Perdew, J.P., K. Burke, and M. Ernzerhof, *Generalized Gradient Approximation Made Simple.* Physical Review Letters, 1996. **77**(18): p. 3865-3868.

104.   Grimme, S., *Semiempirical GGA-type density functional constructed with a long-range dispersion correction.* Journal of Computational Chemistry, 2006. **27**(15): p. 1787-1799.

105.   Grimme, S., et al., *A consistent and accurate ab initio parametrization of density functional dispersion correction (DFT-D) for the 94 elements H-Pu.* The Journal of Chemical Physics, 2010. **132**(15): p. 154104.

106.   Perdew, J.P. and M. Levy, *Physical Content of the Exact Kohn-Sham Orbital Energies: Band Gaps and Derivative Discontinuities.* Physical Review Letters, 1983. **51**(20): p. 1884-1887.

107.   Mori-Sánchez, P., A.J. Cohen, and W. Yang, *Localization and Delocalization Errors in Density Functional Theory and Implications for Band-Gap Prediction.* Physical Review Letters, 2008. **100**(14): p. 146401.

108.   Shishkin, M. and G. Kresse, *Implementation and performance of the frequency-dependent GW method within the PAW framework.* Physical Review B, 2006. **74**(3): p. 035101.

109.   Shishkin, M. and G. Kresse, *Self-consistent GW calculations for semiconductors and insulators.* Physical Review B, 2007. **75**(23): p. 235102.

110.   Heyd, J., G.E. Scuseria, and M. Ernzerhof, *Hybrid functionals based on a screened Coulomb potential.* The Journal of Chemical Physics, 2003. **118**(18): p. 8207-8215.

111.   Pela, R.R., M. Marques, and L.K. Teles, *Comparing LDA-1/2, HSE03, HSE06 and G 0 W 0 approaches for band gap calculations of alloys.* Journal of Physics: Condensed Matter, 2015. **27**(50): p. 505502.

112.   Güttinger, P., *Das Verhalten von Atomen im magnetischen Drehfeld.* Zeitschrift für Physik, 1932. **73**(3): p. 169-184.

113.   Pauli, W., *Principles of Wave Mechanics in Handbuch der Physik.* 1933. **Vol. 24**.

114.   Feynman, R.P., *Forces in Molecules.* Physical Review, 1939. **56**(4): p. 340-343.

115.   Gonze, X., *First-principles responses of solids to atomic displacements and homogeneous electric fields: Implementation of a conjugate-gradient algorithm.* Physical Review B, 1997. **55**(16): p. 10337-10354.

116.   Private contribution from Mr. Md Rajib Khan Musa.

117.   Togo, A., F. Oba, and I. Tanaka, *First-principles calculations of the ferroelastic transition between rutile-type and ${\text{CaCl}}_{2}$-type ${\text{SiO}}_{2}$ at high pressures.* Physical Review B, 2008. **78**(13): p. 134106.

118.   Mulliken, R.S., *Electronic Population Analysis on LCAO–MO Molecular Wave Functions. I.* The Journal of Chemical Physics, 1955. **23**(10): p. 1833-1840.

119.   Cohen, A.D. and C. Reid, *Long Wave Ultraviolet Spectrum of Formaldehyde.* The Journal of Chemical Physics, 1956. **24**(1): p. 85-88.

120.   Ribeiro, H.B., M.A. Pimenta, and C.J.S. de Matos, *Raman spectroscopy in black phosphorus.* Journal of Raman Spectroscopy, 2018. **49**(1): p. 76-90.

121.   Jackson, K., et al., *Raman-active modes of $a\ensuremath{-}{\mathrm{GeSe}}_{2}$ and $a\ensuremath{-}{\mathrm{GeS}}_{2}:$ A first-principles study.* Physical Review B, 1999. **60**(22): p. R14985-R14989.

122.   Lu, Q. and R.U.I. Huang, *NONLINEAR MECHANICS OF SINGLE-ATOMIC-LAYER GRAPHENE SHEETS.* International Journal of Applied Mechanics, 2009. **01**(03): p. 443-467.

123.   Lee, C., et al., *Measurement of the Elastic Properties and Intrinsic Strength of Monolayer Graphene.* Science, 2008. **321**(5887): p. 385-388.

124.   Kudin, K.N., G.E. Scuseria, and B.I. Yakobson, *${\mathrm{C}}_{2}\mathrm{F},$ BN, and C nanoshell elasticity from ab initio computations.* Physical Review B, 2001. **64**(23): p. 235406.

125. Zhou, J. and R. Huang, *Internal lattice relaxation of single-layer graphene under in-plane deformation.* Journal of the Mechanics and Physics of Solids, 2008. **56**(4): p. 1609-1623.

126. Liu, F., P. Ming, and J. Li, *Ab initio calculation of ideal strength and phonon instability of graphene under tension.* Physical Review B, 2007. **76**(6): p. 064120.

127. Cadelano, E., et al., *Nonlinear Elasticity of Monolayer Graphene.* Physical Review Letters, 2009. **102**(23): p. 235502.

128. Dennis, J.E.S., Robert B, *Numerical methods for unconstrained optimization and nonlinear equations.* 1996.

129. Monkhorst, H.J. and J.D. Pack, *Special points for Brillouin-zone integrations.* Physical Review B, 1976. **13**(12): p. 5188-5192.

130. Aresti, A., L. Garbato, and A. Rucci, *Some Cohesive Energy Features of Tetrahedral Semiconductors.* Journal of Physics and Chemistry of Solids, 1984. **45**(3): p. 361-365.

131. Wood, J.D., et al., *Effects of Polycrystalline Cu Substrate on Graphene Growth by Chemical Vapor Deposition.* Nano Letters, 2011. **11**(11): p. 4547-4554.

132. Yao, Y. and C.-p. Wong, *Monolayer graphene growth using additional etching process in atmospheric pressure chemical vapor deposition.* Carbon, 2012. **50**(14): p. 5203-5209.

133. Jayasingha, R., et al., *In Situ Study of Hydrogenation of Graphene and New Phases of Localization between Metal–Insulator Transitions.* Nano Letters, 2013. **13**(11): p. 5098-5105.

134. Zhu, Z. and D. Tománek, *Semiconducting Layered Blue Phosphorus: A Computational Study.* Physical Review Letters, 2014. **112**(17): p. 176802.

135. Fei, R. and L. Yang, *Lattice vibrational modes and Raman scattering spectra of strained phosphorene.* Applied Physics Letters, 2014. **105**(8): p. 083120.

136. Persson, K., et al., *Thermodynamic and kinetic properties of the Li-graphite system from first-principles calculations.* Physical Review B, 2010. **82**(12): p. 125416.

137. Fukuda, K.K., K.; lsono, K.; Yoshio, M., *Foliated natural graphite as the anode material for rechargeable lithium-ion cells.* J. Power Sources, 1997. **69**: p. 165-168.

138. Hightower, A., et al., *Electron energy-loss spectrometry on lithiated graphite.* Applied Physics Letters, 2000. **77**(2): p. 238.

139. Endo, M., et al., *Recent development of carbon materials for Li ion batteries.* Carbon, 2000. **38**: p. 183-197.

140. DiVincenzo, D.P. and E.J. Mele, *Cohesion and structure in stage-1 graphite intercalation compounds.* Physical Review B, 1985. **32**(4): p. 2538-2553.

141. Dahn, J.R., *Phase diagram of ${\mathrm{Li}}_{\mathit{x}}$${\mathrm{C}}_{6}$.* Physical Review B, 1991. **44**(17): p. 9170-9177.

142. *<N doping of graphene through electrothermal reactions with ammonia.pdf>.*

143. Wu, H. and Y. Cui, *Designing nanostructured Si anodes for high energy lithium ion batteries.* Nano Today, 2012. **7**(5): p. 414-429.

144. Chandrasekaran, R., et al., *Analysis of Lithium Insertion/Deinsertion in a Silicon Electrode Particle at Room Temperature.* Journal of The Electrochemical Society, 2010. **157**(10): p. A1139.

145. Teki, R., et al., *Nanostructured silicon anodes for lithium ion rechargeable batteries.* Small, 2009. **5**(20): p. 2236-42.

146. Kasavajjula, U., C. Wang, and A.J. Appleby, *Nano- and bulk-silicon-based insertion anodes for lithium-ion secondary cells.* Journal of Power Sources, 2007. **163**(2): p. 1003-1039.

147. Ohara, S., et al., *A thin film silicon anode for Li-ion batteries having a very large specific capacity and long cycle life.* Journal of Power Sources, 2004. **136**(2): p. 303-306.

148. Szczech, J.R. and S. Jin, *Nanostructured silicon for high capacity lithium battery anodes.* Energy Environ. Sci., 2011. **4**(1): p. 56-72.

149. Key, B., et al., *Real-Time NMR Investigations of Structural Changes in Silicon Electrodes for Lithium-Ion Batteries.* J. AM. CHEM. SOC. , 2009. **131**(26): p. 9239-9249.

150. Liu, N., et al., *A pomegranate-inspired nanoscale design for large-volume-change lithium battery anodes.* Nat Nanotechnol, 2014. **9**(3): p. 187-92.

151. Wu, H., et al., *Stable cycling of double-walled silicon nanotube battery anodes through solid-electrolyte interphase control.* Nat Nanotechnol, 2012. **7**(5): p. 310-5.

152. Chan, C.K., et al., *High-performance lithium battery anodes using silicon nanowires.* Nat Nanotechnol, 2008. **3**(1): p. 31-5.

153. Nagao, M., A. Hayashi, and M. Tatsumisago, *All-solid-state lithium secondary batteries with high capacity using black phosphorus negative electrode.* Journal of Power Sources, 2011. **196**(16): p. 6902-6905.

154.   Stan, M.C., et al., *Puzzling out the origin of the electrochemical activity of black P as a negative electrode material for lithium-ion batteries.* Journal of Materials Chemistry A, 2013. **1**(17): p. 5293-5300.

155.   Sun, L.-Q., et al., *Electrochemical Activity of Black Phosphorus as an Anode Material for Lithium-Ion Batteries.* The Journal of Physical Chemistry C, 2012. **116**(28): p. 14772-14779.

156.   Sun, J., et al., *Formation of stable phosphorus-carbon bond for enhanced performance in black phosphorus nanoparticle-graphite composite battery anodes.* Nano Lett, 2014. **14**(8): p. 4573-80.

157.   Park, C.M. and H.J. Sohn, *Black Phosphorus and its Composite for Lithium Rechargeable Batteries.* Advanced Materials, 2007. **19**(18): p. 2465-2468.

158.   Hembram, K.P.S.S., et al., *Unraveling the Atomistic Sodiation Mechanism of Black Phosphorus for Sodium Ion Batteries by First-Principles Calculations.* The Journal of Physical Chemistry C, 2015. **119**(27): p. 15041-15046.

159.   Fan, X., W.T. Zheng, and J.L. Kuo, *Adsorption and diffusion of Li on pristine and defective graphene.* ACS Appl Mater Interfaces, 2012. **4**(5): p. 2432-8.

160.   Fan, X., et al., *Adsorption of single Li and the formation of small Li clusters on graphene for the anode of lithium-ion batteries.* ACS Appl Mater Interfaces, 2013. **5**(16): p. 7793-7.

161.   Pollak, E., et al., *The interaction of Li+ with single-layer and few-layer graphene.* Nano Lett, 2010. **10**(9): p. 3386-8.

162.   Kucinskis, G., G. Bajars, and J. Kleperis, *Graphene in lithium ion battery cathode materials: A review.* Journal of Power Sources, 2013. **240**: p. 66-79.

163. Zhou, W., et al., *First-principles study of high-capacity hydrogen storage on graphene with Li atoms.* Journal of Physics and Chemistry of Solids, 2012. **73**(2): p. 245-251.

164. Hardikar, R.P., et al., *Boron doped defective graphene as a potential anode material for Li-ion batteries.* Phys Chem Chem Phys, 2014. **16**(31): p. 16502-8.

165. Su, F.-Y., et al., *Could graphene construct an effective conducting network in a high-power lithium ion battery?* Nano Energy, 2012. **1**(3): p. 429-439.

166. Lee, E. and K.A. Persson, *Li absorption and intercalation in single layer graphene and few layer graphene by first principles.* Nano Lett, 2012. **12**(9): p. 4624-8.

167. Khantha, M., et al., *Interaction of lithium with graphene: Anab initiostudy.* Physical Review B, 2004. **70**(12).

168. Pan, D., et al., *Li Storage Properties of Disordered Graphene Nanosheets.* Chemistry of Materials, 2009. **21**(14): p. 3136-3142.

169. Hu, Y.-Y., et al., *How the Number and Location of Lithium Atoms Affect the First Hyperpolarizability of Graphene.* J. Phys. Chem. C 2010. **114**(46): p. 19792–19798.

170. Guo, P., H. Song, and X. Chen, *Electrochemical performance of graphene nanosheets as anode material for lithium-ion batteries.* Electrochemistry Communications, 2009. **11**(6): p. 1320-1324.

171. Yoo, E., et al., *Large Reversible Li Storage of Graphene Nanosheet Families for Use in Rechargeable Lithium Ion Batteries.* Nano Lett, 2008. **8**(8): p. 2277-2282.

172. Dahn, J.R., et al., *Mechanisms for Lithium Insertion in Carbonaceous Materials.* since, 1995. **270**: p. 590-593.

173. Liu, Y., et al., *mechanism of Lithium insertion in hard carbons prepared by pyrolysis of epoxy resins.* Carbon, 1996. **34**(2): p. 193-200.

174. Wang, G., et al., *Graphene nanosheets for enhanced lithium storage in lithium ion batteries.* Carbon, 2009. **47**(8): p. 2049-2053.

175. Lian, P., et al., *Large reversible capacity of high quality graphene sheets as an anode material for lithium-ion batteries.* Electrochimica Acta, 2010. **55**(12): p. 3909-3914.

176. Uthaisar, C., V. Barone, and J.E. Peralta, *Lithium adsorption on zigzag graphene nanoribbons.* Journal of Applied Physics, 2009. **106**(11): p. 113715.

177. Uthaisar, C. and V. Barone, *Edge effects on the characteristics of li diffusion in graphene.* Nano Lett, 2010. **10**(8): p. 2838-42.

178. Wang, Q. and J. Li, *Facilitated Lithium Storage in MoS2 Overlayers Supported on Coaxial Carbon Nanotubes.* J. Phys. Chem. C 2007. **111**(4): p. 1675-1682.

179. Feng, C., et al., *Synthesis of molybdenum disulfide (MoS2) for lithium ion battery applications.* Materials Research Bulletin, 2009. **44**(9): p. 1811-1815.

180. Du, G., et al., *Superior stability and high capacity of restacked molybdenum disulfide as anode material for lithium ion batteries.* Chem Commun (Camb), 2010. **46**(7): p. 1106-8.

181. Hwang, H., H. Kim, and J. Cho, *MoS(2) nanoplates consisting of disordered graphene-like layers for high rate lithium battery anode materials.* Nano Lett, 2011. **11**(11): p. 4826-30.

182.	Chang, K. and W. Chen, *In situ synthesis of MoS2/graphene nanosheet composites with extraordinarily high electrochemical performance for lithium ion batteries.* Chem Commun (Camb), 2011. **47**(14): p. 4252-4.

183.	Chang, K. and W. Chen, *Single-layer MoS2/graphene dispersed in amorphous carbon: towards high electrochemical performances in rechargeable lithium ion batteries.* Journal of Materials Chemistry, 2011. **21**(43): p. 17175.

184.	Chang, K., et al., *Graphene-like MoS2/amorphous carbon composites with high capacity and excellent stability as anode materials for lithium ion batteries.* Journal of Materials Chemistry, 2011. **21**(17): p. 6251.

185.	Zhang, Y.F., et al., *Different growth behaviors of ambient pressure chemical vapor deposition graphene on Ni(111) and Ni films: A scanning tunneling microscopy study.* Nano Research, 2012. **5**(6): p. 402-411.

186.	Jing, Y., et al., *Metallic VS2Monolayer: A Promising 2D Anode Material for Lithium Ion Batteries.* The Journal of Physical Chemistry C, 2013. **117**(48): p. 25409-25413.

187.	Xiao, J., et al., *Exfoliated MoS2Nanocomposite as an Anode Material for Lithium Ion Batteries.* Chemistry of Materials, 2010. **22**(16): p. 4522-4524.

188.	Zhou, M., Y. Zhai, and S. Dong, *Electrochemical Sensing and Biosensing Platform Based on Chemically Reduced Graphene Oxide.* Anal. Chem. , 2009. **81**(14): p. 5603-5613.

189.	Er, D., et al., *Ti3C2 MXene as a High Capacity Electrode Material for Metal (Li, Na, K, Ca) Ion Batteries.* ACS Applied Materials & Interfaces, 2014. **6**(14): p. 11173-11179.

190. Buscema, M., et al., *Fast and broadband photoresponse of few-layer black phosphorus field-effect transistors.* Nano Lett, 2014. **14**(6): p. 3347-52.

191. Rodin, A.S., A. Carvalho, and A.H. Castro Neto, *Strain-induced gap modification in black phosphorus.* Phys Rev Lett, 2014. **112**(17): p. 176801.

192. Xu, Y., J. Dai, and X.C. Zeng, *Electron-Transport Properties of Few-Layer Black Phosphorus.* J Phys Chem Lett, 2015. **6**(11): p. 1996-2002.

193. Fei, R. and L. Yang, *Strain-engineering the anisotropic electrical conductance of few-layer black phosphorus.* Nano Lett, 2014. **14**(5): p. 2884-9.

194. Jiang, J.W. and H.S. Park, *Negative poisson's ratio in single-layer black phosphorus.* Nat Commun, 2014. **5**: p. 4727.

195. Jiang, J.-W. and H.S. Park, *Mechanical properties of single-layer black phosphorus.* Journal of Physics D: Applied Physics, 2014. **47**(38): p. 385304.

196. Buscema, M., et al., *Photovoltaic effect in few-layer black phosphorus PN junctions defined by local electrostatic gating.* Nat Commun, 2014. **5**: p. 4651.

197. Yuan, J., et al., *Photoluminescence Quenching and Charge Transfer in Artificial Heterostacks of Monolayer Transition Metal Dichalcogenides and Few-Layer Black Phosphorus.* ACS Nano, 2015. **9**(9).

198. Li, W., et al., *Ultrafast and directional diffusion of lithium in phosphorene for high-performance lithium-ion battery.* Nano Lett, 2015. **15**(3): p. 1691-7.

199. Yao, Q., et al., *Theoretical Prediction of Phosphorene and Nanoribbons As Fast-Charging Li Ion Battery Anode Materials.* The Journal of Physical Chemistry C, 2015. **119**(12): p. 6923-6928.

200. Guo, G.C., et al., *First-Principles Study of Phosphorene and Graphene Heterostructure as Anode Materials for Rechargeable Li Batteries.* J Phys Chem Lett, 2015. **6**(24): p. 5002-8.

201. Kulish, V.V., et al., *Adsorption of metal adatoms on single-layer phosphorene.* Phys Chem Chem Phys, 2015. **17**(2): p. 992-1000.

202. Li, Q.-F., et al., *Theoretical Prediction of Anode Materials in Li-Ion Batteries on Layered Black and Blue Phosphorus.* The Journal of Physical Chemistry C, 2015. **119**(16): p. 8662-8670.

203. Zhao, S., W. Kang, and J. Xue, *The potential application of phosphorene as an anode material in Li-ion batteries.* J. Mater. Chem. A, 2014. **2**(44): p. 19046-19052.

204. Liu, X., et al., *A first-principles study of sodium adsorption and diffusion on phosphorene.* Phys Chem Chem Phys, 2015. **17**(25): p. 16398-404.

205. Kulish, V.V., et al., *Phosphorene as an anode material for Na-ion batteries: a first-principles study.* Phys Chem Chem Phys, 2015. **17**(21): p. 13921-8.

206. Hashmi, A., U. Farooq, and J. Hong, *Graphene/phosphorene bilayer: High electron speed, optical property and semiconductor-metal transition with electric field.* Current Applied Physics, 2016. **16**(3): p. 318-323.

207. Henkelman, G., B.P. Uberuaga, and H. Jónsson, *A climbing image nudged elastic band method for finding saddle points and minimum energy paths.* The Journal of Chemical Physics, 2000. **113**(22): p. 9901-9904.

208. Henkelman, G. and H. Jónsson, *Improved tangent estimate in the nudged elastic band method for finding minimum energy paths and saddle points.* The Journal of Chemical Physics, 2000. **113**(22): p. 9978-9985.

209. Grimme, S., *Semiempirical GGA-type density functional constructed with a long-range dispersion correction.* J Comput Chem, 2006. **27**(15): p. 1787-99.

210. Liu, H., et al., *Phosphorene: An Unexplored 2D Semiconductor with a High Hole Mobility.* Acs Nano, 2014. **8**(4): p. 4033-4041.

211. Tandy, P. Thesis: *a semi-emperical Hamiltonian for boron, phosphorus and compounds containing boron, phosphorus and silicon.* 2007.

212. Patel, S., et al., *NanoScript: A Nanoparticle-Based Artificial Transcription Factor for Effective Gene Regulation.* Acs Nano, 2014. **8**(9): p. 8959-8967.

213. Chen, M.D., et al., *A theoretical study for the isomers of neutral, cationic and anionic phosphorus clusters P5, P7, P9.* Chemical Physics Letters, 2000. **325**(1): p. 22-28.

214. Private contribution from Dr. Qi, D.

215. Song, W., et al., *Two selective growth modes for graphene on a Cu substrate using thermal chemical vapor deposition.* Carbon, 2014. **68**: p. 87-94.

216. Zhang, C., et al., *The prospects of phosphorene as an anode material for high-performance lithium-ion batteries: A fundamental study.* Vol. 28. 2017. 075401.

217. Akhtar, M., *Synthesis and fundamental property studies of energy material under high pressure.* PhD. thesis, 2017.

CURRICULUM VITAE

Name: Zhang, Congyan

Email: c0zhan09@louisville.edu

Phone number: +1 502-762-5419

Mailing Address: 1860 Blvd De Province Apt 174, Baton Rouge, LA, 70816

Education

Ph. D.: Department of Physics & Astronomy   **Supervisor**: Ming Yu

❖ **August 2015-Present**: University of Louisville – Kentucky, U.S.A

Master: Department of Physics & Astronomy   **Supervisor**: Ming Yu

❖ **August 2013-July 2015**: University of Louisville – Kentucky, U.S.A

Master: Department of Physics, School of Science   **Supervisor**: Zihua Xin

❖ **September 2010- July 2013**: Shanghai University – Shanghai, China

Bachelor: Department of Physics, School of Science

❖ **September 2006-July 2010:** North University of China – Shanxi, China

Work Experience

Research Assistant, University of Louisville, Louisville, KY (08/2014 - Present)

❖ Developed semi-empirical self-consistent and environment-dependent (SCED) Hamiltonian in the framework of the linear combination of atomic orbitals (LCAO) methods; Optimized the SCED Hamiltonian for Phosphorus and Lithium atoms by fitting

their properties with the ab-initial DFT and GAUSSIAN calculations.

❖ Predicted and simulated the performance of phosphorene as an anode material for Lithium ion battery by employing DFT based simulations. Associated with the experimental observation, proved that phosphorene is a promising candidate for the anode material with high diffusion speed, high capacity.

❖ Combine with the experimental observation, simulated the vibrational properties of phosphorene under high pressure by using DFT based simulations. Explained the reason of Raman shift by analyzing the structural properties of phosphorene under high pressure.

❖ Predicted and simulated new allotropes 2D GaP and InP monolayer structures with high puckered orthorhombic symmetry DFT based simulations. Obtained the sandwiched 2D phosphide binary compounds sheets with isotropic structural, electronic, and mechanical properties.

❖ Studied GaP/InP and SiC/GeC in-plane hetero-structures, predicted the structural and electronical properties the hetero-structures with different combination.

❖ Predicted the phase transition from black phosphorus to blue phosphorus by inserting Li ions under ambient condition, and subsequently, providing a new guideline for producing blue phosphorene using mechanical exfoliation.

Teaching Assistant, University of Louisville, Louisville, KY (08/2013 - Present)

❖ Taught and graded the physics labs for undergrad students (three sections per semester). Labs covered mechanics, optics, thermodynamic and electrodynamic

❖ Help students with what they have learned in the lecture, improve their ability to solve physics problems

Teaching Assistant, Shanghai University, Shanghai, China (04/2011 – 06/2013)

❖ Mentored senior students for their graduate research projects (designed the experiments, analyzed the experimental data and revised their final project reports, etc.)

Computational Skill

❖ Experience in reading and writing Fortran program

❖ Experience in using VASP code, Gaussian03 code and SCED-LCAO

❖ Experience in using software including Material Studio (MS), MOLDEN, Xmgrace, VASPview, PHONOPY, bader, Origin-lab and so on

❖ Comfortable with operating systems: Mac OS, WINDOWS, UNIX, and Linux operating environments & packages

Publications & Presentations

❖ Paper

1. Theoretical prediction of sandwiched two-dimensional phosphide binary compounds sheets with tunable bandgaps and anisotropic physical properties, *C. Y. Zhang*, M. Yu, **Nanotechnology** 29 (2018) 095703.

2. Prospects of Phosphorene as an Anode Material for High Performance Lithium-Ion Battery: a Fundamental Study, *C. Y. Zhang*, M. Yu, G. Anderson, R. R. Dharmasena, and G. Sumanasekera, **Nanotechnology** 28 (2017) 075401.

3. Shedding light on the self-assembly of stable SiC based cage nanostructures: A comprehensive molecular dynamics study, Z. H. Xin, *C. Y. Zhang*, M. Yu, C. S. Jayanthi, S. Y. Wu, **Computational Materials Science** 84 (2014) 49-62.

4. Opt-electronic and adsorption properties of phosphorene, G. Anderson, **_C. Y. Zhang_**, M. Rajapaksa, R. Musa, M. Yu, J. Jasinski, G. Sumanasekera (in preparation)

5. Vibrational properties of phosphorene under high pressure, M. Akhter, **_C. Y. Zhang_**, M. Rajapaksa, R. Musa, M. Yu, J. Jasinski, G. Sumanasekera (in preparation)

❖ Meeting

1. 2018, oral representation "New two-dimensional anisotropic monolayers of phosphide binary compounds with wide fundamental bandgaps" APS March Meeting, Los Angeles, CA.

2. 2017, oral representation " Prospects of Phosphorene as an Anode Material for High Performance Lithium-Ion Battery" departmental Colloquium, University of Louisville.

3. 2017, oral representation "Computational design of a novel two dimensional InP nanostructure", APS March Meeting, New Orleans, LA.

4. 2016, oral representation "First-principle study of the energy barrier and diffusivity of Li atom on phosphorene", APS March Meeting, Baltimore, MD.

5. 2015, poster "Preferential adsorption positions for an adsorbed Li atom on the layered black phosphorus", APS March Meeting, San Antonio, TX.

6. 2014, poster "A comprehensive molecular dynamics study on the self-assembly and properties of SiC based cage structures", APS March Meeting, Denver, CO.

Awards

❖ GSC Travel Funding, School of Interdisciplinary and Graduate Studies, University of Louisville (**2016-2017**)

❖ GSC Travel Funding, School of Interdisciplinary and Graduate Studies, University of Louisville (**2017-2018**)

❖ Arts and Sciences Research & Creative Activities Award, College of Arts and Sciences, University of Louisville (**2017-2018**)